© Copyright 2020

Jiajiu Zheng

Nonvolatile Integrated Phase-Change Photonic Platform for Programmable Photonics

Jiajiu Zheng

A dissertation

submitted in partial fulfillment of the

requirements for the degree of

Doctor of Philosophy

University of Washington

2020

Reading Committee:

Arka Majumdar, Chair

Scott Dunham

Lih-Yuan Lin

Program Authorized to Offer Degree:

Electrical Engineering

University of Washington

Abstract

Nonvolatile Integrated Phase-Change Photonic Platform for Programmable Photonics

Jiajiu Zheng

Chair of the Supervisory Committee:
Arka Majumdar
Department of Electrical and Computer Engineering

With the slowing down of Moore's law and advances in nanophotonics, photonic information processing by photonic integrated circuits (PICs) has raised considerable interest to compete with electronic systems in energy-efficient high-throughput data processing, especially for emerging applications such as neuromorphic computing, quantum information, and microwave photonics. Success in these fields usually requires large-scale programmable PICs providing low-energy, compact, and high-speed building blocks with ultra-low insertion loss and precise control. Current programmable photonic systems, however, primarily rely on materials with weak and volatile thermo-optic or electro-optic modulation effects, leading to large footprints and high energy consumption. Alternatively, chalcogenide phase-change materials (PCMs) such as $Ge_2Sb_2Te_5$ (GST) exhibit a substantial optical contrast in a static, self-holding fashion upon phase transitions, but the complexity of present PCM-integrated photonic applications is still limited mainly due to the poor optical or electrical actuation approaches. In this dissertation, by integrating GST on silicon photonic devices, a highly scalable nonvolatile integrated phase-change photonic platform with strong broadband attenuation modulation and optical phase modulation for programmable photonics is demonstrated. Utilizing a free-space pulsed laser, reversible all-optically quasi-continuous programming of the platform is performed, resulting in a nonvolatile multi-level microring-based photonic switch with a high extinction ratio up to 33 dB. To extend the platform to a multi-port broadband scheme, compact (~30 μm), low-loss (~1 dB), and broadband (over 30 nm with cross talk less than −10 dB) 1 × 2 and 2 × 2 switches are demonstrated based on the asymmetric directional coupler design. Electrical switching of the platform with different heaters including graphene, indium tin oxide, and silicon PIN diode heaters that allows large-scale integration and fast energy-efficient large-area switching is then modeled and compared, followed by the experiment with PIN diode heaters. Using GST-clad silicon waveguides and microring resonators, intrinsically compact and energy-efficient photonic switching units operated with low driving voltages, near-zero additional loss, and reversible switching with long endurance are obtained in a complementary metal-oxide-semiconductor (CMOS)-compatible process. This work paves the way for the very large-scale CMOS-integrated programmable electronic-photonic systems such as optical neural networks and general-purpose integrated photonic processors.

TABLE OF CONTENTS

List of Figures iv

List of Tables xiv

Chapter 1. Introduction 1

- 1.1 Photonic Information Processing: Opportunities and Challenges 2
- 1.2 The Rise of Phase-Change Materials 4
- 1.3 Contents and Highlights 5

Chapter 2. Nonvolatile Integrated Phase-Change Photonic Platform 9

- 2.1 Characterization of GST 9
- 2.2 Design and Fabrication 10
- 2.3 Characterization of the Platform 12
- 2.4 Summary 18

Chapter 3. All-Optical Multi-Level Operation 19

- 3.1 All-Optical Switching 19
- 3.2 Multi-Level Operation and Mircoring-Based Switch 22
- 3.3 Summary 23

Chapter 4. Low-Loss and Broadband Multi-Port Photonic Switches 25

- 4.1 1 × 2 Photonic Switch 25
  - 4.1.1 Design and Simulation 25
  - 4.1.2 Experiment 29

4.2 2 × 2 Photonic Switch 30

4.2.1 Design and Simulation 30

4.2.2 Experiment 34

4.3 Discussion 35

4.3.1 Optical Bandwidth of the Switches 35

4.3.2 Design of the Switches for TM Polarization 36

4.4 Summary 37

Chapter 5. Modeling Electrical Switching with Heaters 39

5.1 Device Configuration and Modeling 41

5.1.1 Device Configuration 41

5.1.2 Model Description 42

5.1.3 Material Parameters 44

5.2 Optical Performance 45

5.3 Heating Performance 48

5.3.1 Temperature Distribution 48

5.3.2 Transient Response and Switching Speed 52

5.3.3 Energy Efficiency 54

5.4 Comparison with ITO and PIN Diode Heaters 56

5.4.1 Device Configuration and Modeling 57

5.4.2 Performance Comparison 58

5.5 Summary 61

Chapter 6. Experimental Demonstration of Electrical Switching with PIN Diode Heaters 63

6.1 Experimental Method 63

6.1.1 Device Structure and Fabrication 63

6.1.2 Static Measurement 65

6.1.3 Transient Response Measurement 67

6.1.4 Device Modeling and Simulation 68

6.2 Operating Principle and Performance 69

6.3 Application in Microring Resonators 75

6.4 Discussion 77

6.4.1 Insertion Loss 77

6.4.2 Heating Dynamics 80

6.5 Summary 83

Chapter 7. Conclusions and Outlook 85

Bibliography 88

LIST OF FIGURES

Figure 2.1. GST characterization. (a) Complex refractive index of aGST and cGST as a function of wavelength. (b) XRD data of aGST and cGST. The curve of cGST is offset vertically for clarity. 10

Figure 2.2. GST-on-silicon hybrid integrated nanophotonic platform. (a) Schematic of the platform. Inset: cross-section of the hybrid waveguide. To emphasize the gap between the waveguide and the ring, the schematic is not in scale. (b,c) Fundamental quasi-transverse electric (TE) mode profiles (normalized amplitude profiles of the electric field) of the hybrid waveguide at 1550 nm for (b) aGST with $\tilde{n}_{\mathrm{eff}} = 2.62 - 0.0024\ i$ and (c) cGST with $\tilde{n}_{\mathrm{eff}} = 2.97 - 0.22\ i$. Both were simulated with frequency-domain FEM using the optical constants of GST and ITO measured by ellipsometry. (d) SEM image of a microring with 5 μm as-deposited GST. (e) AFM height map of the region highlighted by the yellow dashed rectangle in (d). 11

Figure 2.3. Transmission measurement of the microrings with GST. (a) Representative output spectra of microrings with different length of GST for amorphous and crystalline states. For each length of GST, the cGST and aGST spectra are in scale, while each set of spectra for a different length of GST is offset vertically for clarity. (b,c) Microscope images of a microring with 5 μm (b) aGST and (c) cGST. 14

Figure 2.4. Characterization of the GST-on-silicon platform using microring resonators. (a) Lorentzian fitting of the spectrum for the resonance dips in a ring with Q ~11,000 near 1550 nm. (b,c) GST length-dependent (b) loss and (c) spectral shift of the microrings for aGST and cGST with respect to those of the intrinsic microrings. Every dot represents a single device. (d,e) Wavelength-dependent (d) attenuation coefficient and (e) resonance shift per unit GST length for aGST and cGST with respect to the reference (before GST deposition). Dots: experiment data. Dotted lines: linear fitting. Solid lines: simulation. 16

Figure 3.1. Determination of GST phase transition conditions by an optical heating setup. (a) Schematic of the optical imaging system. PCX Lens, plano-convex lens. (b) Schematic of the optical pumping system. (c) Induced attenuation coefficient as a function of the fluence of a single laser pulse. White, blue, and red dots denote devices that retained the crystalline state, had intermediate states of GST, and had damaged GST, respectively. Inset: the green Gaussian pulse denotes that only a single pulse was used for this experiment. (d) Sample output spectra of a microring with 4 μm GST in the determined Set and Reset conditions. 20

Figure 3.2. Quasi-continuous tuning of the GST-on-silicon hybrid integrated nanophotonic platform. (a) Output spectra of a microring with 2 μm GST under different number of excitations, where "excitation" denotes a packet of 25 consecutive pulses applied at 50 kHz repetition rate. (b) A zoom-in inspection of the region highlighted by the grey dashed rectangle in the spectra in (a). (c) Attenuation coefficient of the hybrid waveguide as a function of the number of excitations. Inset: the green Gaussian pulse with "×25" denote the excitation process. 23

Figure 4.1. Simulation of the 1 × 2 DC switch. (a) Schematic of the switch. (b,c) Normalized optical field intensity distribution of the switch for (b) aGST and (c) cGST simulated at 1550 nm. (d,e) Calculated transmission spectra at the cross and bar ports for (d) aGST and (e) cGST. 26

Figure 4.2. Mode analysis of the two-waveguide system. (a) Left: effective indices of the fundamental modes in the silicon SW and the HW. Right: the normalized electrical field profiles of the TE mode with GST in the amorphous and crystalline state. The widths of the SW and the HW are $w_s = 450$ nm and $w_c = 420$ nm, respectively. (b-e) Normalized electrical field profiles of the supermodes in the two-waveguide system when the GST is in (b,c) amorphous and (d,e) crystalline state. All the modes are simulated for TE polarization at 1550 nm. 27

Figure 4.3. Trade-off between the coupling length for the maximum transmission in the amorphous state and insertion loss in the crystalline state by varying the gap..................28

Figure 4.4. Experimental results of the 1 × 2 DC switch. (a) Optical microscope image of the fabricated switch. (b) SEM image of the switch. (c) An enlarged view of the coupling region highlighted by the orange rectangle in (b) with the GST false-colored. (d-e)

Measured transmission at the cross and bar ports with the GST in the (d) amorphous and (e) crystalline states......29

Figure 4.5. Simulation of the 2 × 2 DC switch. (a) Schematic of the switch. (b,c) Normalized optical field intensity distribution in the device for (b) aGST and (c) cGST simulated at 1550 nm. (d,e) Calculated transmission spectra at the cross and bar ports for (d) aGST and (e) cGST. 31

Figure 4.6. Mode analysis of the three-waveguide system. (a-e) Normalized E_y field profiles of the supermodes in a three-waveguide system when GST is in the (a-c) amorphous and (d-e) crystalline state. (f) Effective indices of five supermodes guided in the three-waveguide coupler as a function of w_c when $g = 150$ nm, $w_s = 450$ nm, $w_p = w_c - 100$ nm. The maximum coupling efficiency can be achieved when $w_c = 422$ nm, *i.e.*, $n_{aGST3} = (n_{aGST1} + n_{aGST2})/2$. All the modes are simulated for TE polarization at 1550 nm......32

Figure 4.7. Trade-off between L_{aGST} and L_{cGST}/L_{aGST} by varying the gap. 33

Figure 4.8. Experimental results of the 2 × 2 DC switch. (a) Optical microscope image of the fabricated switch. (b) SEM image of the switch. (c) An enlarged view of the coupling region highlighted by the orange rectangle in (b) with the GST false-colored. (d,e) Measured transmission at the cross and bar ports with the GST in the (d) amorphous and (e) crystalline states......34

Figure 4.9. Full wavelength range transmission spectra of the 1 × 2 DC switch at the cross and bar ports for (a,b) simulations and (c,d) experiments. 35

Figure 4.10. Full wavelength range transmission spectra of the 2 × 2 DC switch at the cross and bar ports for (a,b) simulations and (c,d) experiments. 36

Figure 4.11. Design of the 1 × 2 DC switch for TM polarization. (a) Left: effective indices of the fundamental TM modes in the silicon SW and the HW. Right: the normalized electrical field profiles of the TM mode with GST in the amorphous and crystalline state. The widths of the SW and the HW are $w_s = 550$ nm and $w_c = 390$ nm, respectively. The width of the GST (w_p) is set to be 100 nm smaller than w_c. (b-e) Normalized electrical field profiles of the supermodes in the two-waveguide system when the GST is in (b,c) amorphous and (d,e) crystalline state. All the modes are simulated for TM polarization at 1550 nm..37

Figure 5.1. Device configuration. (a) Schematic of the proposed PINC with a graphene heater. Here, the silica cladding is hidden for clarity. The two ports of the PINC are connected with regular silicon rib waveguides in this case. Inset: cross-section of the hybrid cell. (b) Operation principle of electrical switching of the PINC with an external heater. The lattice structure, refractive index (n), and extinction coefficient (κ) of GST for amorphous and crystalline states and the electric power of the reset and set pulses are illustrated..42

Figure 5.2. Dependence of optical figure of merits on the (a) width and (b) height of the silicon rib waveguide and the (c) width and (d) thickness of the GST film at 1550 nm. By default, the width and thickness of the GST are 500 nm and 20 nm, respectively, while the width and height of the silicon rib are fixed to be 500 nm and 120 nm, respectively. This default waveguide geometry is marked as the dots in the figures and adopted for the following analysis unless specifically pointed out. Neither heaters nor metal contacts are involved at this stage...45

Figure 5.3. Dependence of optical performance on the waveguide geometry. (a,b) Normalized electrical field profile and complex effective index ($\tilde{n}_{\mathrm{eff}}$) of the fundamental quasi-transversal electric (TE) mode of the GST-on-silicon hybrid waveguide with (a) aGST and (b) cGST at a wavelength (λ) of 1550 nm. The width and thickness of the GST are 500 nm and 20 nm, respectively. (c,d) Effective refractive index (n_{eff}) and attenuation coefficient ($\alpha = 4\pi\kappa_{\mathrm{eff}}/\lambda$, λ = 1550 nm) of the hybrid waveguide as a function of the (c) width and (d) thickness of the GST with h_{GST} = 20 nm in (c) and w_{GST} = 500 nm in (d). The marked dots correspond to the structure in (a) and (b) and denote the adopted waveguide geometry for the following analysis unless specifically pointed out. Here, the width and height of the silicon rib are fixed to be 500 nm and 120 nm, respectively. Neither heaters nor metal contacts are involved at this stage. 46

Figure 5.4. Additional loss introduced from metal contacts as a function of the distance between the edges of the electrodes and the rib waveguide. The marked dot corresponds to the adopted distance in the main text. 48

Figure 5.5. Temperature distribution analysis. (a) Temperature (T) profile of the PINC for aGST at the end of a pulse (P_0 = 5 mW, Δt = 50 ns). No phase transition is induced due to this pulse. The dashed lines denote the coordinate system with the x (y) axis parallel (perpendicular) to the surface of the GST film and the origin located at the center of the GST cross-section. (b) Temperature profile along the x axis in (a). (c) Temperature profile along the y axis in (a). The orange shaded areas in (b) and (c) represent the position of the GST film. (d) Temperature distribution at different times for a crystallization (Set) process (P_0 = 14 mW). The red lines denote the contour of T = 723 K, within which the GST is assumed to be crystallized. (e) Temperature gradient (ΔT, also marked in (c)) at the end of a pulse as a function of pulse power for different pulse widths. Inset: illustration of the applied pulse. (f) Temperature gradient at the end of a pulse as a function of GST thickness for different pulse widths (P_0 = 5 mW). The pulse energy is selected to be sufficiently low to avoid causing any phase transition of aGST in (e) and (f). 50

Figure 5.6. Real-time temperature gradient during the crystallization process (P_0 = 14 mW, Δt = 50 ns). 51

Figure 5.7. Temperature distribution at the end of a pulse indicating re-amorphization during the crystallization process due to much too high power (upper panel, P_0 = 27 mW, Δt = 9 ns, h_{GST} = 10 nm) and large GST thickness (lower panel, P_0 = 15 mW, Δt = 30 ns, h_{GST} = 50 nm). The red (green) lines denote the contour of T = 723 K (T = 883 K) for the crystallization (re-amorphization) boundary. 51

Figure 5.8. Transient response and speed analysis. (a) Normalized temperature response in the center of the GST cross-section to the pulses with different pulse widths. The power of the pulse is chosen to be as low as 5 mW in order to heat the cGST without inducing any phase transition. The dashed line denotes the position where the temperature is 1/e of the maximum. (b) Extracted dead time (τ, 1/e cooling time) from (a) as a function of pulse width. Inset: illustration of the applied pulse and temperature response. (c) Area chart of the minimum pulse width (Δt_{ac}) and corresponding dead time (τ_{ac}) required to achieve complete crystallization actuated by the maximum allowed pulse power (black line) as a function of GST thickness. Inset: transient temperature response of the crystallization process for different thicknesses of GST. 52

Figure 5.9. Power-dependent transient response. (a) Temperature response in the center of the GST cross-section to the pulses with different pulse power. Inset: corresponding normalized temperature response. The dashed line denotes the position where the temperature is 1/e of the maximum. The power of the pulse is chosen to be low enough in order to heat the cGST without inducing any phase transition and the pulse width is 10 ns. (b) Minimum pulse width required to achieve complete crystallization as a function of pulse power. 53

Figure 5.10. GST thickness-dependent transient response. (a) Normalized temperature response in the center of the GST cross-section for different GST thicknesses. The power of the pulse is chosen to be as low as 5 mW in order to heat the cGST without inducing any phase transition and the pulse width is 10 ns. The dashed line denotes the position where the temperature is 1/e of the maximum. (b) Extracted dead time as a function of GST thickness for different pulse widths. The dashed line denotes the adopted thickness in the main text. (c) Area chart of the minimum pulse width and corresponding dead time required to achieve complete crystallization actuated by a fixed pulse power (P_0 = 10.8 mW) as a function of GST thickness. Inset: transient temperature response of the crystallization process for different thicknesses of GST. 54

Figure 5.11. Energy efficiency analysis. (a) Energy efficiency (η) as a function of pulse width. Inset: pulse-power insensitive energy efficiency (Δt = 10 ns). (b) Energy efficiency as a function of GST thickness for different pulse widths. The pulse power is selected as low as 5 mW for (a) and (b) in order to heat the aGST without inducing any phase transition. (c) GST-thickness dependent energy efficiency for crystallization (η_{ac}) actuated by a pulse with optimal power (blue line) and fixed power (red line). 55

Figure 5.12. Power-dependent energy efficiency for different pulse widths. The pulse power is selected to be low enough in order to heat the aGST without inducing any phase transition. 56

Figure 5.13. Cross-section schematics of the PINCs with graphene, ITO, and PIN diode heaters. p++ (n++), heavily doped p (n)-type silicon region. i, intrinsic silicon region. 57

Figure 5.14. Current-voltage (I-V) curve of the silicon PIN diode. 58

Figure 5.15. Comparison of temperature response of the PINCs with different heaters for crystallization. (a) Transient temperature response of the PINCs with different heaters for crystallization. (b) Temperature distribution at the end of a pulse during the crystallization process in (a) for the PINCs with graphene, ITO, and PIN diode heaters. The power and width of the Set pulse for three heaters are listed in the corresponding figures. p++ (n++), heavily doped p (n)-type silicon region. i, intrinsic silicon region. 59

Figure 5.16. Comparison of temperature response of the PINCs with different heaters for amorphization. (a) Transient temperature response of the PINCs with different heaters for amorphization. (b) Temperature distribution at the end of a pulse during the amorphization process in (a) for the PINCs with graphene, ITO, and PIN diode heaters. The power and width of the Set pulse for three heaters are listed in the corresponding figures. p++ (n++), heavily doped p (n)-type silicon region. i, intrinsic silicon region. 59

Figure 6.1. Nonvolatile electrically reconfigurable photonic switching units. (a) Schematic of the device. For clarity, the top thin-film Al_2O_3 encapsulating layer is not displayed. Inset: cross-section of the device. (b) Top-view optical microscope image of the switching unit on a waveguide with 10-nm-thick GST and a 5-μm-long active region. Inset: SEM image of the grating coupler. (c) Optical microscope image of the black dashed area in (b). (d) SEM image of the active region boxed in (c). False color is used to highlight the GST (orange). S (G), signal (ground) electrode. p++ (n++), heavily doped p (n)-type silicon region. i, intrinsic silicon region. 65

Figure 6.2. Experimental setups. (a) Setup for static measurement. (b) Setup for transient response measurement. The tools framed with dashed red lines were used for measuring the pulse width modulation (PWM) effects. TSL, tunable laser. PC, polarization controller. SMU, source meter unit. EDFA, erbium-doped fiber amplifier. DEMUX, optical demultiplexer. VOA, variable optical attenuator. PD, photodiode. 67

Figure 6.3. Operating principle of the photonic switching units. (a,b) Real-time voltage of the applied electrical pulse (upper panel), corresponding change in optical transmission (with the minimum value normalized to –1) of the switching unit at 1550 nm (middle panel), and simulated temperature response in the center of the GST cross-section to the equivalent pulse with the same power and width (lower panel) for crystallization (Set, a) and amorphization (Reset, b). Insets of the upper panels: schematic of the GST structure changes due to the phase transitions. The orange shaded areas in the lower panel represent the assumed temperature intervals where the properties of GST are weighted sums of those in the amorphous and crystalline states during phase transitions. T_g, glass transition temperature of GST. T_m, melting point of GST. (c) Simulated electric field ($|E|$) profiles for the fundamental quasi-TE mode of the switching unit at 1550 nm in the crystalline (top, $\tilde{n}_{eff} = 2.68 - 0.05$ i) and amorphous (bottom, $\tilde{n}_{eff} = 2.60 - 1.06 \times 10^{-3}$ i) states. (d) Simulated temperature (T) distributions of the switching unit cross-section for crystallization (top) and amorphization (bottom) at the time (t) marked by the dots in the lower panels of (a) and (b), respectively. p++ (n++), heavily doped p (n)-type silicon region. i, intrinsic silicon region. Here, the length of the switching unit is 5 μm and the thickness of the GST is 10 nm. 71

Figure 6.4. Real-time optical transmission during Set and Reset processes. (a,b) real-time power of the applied electrical pulse (dashed line, same as in Figure 6.3) and corresponding normalized change in optical transmission of the simulated switching unit at 1550 nm (solid line) for crystallization (Set, a) and amorphization (Reset, b). Here, the length of the switching unit is 5 μm and the thickness of the GST is 10 nm. 72

Figure 6.5. Performance of the photonic switching units on waveguides. (a) I–V curves of the photonic switch with 20-nm-thick GST and a 4-μm-long active region obtained via current sweeps (0–15 mA) during and after the Set process, exhibiting a typical rectification behavior of PIN diodes without the electrical threshold switching effect. (b) Corresponding optical output under current sweeps at 1550 nm, showing an abrupt change during the Set process. (c) Optical output spectra of the same device after two reversible Set (0–15 mA sweep) and Reset (a single pulse of 4.3 V or ~200 mW for 100 ns) processes. The periodic fringes in the spectra are due to the back reflection between the input and output grating couplers. (d) Temporal trace of the transmission change in a photonic switch with 10-nm-thick GST and a 4-μm-long active region at 1550 nm during the consecutive Set (a single pulse of 3.4 V or ~8 mW for 1 ms with a falling edge of 0.6 ms) and Reset (a single pulse of 7.1 V or ~140 mW for 100 ns) steps. The sampling rate is ~50 Hz. (e) Cyclability of the transmission change of a photonic switch with 10-nm-thick GST and a 5-μm-long active region at 1550 nm under multiple Set (3.1 V or ~11 mW for 50 μs, 30-μs falling edge, ~715 nJ) and Reset (7 V or ~130 mW for 100 ns, ~13 nJ) cycles. Each pulse is temporally separated by more than 100 μs to ensure long enough thermal relaxation. The blue and orange shaded areas represent the two-standard-deviation intervals for the amorphous and crystalline states, respectively. aGST (cGST), amorphous (crystalline) GST. 74

Figure 6.6. Photonic switching units on microring resonators. (a) Top-view optical microscope image of the switching unit on an all-pass microring resonator. Inset: enlarged view of the ring. (b) SEM image of the black dashed area in the inset of (A). False color is used to highlight the GST (orange). S (G), signal (ground) electrode. p++ (n++), heavily doped p (n)-type silicon region. (c) Transmission spectra of a ring switch after a few reversible Set and Reset processes. (d) Cyclability of the transmission change and normalized transmission of a ring switch at 1549.57 nm under multiple Set and Reset cycles. Each pulse is temporally separated by more than 0.1 s. The blue and orange shaded areas represent the two-standard-deviation intervals for the amorphous and crystalline states, respectively. Here, the radius of the rings is 20 μm, the gap between the rings and the bus waveguides is 240 nm, the length of the switching units is 3 μm, and the thickness of the GST is 10 nm. Set, a single pulse of 1 V or ~0.6 mW for 100 μs with a falling edge of 60 μs, ~78 nJ. Reset, a single pulse of 2.5 V or ~80 mW for 100 ns, ~8 nJ. aGST (cGST), amorphous (crystalline) GST. 76

Figure 6.7. Insertion loss analysis based on experimental results. (a) Insertion loss (IL) spectra introduced by each important fabrication step and extinction ratio (ER) between two states of a photonic switching unit on a waveguide with 10-nm-thick GST and a 5-μm-long active region (same device as in Figure 6.5e). (b) Loss from each important fabrication step and loss modulation of microring resonators with different lengths of switching units near 1550 nm. Here, the radius of the rings is 20 μm, the gaps between the rings and the bus waveguides are 240 nm, 270 nm, or 330 nm, and the thickness of the GST is 10 nm. Every dot represents the experiment data of a single device. The dotted lines are the linear fitting of the experiments. 79

Figure 6.8. Heating dynamics of the photonic switching unit on the waveguide. (a) Electrical pulses (upper panel), corresponding transmission response (middle panel) and its normalization (lower panel) of the switching unit at 1550 nm for pulse amplitude modulation (PAM). (b) Electrical pulses (upper panel) and normalized transmission response (lower panel) of the switching unit at 1550 nm for pulse width modulation (PWM). The curves of the electrical pulses with different pulse widths have been vertically offset for clarity. Inset of lower panel: extracted dead time (1/e cooling time) as a function of pulse width with 95% confidence bounds. Here, the length of the switching unit is 5 μm and the thickness of the GST is 10 nm (same device as in Figure 6.3). The pulse energy was chosen to be sufficiently low to prevent any phase transition. 81

Figure 6.9. Heating dynamics of the switching unit on the microring resonator. (a) Electrical pulse (upper panel) and corresponding transmission response (lower panel) of the ring measured at different wavelengths. Inset of upper panel: transmission spectrum of the ring without any voltage applied. The probe wavelengths are annotated in the spectrum by the arrows using the same colors as in the lower panel. (b) Zoom-in inspection of the grey dashed area in (a), indicating a combination of the free-carrier effect and cavity oscillatory behavior in response to the step signal. Here, the radius of the ring is 20 μm, the gap between the rings and the bus waveguides is 330 nm, the length of the switching unit is 2 μm, and the thickness of the GST is 10 nm. The pulse energy was chosen to be sufficiently low to prevent any phase transition. 82

LIST OF TABLES

Table 5.1. Main Material Parameters Used in Simulations* 44

Table 5.2. Performance Comparison of the PINCs with Different Heaters* 60

Table 6.1. Main Material Parameters Used in the Chapter* 69

Table 6.2. Simulated Complex Effective Index and Attenuation Coefficient of the Photonic Switching Unit after Each Important Fabrication Step at 1550 nm..................................78

ACKNOWLEDGEMENTS

As time goes by, it has come to the end of my five years' doctorate study at the University of Washington. Through this special experience in my life, I have not only learned a lot in research but also become more mature in dealing with different kinds of affairs and getting along with others. I would not obtain such achievements without the help of my advisor, teachers, collaborators. colleagues, friends, and family. In this section, I would like to take this opportunity to show my sincere gratitude to all of them.

My greatest thanks are owed to my dear advisor Professor Arka Majumdar. When I just came to America, I did not speak English well and was not very familiar with the culture and many regular procedures in the US. It was Arka who provided me invaluable help to get through this difficult time. As Arka's first international student, I always receive great advice and care from him for every important affair, ranging from study plans to job searching. In terms of research, Arka, as a wise and energetic scholar, is always accessible to afford me timely help and sufficient resources to complete my projects. His kind support and respect for my ideas and research interests have inspired me to become a confident and outstanding researcher. For all of these, I am incredibly grateful to him.

The faculty at the university have provided me with excellent instruction. Here, I would like to especially thank my committee members, Professors Scott Dunham, Lih-Yuan Lin, and Peter Pauzauskie for their time and advice. The staff at the university have also provided me much convenience and a good environment to study and research. I would like to thank the staff in our department including Brenda Larson for their hard work and patience. I would also like to appreciate all the staff at the Washington Nanofabrication Facility including Darick Baker, Mark Morgan, Shane Patrick, Duane Irish, Richard Bojko, and Mark Brunson as well as those at the Molecular Analysis Facility including Micah Glaz. It is their efforts of training and maintenance that make my thoughts become a reality. I would also like to acknowledge my collaborators: Professor Peipeng Xu at Ningbo University for his insight in photonics especially in photonic crystal cavities, Professor Chang-Hua Liu at National Tsing Hua University for his experience in 2D materials, Professor Scott Dunham and Shifeng Zhu for their knowledge in semiconductor physics and process simulations, Prof. Lih-Yuan Lin and Chen Zou for their help in solution making, Professor Mo Li and Changming Wu for their help in dynamics measurement setup, Professor Nicholas Boechler and Amey Khanolkar at UCSD for their help in optical pumping, Professor Eric Pop and Sanchit Deshmukh at Stanford University for their suggestions in electrical switching, Jason Myers and Jesse Frantz at Naval Research Laboratory and Joshua Hendrickson at Air Force Research Laboratory for their exploration in phase-change materials, and Jonathan Doylend at Intel for his supervision and advice in the phase-change material project.

My groupmates in the lab and friends deserve my honest acknowledgements too. I would like to especially thank Taylor Fryett, Alan Zhan, and Shane Colburn. They gave me significant support to overcome the challenges of my project at the early stage. I would also like to thank my groupmates Roger Fang, Dan Guo, Chuchuan Hong, Yueyang Chen, James Whitehead, Zheyi Han, Albert Ryou, Elyas Bayati, David Rosser, Luocheng Huang, Abhi Saxena, Max Zhelyeznyakov, Shreyas Shah, Chris Munley, Yun Gao, Jiaming Li, Tristan Tan, Vishal Vashishtha, Jacob Waelder, Zane Peycke, and Michael Choquer as well as my friends Ruoming

Peng, Jinlin Xiang, Rui Xue, Xiaoshun Zeng, Xiudi Li, Yicheng Li, Peiran Liu, and Peifeng Jing for their help, care, and company.

I would like to thank my mother Qinwei Chen and my dad Jianxun Zheng, who support me both spiritually and physically to keep pursuing my dream. My deep gratitude belongs to them for their selfless dedication.

Last but not least, I would like to acknowledge the University of Washington and Seattle. The beautiful and diverse environment here enables me to develop myself with full comfort and freedom.

Thank all of the above who make me grow and let me enjoy the important five years in my life. Although this chapter of my life is going to be the end, their help will continue having a lot of positive impact on me that will support me to overcome the obstacles in the future.

Chapter 1.

INTRODUCTION

The emerging applications such as artificial intelligence, 5G, Internet of things, autonomous vehicles, and smart wearables have recently posed a challenge to modern computing technology due to their requirement of high-throughput, energy-efficient, and data-intensive information processing. Whereas the blossom of Moore's law (*i.e.* the number of the transistors on a chip doubles around every two years) in the semiconductor industry has brought about an increase in the processing speed at reduced cost and power consumption per transistor for more than fifty years, this is not the case any longer [1]. In fact, in the early 2000s, as the features began to shrink below ~90 nm, the clock frequency was limited up to a few gigahertz to avoid the exponentially increased power consumption due to the overwhelming heat from current leakage and metallic interconnect loss [1,2]. As a result of this breakdown of Dennard scaling (*i.e.* the power density stays constant as transistors get smaller), multicore processors have been adopted to keep the chips moving along Moore's law. However, with the shrinkage of transistors, inevitable heat generation stuck in the same small area of a chip has once again become a serious problem not to be ignored and the electron behavior will be governed by quantum uncertainties that will make computing components unreliable [1]. In addition, the power consumption and latency for signal transmission between transistors do not scale down in the same way as those within each transistor so that they begin to dominate the performance of the whole system [2]. What makes it worse is that modern computer systems are primarily based on the von Neumann architecture (*i.e.* the operations of processing and memory separate in time and space) requiring constant data transfer between the central processing unit (CPU) and memory. This leads to the so-called von Neumann bottleneck that limits the effective processing speed and wastes a lot of energy [3]. The industry and academia are therefore resorting to advanced technology and basic science including novel materials [4-6], computing architectures [7,8], and computing mechanisms [9-11] for next-generation computers.

1.1 PHOTONIC INFORMATION PROCESSING: OPPORTUNITIES AND CHALLENGES

Among all the candidates, photonic integrated circuits (PICs), in particular, silicon photonics (*i.e.* the study and application of integrated photonic systems where silicon is used as the optical medium) [12], have been considered to be an ideal solution and extensively studied for the booming applications in the past decades. Benefiting from the low-loss broadband transmission, PICs have demonstrated advantages over electronics in information transport including telecommunication and data center interconnects. Recently, thanks to the remarkable advances in nanofabrication [13], the level of complexity of photonic integration has reached a new height, shedding light on the future electronic-photonic systems on a chip [14-16]. The availability of large-scale PICs is thus offering PICs new opportunity to compete with electronic systems in energy-efficient high-throughput data processing, especially for emerging applications such as neuromorphic computing [17], quantum information [16,18], and microwave photonics [19,20].

Specifically, photonic information processing is superior to conventional electronic computing for the following reasons:

- Low latency: Photons travel one or two orders of magnitude faster than electrons on a chip meaning that it is possible to conduct information processing and propagation at the speed of light [2].
- Low loss: Without current that causes Joule heating in circuits, optical devices inherently enable low-loss communication and information processing with little or no energy consumption [21,22].

- Parallel operation: With different degrees of freedom including wavelength, amplitude, phase, mode, polarization, and orbital angular momentum, photons as bosons allow unique multiplexing techniques to significantly extend the computing capacity (bandwidth) [23,24].
- High speed: Unlike transistors, the power consumption of optical devices is only linearly proportional to the clock frequency [2]. Much higher modulation speeds can thus be achieved limited only by the intrinsic bandwidth (tens of gigahertz) of on-chip optical modulators and photodetectors.

Analogous to field-programmable gate arrays (FPGAs) in electronics, success in photonic information processing usually requires large-scale programmable PICs that have low-energy, compact, and high-speed building blocks with ultra-low insertion loss and precise control [25-27]. Such general-purpose PICs usually consist of a mesh of photonic switches that can be reconfigured on demand to the bar, cross, or coupler states [26-28] to provide different functionalities such as universal linear transformation [26,27], enabling excellent flexibility and cost-effective mass manufacturing. Whereas numerous programmable photonic systems have been reported [17-20,28], limited tunability of the systems is exhibited due to the weak thermo-optic [29,30] or electro-optic [31,32] effects of the materials (with the refractive index change Δn usually less than 0.01), leading to high energy consumption (typically several milliwatts) and large chip footprints (at least few tens of microns for the length of active regions). Microelectromechanical systems (MEMS) [33] or resonator-based systems [34,35] can help improve the modulation strength, but they suffer from either a large actuation voltage up to 40 V or narrow optical bandwidth as well as high sensitivity to fabrication and temperature variations [36]. The volatile reconfigurability or lack of memory of these PICs also necessitates a continuous power supply rendering the systems energy-inefficient. Besides, there exist many other challenges for current programmable photonic systems such as the inevitable packaging/alignment issue, lacking efficient optical nonlinearity, and the electro-optic signal conversion issue that introduces extra latency and energy consumption [37].

1.2 THE RISE OF PHASE-CHANGE MATERIALS

To address the first two challenges (limited tunability and lack of memory), it is highly desirable to explore other active photonic materials with strong optical modulation and self-holding characteristics. Chalcogenide phase-change materials (PCMs) such as the well-known $Ge_2Sb_2Te_5$ (GST) are one of the promising candidates [38-40] because of their following exceptional properties:

- Strong tunability: Upon structural phase transitions between the covalent-bonded amorphous state and the resonant-bonded crystalline state, PCMs exhibit substantial contrast in electrical resistivity [41] and optical constants (usually $\Delta n > 1$) over a broad wavelength range from the visible to infrared (IR) spectral region [38,39,42]. Additionally, by carefully controlling the excitation signal, intermediate states between the two states can be reached.
- Nonvolatility (long retention): Once switched, the resulting state can be retained for more than ten years under ambient conditions in no need of any external power supply [41,43].
- High-performance switching: Phase transitions of PCMs can be reversibly actuated by ultra-short optical or electrical pulses (picosecond to sub-nanosecond timescale for amorphization and sub-nanosecond to nanosecond timescale for crystallization) [44-46] with high cyclability (potentially up to 10^{15} switching cycles) [47,48] and low energy (down to femtojoules per bit or ~10 aJ/nm^3) [39,49-51].

- Excellent scalability: PCMs can be shrunk to the nanoscale [52] and are extremely easy to scale up because of their compatibility with other substrates without the "lattice mismatch" issue as the as-deposited PCMs are usually in the amorphous state. Actually, they have already been commercially used for optical rewritable discs and electronic memories.

Therefore, PCMs can potentially enable ultra-compact [48,53-57], broadband [39,48,55], multi-level [3,39,56-63], ultra-fast, long-endurance [48], and large-scale operations for programmable photonics without static energy consumption. By integrating PCMs with silicon or silicon nitride waveguides, several research groups have reported a variety of applications such as optical switches/modulators [39,48,53-57,61,64-68], photonic memories [58,60,62,69,70], and optical computing [3,23,24,59,63,71,72]. Recently, mixed-mode operations [51,73] and tunable volatility [74] of PCMs have also been demonstrated. However, previous PCM-based integrated photonic applications are still limited to single devices or simple PICs mainly due to the poor scalability of the optical or electrical actuation approaches (see Chapter 5). To scale up the PCM-integrated photonic devices to a much higher complexity as required by the future on-chip photonic information processing, it is important to build a nonvolatile integrated phase-change photonic platform with highly scalable photonic switching units as building blocks. To achieve this goal, multi-level, broadband multi-port switches with efficient electrical control are needed.

1.3 CONTENTS AND HIGHLIGHTS

In this dissertation, a nonvolatile integrated phase-change photonic platform based on GST-clad silicon photonic devices and its essential techniques to support chip-scale programmable PICs are both theoretically and experimentally studied. Specifically, the main contents and highlights of the dissertation are as follows.

- Chapter 2 focuses on the structure, fabrication, and static optical characterization of the GST-on-silicon hybrid integrated nanophotonic platform [39]. Utilizing the GST-clad silicon microring resonators, both the strong broadband attenuation modulation (7.3 dB/μm) and optical phase modulation (0.70 nm/μm) effects induced by the GST are characterized and the complex refractive indices of the GST are accordingly inferred. This is the first time the fundamental properties of the GST-on-silicon platform are systematically explored. The results also indicate that it is possible to use resonators to characterize the properties of materials on the nanoscale.
- Chapter 3 addresses the experimental setup and process of all-optical, reversible, and quasi-continuous (multi-level) programming of the GST-on-silicon platform, which was rarely shown before this work, by adjusting the energy and number of free-space laser pulses applied to the GST [39]. Designed to achieve near critical coupling when the GST is in the amorphous state, a nonvolatile multi-level microring-based switch with a high extinction ratio (ER) up to 33 dB is thus demonstrated.
- Chapter 4 extends the platform to a multi-port and broadband scheme where compact (~30 μm), low-loss (~1 dB), and broadband (over 30 nm with cross talk less than −10 dB) 1 × 2 and 2 × 2 switches are demonstrated [55]. Based on the asymmetric directional coupler structure [75,76], the presented switches can circumvent the high loss associated with the crystalline GST. The reported switches can function as the building blocks of the future large-scale PCM-based programmable photonic networks.
- Chapter 5 provides the model and analysis of electrical switching of the GST-on-silicon platform with different heaters including graphene, indium tin oxide (ITO), and silicon PIN diode (p-type, intrinsic, n-type junction) heaters that allows large-scale integration and

large-area switching [77]. Thanks to the ultra-low heat capacity and high in-plane thermal conductivity of graphene [78,79], the proposed heating structures exhibit a high switching speed of ~80 MHz and high energy efficiency of 19.2 aJ/nm^3 (6.6 aJ/nm^3) for crystallization (amorphization) while achieving complete phase transitions to ensure strong attenuation (~6.46 dB/μm) and optical phase (~0.28 π/μm at 1550 nm) modulation. Compared with ITO and silicon PIN diode heaters, the structures with graphene heaters display two orders of magnitude higher figure of merits for heating and overall performance. This work facilitates the analysis and understanding of the thermal-conduction heating-enabled phase transitions on PICs and supports the development of the future large-scale PCM-based electronic-photonic systems.

- Chapter 6 presents the experiment of electrical switching with silicon PIN diode heaters proposed in Chapter 5 [48]. Using GST-clad silicon waveguides and microring resonators, intrinsically compact and energy-efficient photonic switching units operated with low driving voltages (down to 1 V for crystallization and 2.5 V for amorphization), near-zero additional loss (~0.02 dB/μm), and reversible switching with long endurance (more than 1000 phase transitions) are obtained in a complementary metal-oxide-semiconductor (CMOS)-compatible process. This work can potentially enable very large-scale CMOS-integrated programmable electronic-photonic systems such as optical neural networks (ONN) and general-purpose integrated photonic processors (optical FPGAs).
- Chapter 7 concludes the above work and points out several tentative directions to improve the current nonvolatile integrated phase-change photonic platform as future work. Challenges and outlook will be included.

Note that part of the dissertation is adapted with permission from my previous publications. Chapter 2 and Chapter 3 are adapted from Ref. [39]. Copyright 2018 Optical Society of America. Chapter 4 is adapted with permission from Ref. [55]. Copyright 2019 American Chemical Society. Chapter 5 is adapted with permission from Ref. [77]. Copyright 2020 American Chemical Society. Chapter 6 is adapted with permission from Ref. [48]. Copyright 2020 Wiley-VCH.

Chapter 2.

NONVOLATILE INTEGRATED PHASE-CHANGE PHOTONIC PLATFORM

This chapter studies the nonvolatile integrated phase-change photonic platform built for the large-scale programmable photonic systems, including the design, fabrication, and static optical characterization. This chapter provides the fundamentals to the integrated phase-change photonic devices and paves the way for the essential techniques of the platform that will be discussed in the following chapters. Note that this chapter is partially adapted from Ref. [39]. Copyright 2018 Optical Society of America.

2.1 CHARACTERIZATION OF GST

To better understand the properties of the hybrid material platform and have a reliable reference for the subsequent simulation and experiment, it is necessary to separately characterize PCMs using standard metrological methods such as ellipsometry and X-ray diffraction (XRD) measurements. As the platform employs GST as the tunable material, the thin-film GST layer was measured.

In this experiment, ellipsometry (Woollam-M-2000) and XRD measurements (D8 Discover Microfocus) were conducted for a 20-nm-thick (measured by ellipsometry) blank GST layer that was deposited on a silicon wafer using a GST target (AJA International) in a magnetron sputtering system (Lesker Lab 18). As shown in Figure 2.1a, the extracted optical constants from the ellipsometer have high contrast over a broad spectral region between the as-deposited GST and the GST after rapid thermal annealing (RTA, AccuThermo AW 610) the chip at 200 ℃ for 10 mins in a N_2 atmosphere. The results agree well with the previously measured values for amorphous GST (aGST) and crystalline GST (cGST), respectively [38,42]. The XRD data in Figure 2.1b show that the XRD distribution changed from a disordered aGST pattern to a typical diffraction pattern of fcc-cGST after RTA with four characteristic peaks [80]. The strong signal near 70° in Figure 2.1b is from the silicon substrate, which covers the (420) peak of cGST.

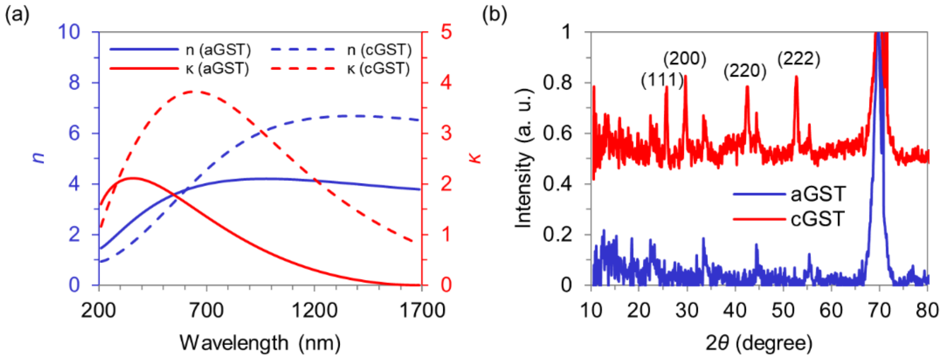

Figure 2.1. GST characterization. (a) Complex refractive index of aGST and cGST as a function of wavelength. (b) XRD data of aGST and cGST. The curve of cGST is offset vertically for clarity.

2.2 DESIGN AND FABRICATION

With the properties of GST thin film being characterized, we are capable of researching on the nonvolatile integrated phase-change photonic platform in the following sections.

As illustrated in Figure 2.2a, we integrate the GST with silicon rib waveguides where light is evanescently coupled with the GST to form the GST-on-silicon hybrid integrated nanophotonic platform. Due to the dramatic difference in the complex refractive index between aGST and cGST, the mode profile and complex effective index ($\tilde{n}_{\mathrm{eff}} = n_{\mathrm{eff}} - \kappa_{\mathrm{eff}}\, i$) of the hybrid waveguide will be strongly modified once the GST is switched between two states, as is shown in Figure 2.2b,c. The transmission and phase properties of hybrid silicon PICs using such a structure can thus be significantly altered. Note that the simulations are performed using a frequency-domain two-dimensional (2D) finite-element method (FEM) wave optics model through the mode analysis (eigenvalue solver) in a commercially available software COMSOL Multiphysics. The perfectly matched layer domains are adopted for the boundary regions of the model with the scattering boundary conditions applied to all the external boundaries.

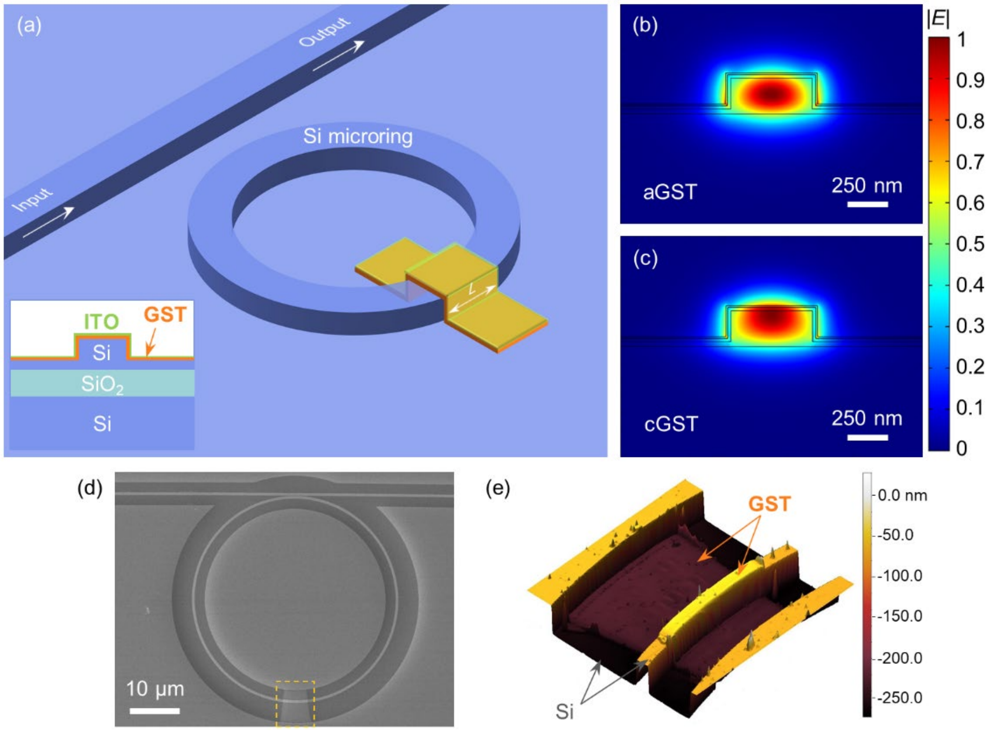

Figure 2.2. GST-on-silicon hybrid integrated nanophotonic platform. (a) Schematic of the platform. Inset: cross-section of the hybrid waveguide. To emphasize the gap between the waveguide and the ring, the schematic is not in scale. (b,c) Fundamental quasi-transverse electric (TE) mode profiles (normalized amplitude profiles of the electric field) of the hybrid waveguide at 1550 nm for (b) aGST with $\tilde{n}_{\mathrm{eff}} = 2.62 - 0.0024$ i and (c) cGST with $\tilde{n}_{\mathrm{eff}} = 2.97 - 0.22$ i. Both were simulated with frequency-domain FEM using the optical constants of GST and ITO measured by ellipsometry. (d) SEM image of a microring with 5 μm as-deposited GST. (e) AFM height map of the region highlighted by the yellow dashed rectangle in (d).

We fabricated the hybrid platform on a commercial silicon-on-insulator (SOI) wafer (Soitec) with a 220-nm-thick silicon layer on top of a 3-μm-thick buried oxide layer. The pattern, including the 500-nm-wide waveguides, microring resonators, and grating couplers, was defined by a JEOL JBX-6300FS 100kV electron-beam lithography (EBL) system using positive tone ZEP-520A resist. After development, 190 nm partially etched rib waveguides were made by an inductively coupled plasma reactive ion etching (ICP-RIE, Oxford PlasmaLab 100 ICP-180) process exploiting mixed gas of SF_6 and C_4F_8. The partially etched design is chosen to reduce the step height for the GST deposition later in the process and to enhance the coupling between the bus waveguides and microrings. The enhanced coupling maintains the critical coupling condition (where the roundtrip loss rate is the same as the coupling rate) of the microring resonators [81] in the presence of high loss from the GST. The devices were then measured to obtain the reference transmission spectra. A second EBL exposure using positive tone poly(methyl methacrylate) (PMMA) resist was subsequently carried out to create windows for the GST deposition. After development, 20 nm GST was sputtered onto the chip and then capped with 11 nm ITO to protect the GST from oxidation. The deposited ITO layer here is relatively transparent over the visible and near-IR spectral region according to ellipsometry measurements (extinction coefficient $\kappa < 0.002$ from 480 nm to 1700 nm, and much smaller than that of GST in the amorphous and crystalline state). Finally, the lift-off of the GST/ITO layers was completed using methylene chloride. Figure 2.2d shows a scanning electron microscope (SEM) image of one fabricated microring resonator partially covered with an as-deposited GST strip (length L = 5 μm). Using atomic force microscopy (AFM), as is shown in Figure 2.2e, we confirmed a 31-nm-thick smooth thin film of GST/ITO was deposited on the silicon waveguide with an average root-mean-square (RMS) surface roughness of 2.2 nm (which is much shorter than the wavelength of interest).

2.3 CHARACTERIZATION OF THE PLATFORM

To characterize the properties of the GST-on-silicon platform, we measured the transmission spectrum of 40 microring resonators (with a radius of 20 μm and a gap of 100 nm between the bus waveguide and the microring) covered with various lengths of GST using a vertical fiber-coupling setup. Focusing sub-wavelength grating couplers [82] were utilized to polarization-selectively couple light from a tunable continuous-wave laser (Santec TSL-510) to the waveguides and collect light on the other side of the waveguides into a low-noise power meter (Keysight 81634B) via single-mode fibers (SMFs) operated at an angle of ~32 degrees. The power of the coupled light was kept low enough (< 100 μW) to prevent any phase transition of the GST and minimize the thermo-optic effects of the GST [83] and silicon [84]. The polarization of the input light was controlled to match the fundamental quasi-TE mode of the waveguide by a manual fiber polarization controller (Thorlabs FPC526). The temperature of the test stage was fixed at ~20 °C using a thermoelectric controller (TEC, TE Technology TC-720), so as to avoid any thermal shift of the resonators. For each device, we performed the transmission measurement: (i) before the GST deposition to record the intrinsic loss and resonance wavelength of each microring, (ii) right after the GST deposition (which is aGST), and then (iii) after RTA the chip to change the GST from the amorphous to the crystalline state.

Figure 2.3a shows the representative output spectra of microring resonators in the amorphous and crystalline states which are strongly related to the state and the length of the GST. Two spectra, corresponding to aGST and cGST, for each length of GST are plotted on the same scale, where each set corresponding to a different length is vertically offset for clarity. In both states, with an increase of the GST length *L* (shown on the right axis of the plot), the linewidths of the resonance dips broaden, corresponding to the increase in loss, and a red-shift of the spectrum is observed, corresponding to the increase in the effective index. Similar broadening and red-shift of the resonances can be observed for every microring upon switching the GST from the amorphous to the crystalline state. The absorptive and refractive modulation effects introduced by the GST are so substantial that we observe a distinct color change between aGST and cGST under an optical microscope, as shown in Figure 2.3b,c. We note that with increased length of the GST, the roundtrip loss rate increases, while the coupling rate between the waveguide and the ring remains the same. Hence, the ring resonator goes from being over-coupled, to critically coupled, then under-coupled. This can be observed from Figure 2.3a, where the transmission dip changes depending on the length of aGST.

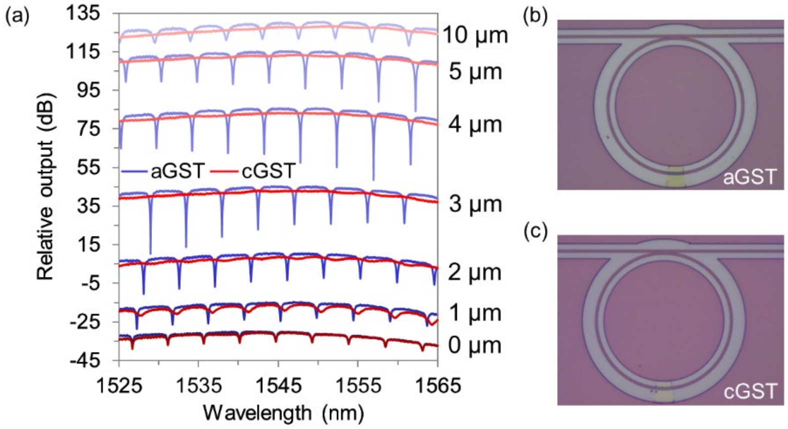

Figure 2.3. Transmission measurement of the microrings with GST. (a) Representative output spectra of microrings with different length of GST for amorphous and crystalline states. For each length of GST, the cGST and aGST spectra are in scale, while each set of spectra for a different length of GST is offset vertically for clarity. (b,c) Microscope images of a microring with 5 μm (b) aGST and (c) cGST.

To quantitatively describe the modulation effects, we extracted the quality factor (*Q*) and resonance wavelength of each dip by fitting the measured resonances to a Lorentzian lineshape function (Figure 2.4a). We could not fit the data of the microrings with cGST of length $L > 2$ μm since the visibility of the resonance is significantly reduced due to strong attenuation from the cGST, as is shown in Figure 2.3a. As the quality factor and the free spectral range (FSR) of the bare silicon microring (without any GST) remain unchanged throughout the fabrication process (the plot denoted as “0 μm” GST in Figure 2.3a), we assume that the intrinsic loss (composed of scattering loss, material absorption loss, and bending loss) of the microrings remains unchanged after the GST deposition and RTA. The loss introduced by GST can then be estimated as the difference in the loss of the microring before and after GST deposition [85]:

$$\text{Loss} = \alpha L + \alpha_0 \approx 2\pi R \cdot \frac{2\pi n_{\text{g}}}{\lambda_0} \cdot \left(\frac{1}{Q} - \frac{1}{Q_0}\right) = \frac{2\pi\lambda_0}{\text{FSR}} \cdot \left(\frac{1}{Q} - \frac{1}{Q_0}\right) \tag{1}$$

where α is the attenuation coefficient of the GST-on-silicon hybrid waveguide, α_0 is the mode mismatch loss between the regular silicon waveguide and the hybrid waveguide, $R = 20$ µm is the radius of the microrings, λ_0 is the resonance wavelength, Q_0 and Q are the quality factor of the same microring before and after the GST deposition, FSR is the free spectral range of the microring, and $n_{\text{g}} = \lambda_0^2/(\text{FSR}\cdot 2\pi R)$ is the group index averaged over the whole ring with partial GST coverage. Here, the change in FSR and n_{g} due to the GST deposition is neglected because of the limited coverage area of GST on the microrings. As plotted in Figure 2.4b, the GST-introduced loss is linearly proportional to the length of the GST. From this, we obtained the attenuation coefficient of the hybrid waveguide near 1550 nm to be $\alpha_{\text{aGST}} = 0.27 \pm 0.04$ dB/µm for aGST and $\alpha_{\text{cGST}} = 7.6 \pm 1.0$ dB/µm for cGST. The uncertainty noted is obtained from the upper and lower limit of the confidence interval (95%) for estimated parameters by linear regression analysis. Therefore, the attenuation modulation effect from aGST to cGST is around 7.3 dB/µm. Compared with the simulation results, the experimental attenuation coefficient for cGST agrees quite well with the theoretical value of 7.7 dB/µm, whereas that for aGST is much larger than the expected 0.08 dB/µm. We attribute this inconsistency to the unwanted scattering loss due to the surface roughness of GST. The scattering loss is negligible when the device is in the lossy crystalline state. However, it becomes dominant when the absorption rate of GST is relatively small in the amorphous state. The extracted mode mismatch loss is less than 0.5 dB in both states and is ignored in calculating the attenuation coefficient using Eq. (1) except in the amorphous state.

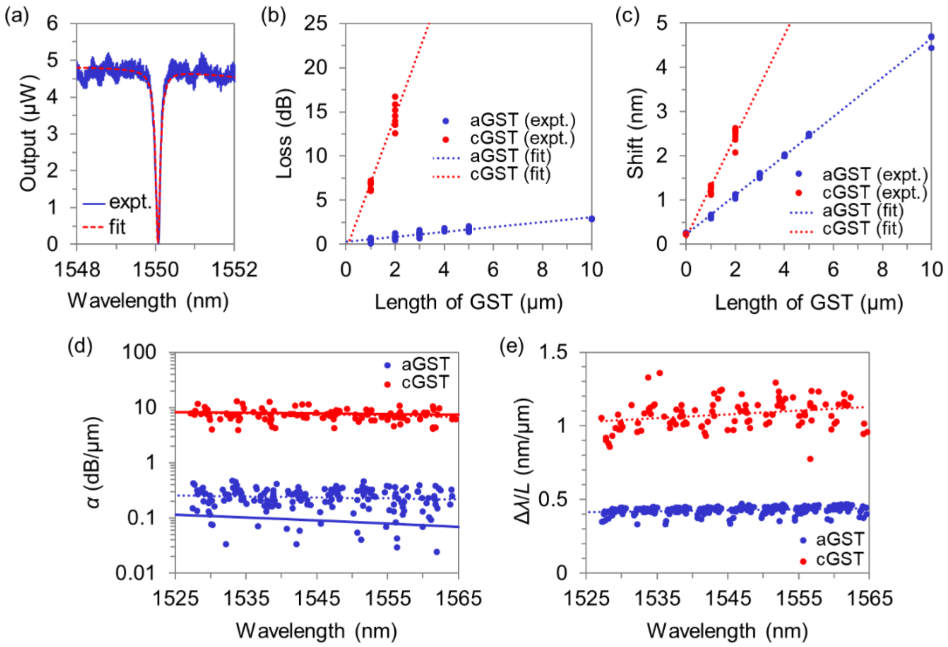

Figure 2.4. Characterization of the GST-on-silicon platform using microring resonators. (a) Lorentzian fitting of the spectrum for the resonance dips in a ring with Q ~11,000 near 1550 nm. (b,c) GST length-dependent (b) loss and (c) spectral shift of the microrings for aGST and cGST with respect to those of the intrinsic microrings. Every dot represents a single device. (d,e) Wavelength-dependent (d) attenuation coefficient and (e) resonance shift per unit GST length for aGST and cGST with respect to the reference (before GST deposition). Dots: experiment data. Dotted lines: linear fitting. Solid lines: simulation.

The linear increase of the red spectral shift ($\Delta\lambda$) with respect to the reference (before GST deposition) as a function of the GST length is shown in Figure 2.4c. We fit the resonance shifts per unit GST length $\Delta\lambda/L$ near 1550 nm to be 0.444 ± 0.007 nm/μm and 1.14 ± 0.12 nm/μm for aGST and cGST, respectively. Thus, the optical phase modulation effect from aGST to cGST is around 0.70 nm/μm. We observe that there is a residual shift of ~0.2 nm for every microring after the GST deposition, as is reflected by the non-zero shift at L = 0 μm. We attribute this to an irreversible modification of the ring resonators during the deposition process, possibly from residual resist left over from the lift-off process. The spectral shift can also be theoretically estimated [86] by

$$\frac{\Delta\lambda}{L} \approx \frac{\Delta n_{\mathrm{eff}}\lambda_0}{2\pi R n_{\mathrm{eff0}}} \tag{2}$$

where n_{eff0} is the real part of the effective index for the bare silicon waveguide, and Δn_{eff} is the real part of the effective index change. The effective index n_{eff0} instead of group index n_{g} is used because only a small portion of the ring resonator is modified, unlike the case described in [86]. According to the simulated waveguide modes, $\Delta\lambda/L$ are 0.98 nm/μm and 2.76 nm/μm for aGST and cGST, respectively. Potential causes for the discrepancy between the theory and experiment are: the modification of the GST refractive index upon shrinking the GST from the wafer size into a small scale, or a non-conformal coverage of GST due to the directionality of sputtering. From the experimental data, we estimate the refractive indices of the nano-patterned GST to be $n_{\mathrm{aGST}} \approx 2.58 - 0.12i$ and $n_{\mathrm{cGST}} \approx 4.68 - 1.92i$, whereas the pristine GST indices (measured by ellipsometry) are $n_{\mathrm{aGST}} = 3.89 - 0.02i$ and $n_{\mathrm{cGST}} = 6.63 - 1.09i$. The increased imaginary value for aGST is, however, primarily due to the extra scattering loss as described before. Note that, measurement of refractive indices of nano-patterned GST is generally difficult and our results indicate that high-Q resonators can potentially be used to characterize properties of materials on the nanoscale.

Figure 2.4d,e summarize the extracted attenuation coefficient and the resonance shift per unit GST length as a function of the wavelength. Both the attenuation coefficient and the resonance shift exhibit broadband behavior over the whole C band (1530 nm-1565 nm) for both aGST and cGST, as was expected from the simulations. Notably, a close match was observed between the simulation line and the linear fitting line of experimental data for the attenuation coefficient of cGST.

2.4 SUMMARY

In this chapter, we report a nonvolatile integrated phase-change photonic platform using GST-clad silicon waveguides and microring resonators. The platform exhibits strong broadband attenuation modulation (7.3 dB/μm) and optical phase modulation (0.70 nm/μm) effects induced by GST. The method we exploited for characterization is of universal significance for the study of new materials and is the basis for further exploration.

Chapter 3.

ALL-OPTICAL MULTI-LEVEL OPERATION

The state of GST can be reversibly programmed by the application of heat via optical or electrical pulses. However, multi-level optical switching of the GST on silicon platform was rarely shown. This chapter focuses on the all-optical multi-level operation of the GST-on-silicon platform. Based on the switching approach, an all-optical multi-level microring-based switch is demonstrated. Note that this chapter is partially adapted from Ref. [39]. Copyright 2018 Optical Society of America.

3.1 ALL-OPTICAL SWITCHING

We explore reversible and quasi-continuous tuning of the GST-on-silicon platform by a 532-nm actively *Q*-switched pulsed diode-pumped solid-state (DPSS) laser (Coherent HELIOS 532-3-50) with 440 ps pulse duration. As illustrated in Figure 3.1a, an optical imaging system was used to locate the devices of interest under white light. Once the CCD camera, the beam splitter (BS), and the objective were moved away to avoid laser damage, the setup became an optical pumping system (Figure 3.1b) enabling the pulsed laser to switch the GST. The pump energy of the optical pulses was adjusted by a variable neutral-density (ND) filter and a half-wave plate (HWP), along with a polarizing beam splitter (PBS). Rotating the HWP in the beam path rotated the polarization of the pump laser, the vertical component of which was transmitted to the sample by after passing through the PBS. The pump energy was measured by a laser power meter (Coherent FieldMaxII-TO) with a thermopile sensor (Coherent PM10). The number and repetition rate of the pulses were controlled by providing a TTL signal to the *Q*-switch of the laser using a dual channel arbitrary function generator (Tektronix AFG3022B). In order to align the laser beam spot (diameter ~120 μm) with the GST strip, we used the pump laser to burn a hole on the edge of the chip with consecutive high-energy pulses, marked the contour of the hole on the screen of the imaging system, and then moved the target GST strip to the center of the mark with a 3-axis stage. After optically heating the sample, the chip was taken back to the fiber setup for transmission measurement.

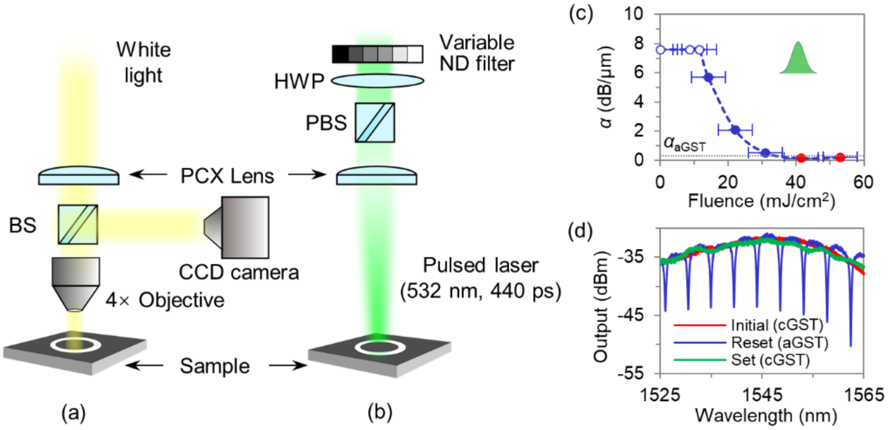
White light
Variable ND filter
HWP
PBS
PCX Lens
BS
CCD camera
4× Objective
Pulsed laser (532 nm, 440 ps)
Sample
(a)
(b)
(c)
α (dB/μm)
10
8
6
4
2
0
α_{aGST}
0
20
40
60
Fluence (mJ/cm²)
(d)
Output (dBm)
-35
-45
-55
Initial (cGST)
Reset (aGST)
Set (cGST)
1525
1545
1565
Wavelength (nm)

Figure 3.1. Determination of GST phase transition conditions by an optical heating setup. (a) Schematic of the optical imaging system. PCX Lens, plano-convex lens. (b) Schematic of the optical pumping system. (c) Induced attenuation coefficient as a function of the fluence of a single laser pulse. White, blue, and red dots denote devices that retained the crystalline state, had intermediate states of GST, and had damaged GST, respectively. Inset: the green Gaussian pulse denotes that only a single pulse was used for this experiment. (d) Sample output spectra of a microring with 4 μm GST in the determined Set and Reset conditions.

To realize quasi-continuous tuning of the hybrid platform, we first determined the Set (crystallization) and the Reset (amorphization) condition of the GST. For amorphization, the GST should be melted and then rapidly quenched to maintain its disordered state by a single short pulse. In contrast, heating the GST to just above its glass transition temperature (T_g), but below the melting point (T_m), by a long-enough sequence of short pulses or a single long pulse converts the lattice arrangement to a crystalline or partially crystalline state. We chose several microrings with the same length (L = 5 μm) of fully crystalline GST (after RTA) and illuminated the GST with a single pulse of different energies (a different pulse energy for each ring). The attenuation coefficient introduced by the GST was then extracted from the transmission spectrum. Because the attenuation coefficient reflects the state of GST or the degree of crystallization, the pulse that leads the attenuation coefficient to drop to around the previously fitted value of α_{aGST} (see Chapter 2) can serve as the Reset pulse. Similarly, the pulse of lower energy that maintained the initial crystalline GST attenuation coefficient α_{cGST} can be identified as an appropriate Set pulse. As is shown in Figure 3.1c, with the increase of the laser fluence, the attenuation coefficient decreases from α_{cGST} to a value below α_{aGST} (red dots in the figure), corresponding to damage to the GST, which was verified by microscope inspection. We estimate the error in our power measurements to be ~10 mJ/cm^2. Such a large error is primarily due to the free-space setup and can be potentially reduced by guiding the light on-chip. We chose the single Reset pulse fluence to be ~31 mJ/cm^2 which was below the damage fluence, and each of the Set pulses to be ~10 mJ/cm^2. To fully crystallize the GST, we applied 450 consecutive Set pulses with a repetition rate of 50 kHz to accumulate heat. These thermal conditions are comparable to those used previously [87] and justified by conducting the Reset and Set pulses back and forth several times on the same microring and comparing the attenuation coefficient to the fitted values. Figure 3.1d shows the typical spectra of one microring with 4 μm GST after the Set and Reset pulses. The single Reset pulse reduced the attenuation coefficient to 0.62 dB/μm, while the Set sequence successfully made the spectrum recover back to the initial state (cGST). Considering the effective area of the GST used in the hybrid waveguides, the equivalent energies of each pulse to switch the GST to amorphous and crystalline state are only ~620 pJ (~9 aJ/nm^3) and ~200 pJ (~3 aJ/nm^3), respectively, which are comparable to previous reports with similar volumes of GST [58,64]. We note that the energy-efficiency of our device for amorphization is only an order of magnitude larger than the fundamental limit, estimated to be ~1.2 aJ/nm^3 [47]. We emphasize that as the phase transition is nonvolatile, no more energy is needed after the switching process. This is where the PCM-based tuning mechanisms out-perform traditional thermo-optic or electro-optic mechanisms in terms of total energy-efficiency for programmable photonics.

3.2 MULTI-LEVEL OPERATION AND MICRORING-BASED SWITCH

The Set and Reset pulses allow us to control the hybrid platform in a quasi-continuous manner. As is shown in Figure 3.2, a microring with 2 μm of fully crystalline GST was pumped by a Reset pulse to convert the GST to the amorphous state. Since the loss of the microring for aGST is close to the transmission loss in the coupling region, the critical coupling condition was reached in the amorphous state, enabling deep dips in the transmission spectrum (Figure 3.2a,b). To achieve intermediate states, we exploited the heat accumulation effect by applying a succession of excitations each comprised of 25 set pulses to the GST on the microring. With the increase of the number of excitations, the resonance linewidths increased, the depth of the resonances diminished, and the resonances shifted to longer wavelengths, implying an increased fraction of crystallization in the GST. With five 25-set-pulse excitations, the spectrum of the microring is almost identical to that where the GST is in the fully crystalline state. Due to the remarkable absorptive and refractive modulation effects of GST, the transmission of the microring at 1551.5 nm shows a switching effect with an extinction ratio of 33 dB (Figure 3.2b). To justify the crystallization procedure, we extracted the attenuation coefficient of the hybrid waveguide at around 1551.5 nm, as is shown in Figure 3.2c. The attenuation coefficient gradually increased to ~7 dB/μm, which is close to the previously fitted value α_{cGST}. We repeated this experiment with several other rings, and observed similar qualitative behavior, although quantitative match was not obtained. We attribute this uncertainty to the small shifts in the relative position between the laser beam spot and the GST strip. Note that, although we achieved each intermediate state from its last state in one direction, our experiment implies that we can achieve any pre-defined intermediate states from fully crystalline GST by first applying a Reset pulse and then applying a variable number of Set pulses. Although packets of 25 pulses were used in our experiment, we note that reducing the number of Set pulses in each excitation, more intermediate states can be realized.

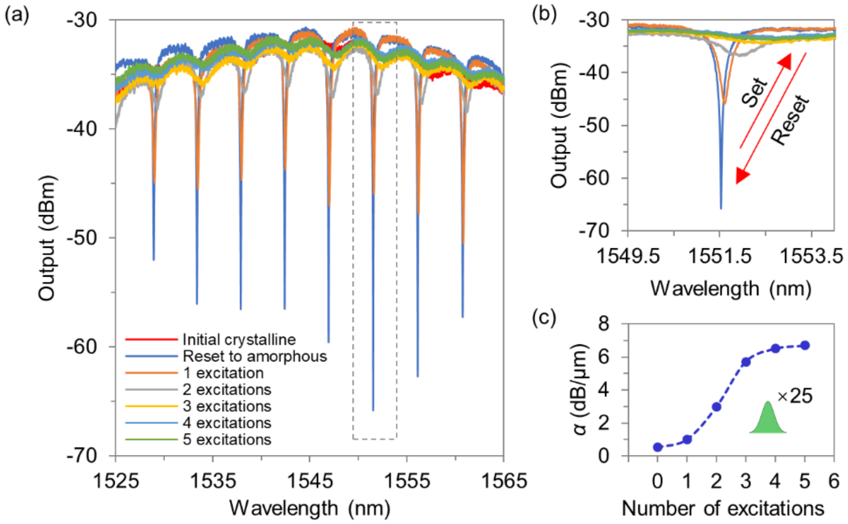

Figure 3.2. Quasi-continuous tuning of the GST-on-silicon hybrid integrated nanophotonic platform. (a) Output spectra of a microring with 2 μm GST under different number of excitations, where “excitation” denotes a packet of 25 consecutive pulses applied at 50 kHz repetition rate. (b) A zoom-in inspection of the region highlighted by the grey dashed rectangle in the spectra in (a). (c) Attenuation coefficient of the hybrid waveguide as a function of the number of excitations. Inset: the green Gaussian pulse with “×25” denote the excitation process.

3.3 SUMMARY

To summarize this chapter, with different pulse energy and number of laser pulses, it was shown that the GST on the hybrid platform can be reversibly switched between the amorphous and crystalline states and quasi-continuously tuned to several intermediate states. Based on this platform, a nonvolatile 1 × 1 microring photonic switch with a high extinction ratio up to 33 dB was demonstrated. This research is only a first step towards future large-scale programmable photonic networks. For instance, with appropriate design, a broadband low-loss 2 × 2 photonic switch [75] could be realized, which would be the building block for a future nonvolatile routing network and optical FPGA. It is worth noting that the free-space optical heating setup used in this work is not a scalable method for complex PICs (see Chapter 5). To flexibly control the phase transition, local electrical heating either using another transparent conductive material or silicon itself may be preferable [54,68], wherein mature CMOS electronics can be leveraged to make large-scale programmable electronic-photonic systems.

Chapter 4.

LOW-LOSS AND BROADBAND MULTI-PORT PHOTONIC SWITCHES

Resonator-based switches suffer from intrinsic narrow optical bandwidth as well as high sensitivity to fabrication imperfections and temperature fluctuations [36]. Practical applications of programmable PICs require photonic switches to have a multiport and broadband characteristic. Current experimental demonstrations of PCM-integrated switches, however, are either single-port [53,65,68] or narrow-band [39,64,67]. PCM-integrated Mach–Zehnder interferometer (MZI) switches can potentially afford broadband operation. Unfortunately, their performance including the crosstalk (CT, defined as the contrast ratio between the two output ports) and insertion loss (IL) will be dramatically sacrificed due to the large absorptive loss from crystalline PCMs.

In this chapter, we demonstrate low-loss and broadband 1 × 2 and 2 × 2 photonic switches based on the previously built GST-on-silicon platform and the asymmetric directional coupler (DC) switch design [75,76], bypassing the high loss associated with the crystalline state. Note that this chapter is adapted with permission from Ref. [55]. Copyright 2019 American Chemical Society.

4.1 1 × 2 PHOTONIC SWITCH

This section reports a 1 × 2 DC switch.

4.1.1 *Design and Simulation*

Figure 4.1a shows the schematic of the 1 × 2 DC switch. The asymmetric coupling region consists of a normal silicon strip waveguide (SW) and a GST-on-silicon hybrid waveguide (HW) where a thin layer of GST is placed on silicon. When the GST is in the low-loss amorphous state, the optimized structure of the silicon SW and the HW can meet the phase-matching condition (*i.e.* the mode effective index of the SW equals to that of the HW) for TE polarization, leading to the cross state of the switch with a low IL (Figure 4.1b). Once the GST is transformed to the lossy crystalline state, the phase-matching condition is significantly altered due to the strong modification of the mode in the HW induced by the dramatic difference of complex refractive indices between aGST and cGST (Figure 4.2a). As a result, light is diverted away from the HW forming the bar state of the switch with low attenuation ensured by minimal optical field interaction with the lossy GST layer (Figure 4.1c).

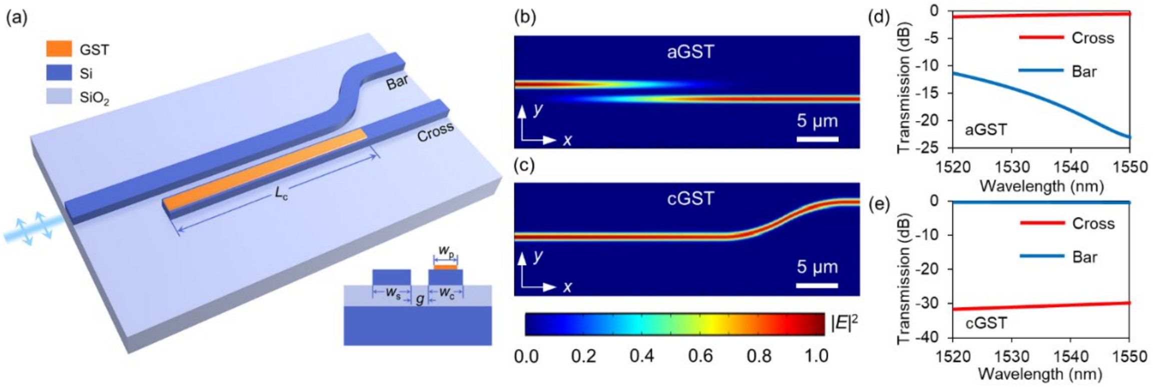

Figure 4.1. Simulation of the 1 × 2 DC switch. (a) Schematic of the switch. (b,c) Normalized optical field intensity distribution of the switch for (b) aGST and (c) cGST simulated at 1550 nm. (d,e) Calculated transmission spectra at the cross and bar ports for (d) aGST and (e) cGST.

To determine the widths of the waveguides (w_s, w_c) appropriately, we analyze the effective indices of the fundamental modes supported in the silicon SW and the GST-on-silicon HW with respect to their widths (Figure 4.2a). The simulations are performed using the frequency-domain FEM (COMSOL Multiphysics). The width of the silicon SW (w_s) is chosen as 450 nm to ensure single-mode operation. The width of the GST (w_p) is set to be 100 nm smaller than the core width of the HW (w_c), which can be easily achieved within the alignment precision of the electron-beam lithography (EBL). w_c is optimally chosen as 420 nm so that the phase-matching condition could be satisfied for aGST to achieve strong coupling between the two waveguides, which can be verified in Figure 4.2b,c. Therefore, the input TE-polarized light will be evanescently coupled to the cross port completely with an appropriate coupling length. On the contrary, with the GST switched to the lossy crystalline state, the huge effective index contrast between the two waveguides indicates a serious phase mismatch, resulting in two isolated modes as shown in Figure 4.2d,e.

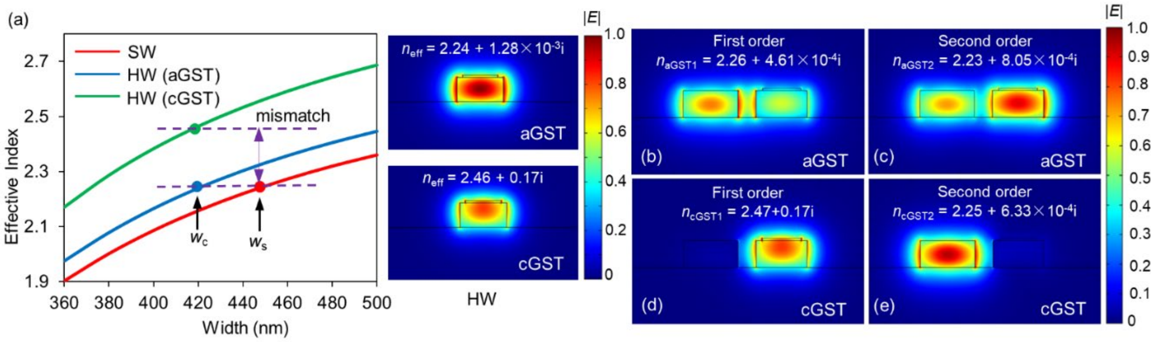

Figure 4.2. Mode analysis of the two-waveguide system. (a) Left: effective indices of the fundamental modes in the silicon SW and the HW. Right: the normalized electrical field profiles of the TE mode with GST in the amorphous and crystalline state. The widths of the SW and the HW are w_s = 450 nm and w_c = 420 nm, respectively. (b-e) Normalized electrical field profiles of the supermodes in the two-waveguide system when the GST is in (b,c) amorphous and (d,e) crystalline state. All the modes are simulated for TE polarization at 1550 nm.

Next, the characteristics of the coupling region are studied when varying the gap (g) between the silicon SW and HW. There exists a trade-off between the coupling length (L_c) and the insertion loss in the crystalline state (IL_{cGST}). IL_{cGST} is introduced to access the loss performance for cGST and is given by $IL_{cGST} = L_c \times \alpha_{cGST2}$, where L_c and α_{cGST2} denote the optimal coupling length corresponding to a specific g and attenuation coefficient of the second order supermode (Figure 4.2e). Figure 4.3 shows the L_c and IL_{cGST} as a function of the gap. As the gap increases, the coupling length in the amorphous state increases, while the insertion loss in the crystalline state decreases due to the weaker evanescent coupling between the two waveguides. Considering the trade-off and fabrication difficulty, a moderate g of 150 nm is chosen while ensuring reliable fabrication of the coupling region. The coupling length given by $L_c = \lambda_0/2(n_{aGST1} - n_{aGST2})$ is thus calculated as compact as ~24 μm, where n_{aGST1} and n_{aGST2} are respectively the effective indices of the first order (even) and second order (odd) supermodes in the two-waveguide system, λ_0 = 1550 nm is the wavelength.

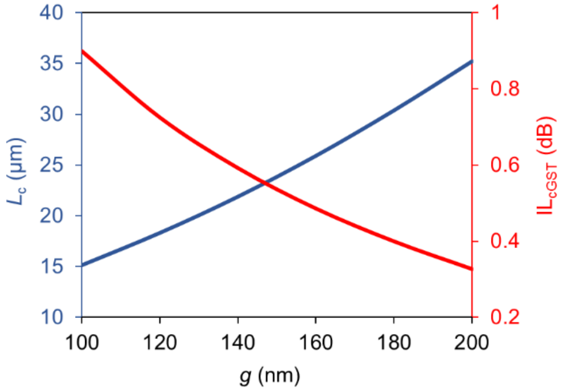

Figure 4.3. Trade-off between the coupling length for the maximum transmission in the amorphous state and insertion loss in the crystalline state by varying the gap.

Based on the above structure, we calculated transmission spectral response of the 1 × 2 DC switch in both states (Figure 4.1d,e) by the three-dimensional (3D) finite-difference time-domain method (FDTD) in a commercially available software Lumerical (FDTD Solution). When the GST is in the amorphous state, the optical switch attains a small IL < 1 dB and CT from −11 dB to −23 dB over the wavelength range of 1520-1550 nm. For the crystalline state, since almost no evanescent coupling occurs due to the phase mismatch, the spectral response to the input light is quite flat and broadband. The corresponding IL and CT are < 0.6 dB and < −29 dB across the whole wavelength range.

4.1.2 *Experiment*

The devices were fabricated using a similar method to that described in Chapter 2. The pattern was defined via EBL and transferred to the top silicon layer by ICP-RIE (fully etched). Deposition of 20 nm GST and 11 nm ITO on the HWs was completed using a second EBL step followed by the sputtering and lift-off process. Figure 4.4a,b show the optical microscope and SEM images of the fabricated 1 × 2 DC switch. A false-colored SEM image of the coupling region is shown in Figure 4.4c where the GST layer is clearly resolved.

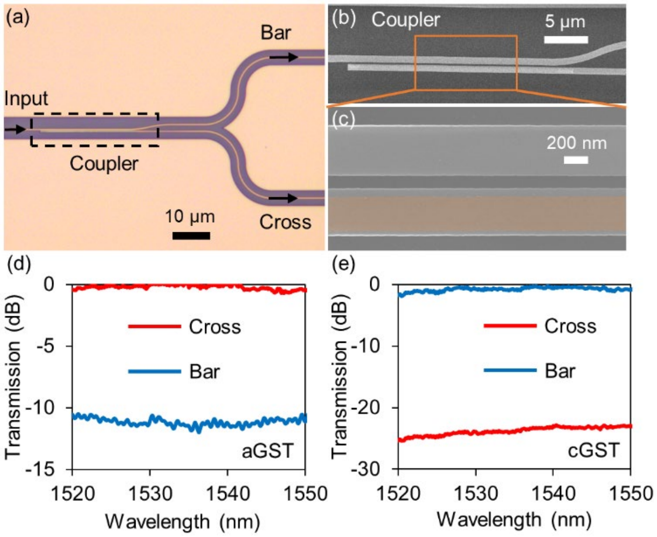

Figure 4.4. Experimental results of the 1 × 2 DC switch. (a) Optical microscope image of the fabricated switch. (b) SEM image of the switch. (c) An enlarged view of the coupling region highlighted by the orange rectangle in (b) with the GST false-colored. (d-e) Measured transmission at the cross and bar ports with the GST in the (d) amorphous and (e) crystalline states.

The same off-chip optical fiber setup was used to measure the spectral response of the fabricated devices (see Chapter 2). The straight single-mode waveguides on the same chip were utilized to normalize the spectra of the target devices. For each device, we measured the transmission right after the deposition of the GST, which is initially in the amorphous state because of the low sputtering temperature. After that, RTA (see Chapter 2) was performed to actuate the phase transition from aGST to cGST and another transmission measurement was conducted. The measurement results of the 1 × 2 DC switch are shown in Figure 4.4d,e. For the wavelength range of 1520-1550 nm, the ILs were measured to be approximately 1 dB for both states and the CT was measured to be < -10 dB for aGST and < -22 dB for cGST. The discrepancy between the measured CTs and the design targets is primarily due to the fabrication-induced gap change and positional deviation of the GST layer owing to the limited alignment precision.

4.2 2 × 2 PHOTONIC SWITCH

We extend the DC design scheme to build a 2 × 2 switch.

4.2.1 *Design and Simulation*

Figure 4.5a shows the schematic diagram of the 2 × 2 DC switch based on the three-waveguide DC. The three-waveguide DC consists of two identical silicon strip waveguides separated by a GST-on-silicon hybrid waveguide. The operating principle of the proposed switch relies on the considerable mode modification of the TE-polarized supermodes in the three-waveguide system due to the GST phase transition. When the GST is in the amorphous state, the device functions as a three-waveguide DC and the complete power transfer could be achieved when the phase-matching condition (*i.e.* the effective indices of the three supermodes are evenly spaced) [88,89] is satisfied. Thus, the input light couples to the low-loss GST-on-silicon HW and passes through the cross port (Figure 4.5b). Once the GST is crystallized, the three-waveguide system effectively boils down to two separated SWs because of the much higher effective index of the HW. In this case, only the even and odd supermodes can be supported in the coupler. The gap between the two SWs is $w_p + 2g$, resulting in a much larger coupling length (L_{cGST}). Hence, after a specific coupling length (L_c, designed for the maximum transmission in the amorphous state, *i.e.*, L_{aGST}), the input light is almost not cross-coupled but propagates directly to the bar port as if the central HW does not exist (Figure 4.5c).

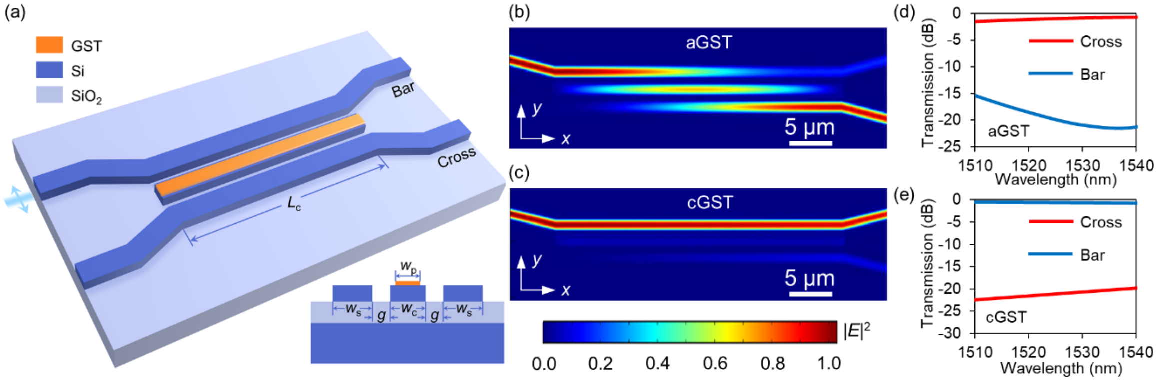

Figure 4.5. Simulation of the 2 × 2 DC switch. (a) Schematic of the switch. (b,c) Normalized optical field intensity distribution in the device for (b) aGST and (c) cGST simulated at 1550 nm. (d,e) Calculated transmission spectra at the cross and bar ports for (d) aGST and (e) cGST.

We study the light coupling mechanism by analyzing the supermodes in the coupling region (Figure 4.6). In this calculation, we adopt the same parameters used in the 1 × 2 switch with w_s = 450 nm, g = 150 nm, and $w_p = w_c - 100$ nm. Figure 4.6a-e shows the transverse electric field distribution of all the supermodes supported by the three-waveguide coupler at 1550 nm in the amorphous and crystalline state. For aGST, the three-waveguide coupler supports two symmetric modes and one antisymmetric mode, as shown in Figure 4.6a-c. For cGST, only even and odd supermodes can be supported in the coupler, as shown in Figure 4.6d,e. In this state, the device can be simply regarded as a two-core DC. The dependence of the effective indices on w_c is shown in Figure 4.6f. n_{aGST1}, n_{aGST2}, and n_{aGST3} represent the three effective indices of the supermodes in the amorphous state. To achieve the maximum power transfer efficiency to the cross port, the effective indices of the supermodes need to meet the phase-matching condition given by $n_{aGST1} + n_{aGST2} = 2n_{aGST3}$. As w_c increases, n_{aGST1} and n_{aGST2} increase and the phase-matching condition can be satisfied when choosing w_c = 422 nm. Similarly, n_{cGST1} and n_{cGST2} represent the two effective indices of the supermodes in the crystalline state. They almost remain constant when w_c changes as there exists no field distribution in the hybrid GST-on-silicon waveguide, indicating little coupling.

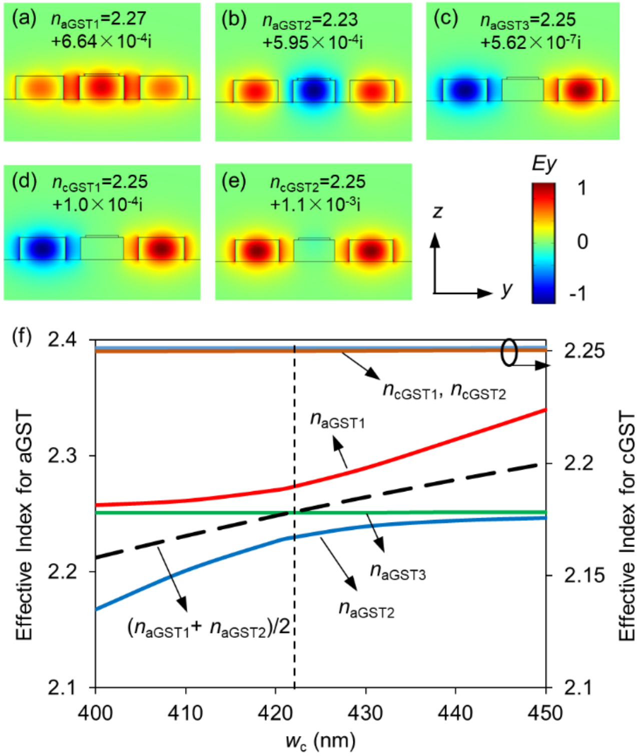

Figure 4.6. Mode analysis of the three-waveguide system. (a-e) Normalized E_y field profiles of the supermodes in a three-waveguide system when GST is in the (a-c) amorphous and (d-e) crystalline state. (f) Effective indices of five supermodes guided in the three-waveguide coupler as a function of w_c when g = 150 nm, w_s = 450 nm, $w_p = w_c - 100$ nm. The maximum coupling efficiency can be achieved when w_c = 422 nm, *i.e.*, $n_{aGST3} = (n_{aGST1} + n_{aGST2})/2$. All the modes are simulated for TE polarization at 1550 nm.

Next, the coupling characteristics are studied when varying the gap. Figure 4.7 shows the corresponding coupling length for aGST (L_{aGST}) and the ratio of the two coupling lengths for cGST and aGST (L_{cGST}/L_{aGST}). As the gap increases, L_{aGST} and L_{cGST}/L_{aGST} increase simultaneously, implying a smaller crosstalk and insertion loss due to the cross-coupling but at the cost of a larger device length. Considering this performance trade-off and fabrication feasibility, we choose g = 150 nm. The coupling length of the three-waveguide coupler for both states can be calculated by

$$L_{\mathrm{aGST}} = \frac{\lambda_0}{2(n_{\mathrm{aGST1}} - n_{\mathrm{aGST3}})} = \frac{\lambda_0}{2\Delta n_{\mathrm{aGST}}} \tag{3}$$

$$L_{\mathrm{cGST}} = \frac{\lambda_0}{2(n_{\mathrm{cGST1}} - n_{\mathrm{cGST2}})} = \frac{\lambda_0}{2\Delta n_{\mathrm{cGST}}} \tag{4}$$

When g = 150 nm, L_{aGST} and L_{cGST} are calculated to be 35 μm and 516 μm, respectively, resulting in a large ratio of $L_{\mathrm{cGST}}/L_{\mathrm{aGST}}$ = 14.7. Hence, it is expected that the switching operation of the two states can be achieved if we choose a suitable coupling length for the amorphous state.

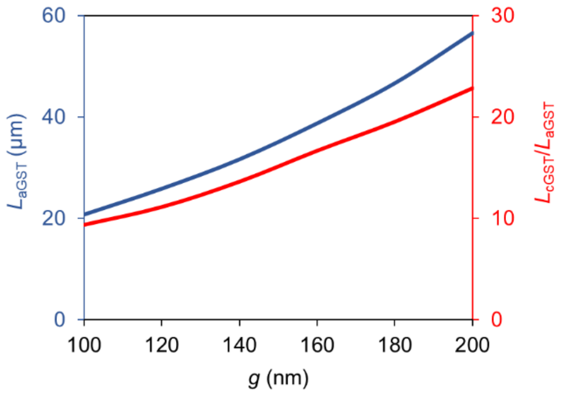

Figure 4.7. Trade-off between L_{aGST} and $L_{\mathrm{cGST}}/L_{\mathrm{aGST}}$ by varying the gap.

Based on the above structure, we calculated the spectral response of the designed 2 × 2 DC switch for aGST and cGST when launching the light from one of the input ports (Figure 4.5d,e). The simulation was performed by the 3D eigenmode expansion method (EME) in Lumerical (MODE Solution). This method is especially suitable for the 2 × 2 switch due to the invariant structure in the propagation direction of light and can significantly reduce the calculation time by reusing the scattering matrices of similar structure sections [90]. The grid size of the mesh in our simulation is set as $\Delta x = \Delta y = \Delta z = 20$ nm. To ensure the accuracy of the field distribution, a grid size of 2 nm is used to override the GST domain. The device exhibits low ILs of <1 dB in both states when the wavelength varies from 1510 nm to 1540 nm. The bandwidth for achieving a CT less than −15 dB in the amorphous state and less than −20 dB in the crystalline state is more than 25 nm, enabling broadband switching operation.

4.2.2 *Experiment*

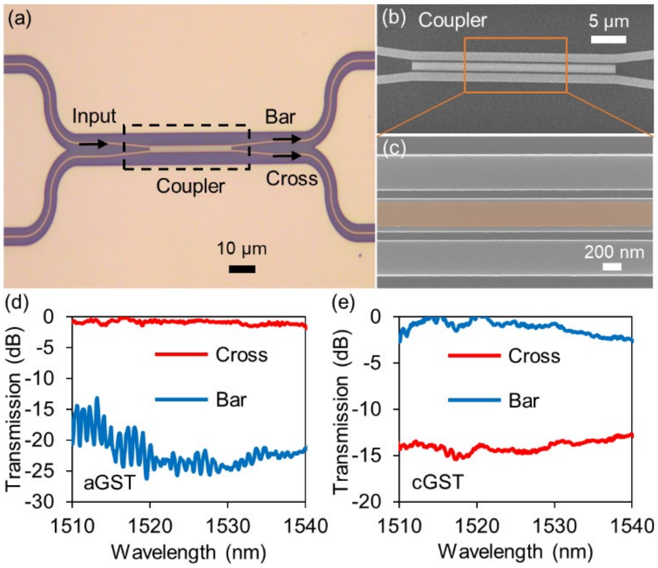

Figure 4.8. Experimental results of the 2 × 2 DC switch. (a) Optical microscope image of the fabricated switch. (b) SEM image of the switch. (c) An enlarged view of the coupling region highlighted by the orange rectangle in (b) with the GST false-colored. (d,e) Measured transmission at the cross and bar ports with the GST in the (d) amorphous and (e) crystalline states.

Figure 4.8a,b shows the microscope and SEM images of the fabricated 2 × 2 DC switch. A false-colored SEM image of the coupling region is shown in Figure 4.8c where the GST layer is clearly resolved. The measured transmission spectra of the 2 × 2 DC switch are shown in Figure 4.8d,e. For aGST, the IL was measured to be approximately 1 dB and the CT is less than ~−15 dB at the wavelength ranging from 1510 nm to 1540 nm, agreeing well with the simulation results. For cGST, the IL through the switch is approximately 1-2 dB and the CT is less than −10 dB with a bandwidth of over 30 nm. The degraded IL and CT compared with the simulation results are mainly attributed to the gap discrepancy due to the fabrication imperfection and positional deviation of the GST layer owing to the limited alignment precision.

4.3 DISCUSSION

Here, we discuss the optical bandwidth of the switches as well as the design for transverse magnetic (TM) polarization.

4.3.1 *Optical Bandwidth of the Switches*

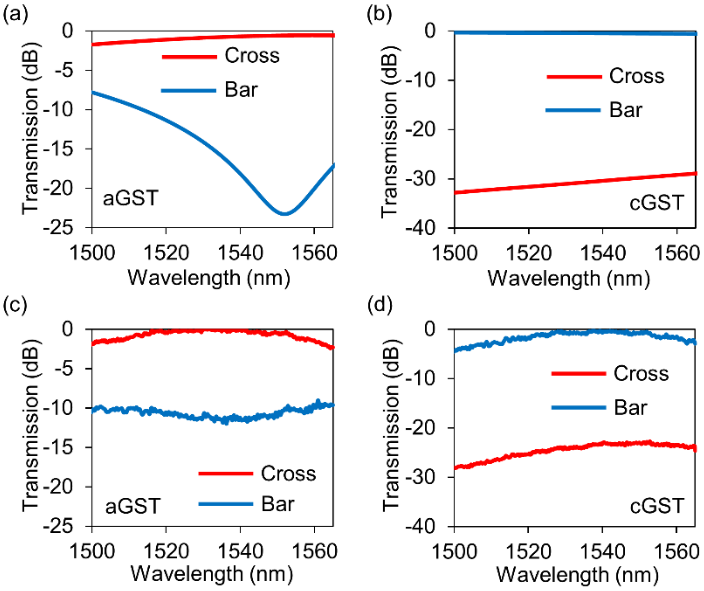

Figure 4.9. Full wavelength range transmission spectra of the 1 × 2 DC switch at the cross and bar ports for (a,b) simulations and (c,d) experiments.

Figure 4.9 and Figure 4.10 show the full-wavelength-range transmission spectra of the switches at the cross and bar ports for both simulation and experiment. The designed switches have an optical bandwidth of ~60 nm with CT < -10 dB and IL < 1 dB which is primarily limited by the wavelength-dependent coupling length and phase-matching condition due to the waveguide dispersion and can be further improved by utilizing the adiabatic [91], bent [29], or multi-section [92] DC. However, the optical bandwidth of the fabricated devices degraded to ~30 nm with CT

< −10 dB and IL ~1 dB due to the fabrication imperfection. The longest wavelength range (1565 nm) is limited by our tunable laser.

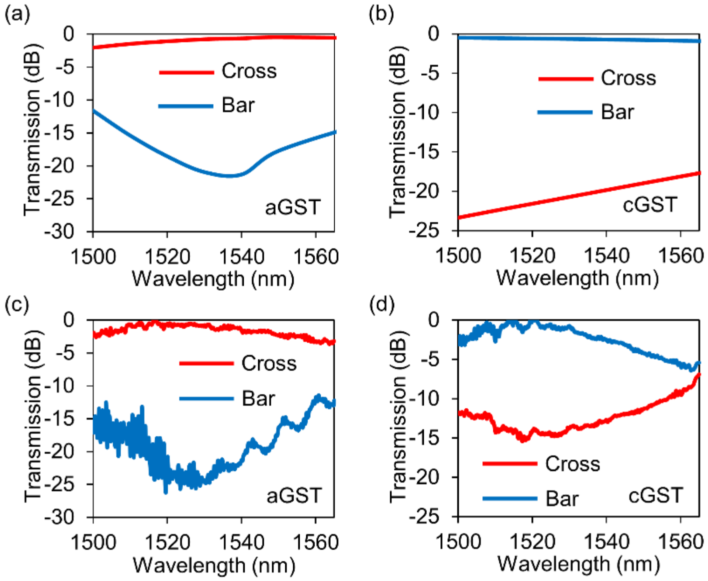

Figure 4.10. Full wavelength range transmission spectra of the 2 × 2 DC switch at the cross and bar ports for (a,b) simulations and (c,d) experiments.

4.3.2 *Design of the Switches for TM Polarization*

The design method also works for switches operating in the TM mode. As an example, we optimize a 1 × 2 switch (with the same schematic as in Figure 4.1a). Figure 4.11a shows the calculated effective indices of the fundamental TM modes of the SW and the HW with respect to their widths. The right side shows the electrical field distribution for the TM mode of the HW for aGST and cGST. The width of the silicon waveguide (w_s) is chosen as 550 nm to ensure single-mode operation. The optimal w_c is 390 nm to achieve strong coupling between the two waveguides, which can be verified in Figure 4.11b,c. Therefore, the input TM-polarized light will be evanescently coupled to the cross port completely with an appropriate coupling length (~15 μm when the gap is 400 nm). On the contrary, with the GST switched to the lossy crystalline state, the huge effective index contrast between the two waveguides indicates a serious phase mismatch, resulting in two isolated modes as shown in Figure 4.11d,e and uncoupled light directly guided into the bar port with very low insertion loss. In this way, we can conclude that our proposed 1 × 2 switch schematic can be redesigned for TM operation. Similarly, to achieve the 2 × 2 switch for TM operation, a symmetric adjacent waveguide could be added to form the 2 × 2 schematic and meet the phase-matching condition for the three-waveguide DC system. Therefore, our methods to design the DC switches for TE polarization could also be applied to TM operation.

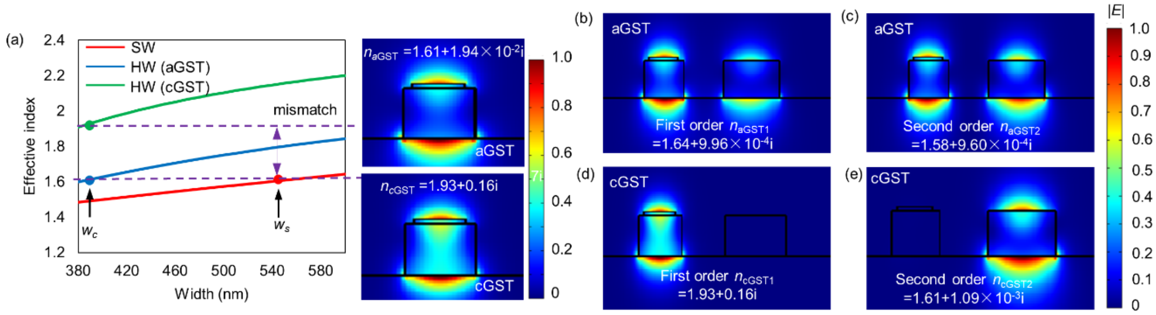

Figure 4.11. Design of the 1 × 2 DC switch for TM polarization. (a) Left: effective indices of the fundamental TM modes in the silicon SW and the HW. Right: the normalized electrical field profiles of the TM mode with GST in the amorphous and crystalline state. The widths of the SW and the HW are w_s = 550 nm and w_c = 390 nm, respectively. The width of the GST (w_p) is set to be 100 nm smaller than w_c. (b-e) Normalized electrical field profiles of the supermodes in the two-waveguide system when the GST is in (b,c) amorphous and (d,e) crystalline state. All the modes are simulated for TM polarization at 1550 nm.

4.4 SUMMARY

In this chapter, we demonstrated compact (~30 μm) nonvolatile 1 × 2 and 2 × 2 switches with low-loss (~1 dB) and broadband (over 30 nm with CT < −10 dB) operations on the GST-on-silicon platform. Although the reported switches are optimized for TE polarization, similar design can be conducted for TM operation. With emerging wide-bandgap PCMs [93,94] and better fabrication, further improvement of the performance including IL and CT can be expected. The optical bandwidth of the designed switches is primarily limited by the wavelength-dependent coupling length and phase-matching condition and can be further improved by utilizing the adiabatic, bent, or multi-section DC. As a proof of concept, thermal heating was employed to actuate the phase transition in this work. For practical applications in a large-scale PIC, on-chip electrical switching using transparent conductive heaters such as ITO [61,68,95], graphene [77], or silicon [48,57] can be considered with the switching speed as fast as ~10 MHz, which is much faster than the traditional thermo-optic switches (~100 kHz) [29,30]. From the volume of the GST needed in the switches, the reconfiguration energy for phase transition is estimated to be ~2 nJ [39], only an order of magnitude larger than the thermodynamic limit [47]. The availability of such on-chip nonvolatile switching technology paves the way for optical FPGAs and sheds light on their applications including optical interconnects, neuromorphic computing, quantum computing, and microwave photonics.

Chapter 5.

MODELING ELECTRICAL SWITCHING WITH HEATERS

To scale up the GST-on-silicon platform to a much higher complexity, it is also important to have scalable control over the states of GST. In general, reversible phase transitions of PCMs on PICs can be triggered either by self-heating or thermal-conduction heating. Self-heating relies on the photothermal or Joule heating effect of PCMs to actuate the phase change process and can be realized by free-space optical switching [39,53,64], on-chip optical switching [3,50,51,58-63,67,72-74,96], or electrical threshold switching [51,54,56,66]. Resembling the approach used in rewritable optical disks, free-space optical switching, where PCMs are heated up by focusing laser pulses onto target devices in the far field, facilitates the switching of large-area PCMs at any position, but is not viable for further integration and scaling due to the slow, diffraction-limited, inaccurate alignment process [39]. In contrast, on-chip optical switching, mainly exploiting the evanescent coupling of near-field light pulses between waveguides and above PCMs, allows fully integrated all-optical operations of small-size PCMs down to the nanoscale [51]. However, it is challenging to switch large-area PCMs through this method due to the nonuniform heating, and the complexity of PICs is restricted because of the difficulty in light routing and cascaded-device heating [3], leading to limited switching contrast and system complexity. Note that, both the photothermal-based approaches will suffer from the low extinction coefficient of amorphous state in the re-crystallization process [58,61], where multiple pulses or a single structured pulse are usually needed. The issue becomes particularly severe when transparent PCMs are used [93,94]. Electrical threshold switching by contacting the two sides of PCMs in a circuit seems to be a better choice for large-scale integration. Nevertheless, it proves to be ineffective because the limited operation volume of PCMs due to the crystallization filamentation [97] and nonuniform heating conflicts with the requirement of relatively large size for photonic devices, resulting in low optical contrast between two states [51]. This method will also face challenges when it comes to less conductive PCMs which are generally also transparent due to their larger bandgaps. In comparison, thermal-conduction heating via external electrical heaters [48,57,61,68,95], instead, can locally select and arbitrarily extend the switching region by increasing the size of the heaters. Therefore, this approach intrinsically eliminates all the above problems, enabling large-area phase-change photonic devices [48,55] with the potential of strong optical modulation and high-complexity integration. However, among the few works based on this approach [48,57,61,68,95], no fast (> 10 MHz) and energy-efficient (~10 aJ/nm^3) electrical control has been reported so far. To maximize the advantages of thermal-conduction heating in terms of both optical and heating performance, the optical waveguide and heating system of phase-change integrated nanophotonic cells (PINCs), *i.e.*, the fundamental unit of PCM-integrated photonic devices, remain to be improved and the heating process requires to be analyzed and optimized. To assist the development of the future large-scale PCM-based programmable PICs, it is also important to develop a comprehensive model that has the capability of controlling and predicting the device performance.

In this chapter, we propose and model electrical switching of nonvolatile PINCs with graphene heaters based on the GST-on-silicon platform. The optical and heating performance are first carefully analyzed and then compared with those of the PINCs with ITO and silicon PIN diode heaters. Note that this chapter is adapted with permission from Ref. [77]. Copyright 2020 American Chemical Society.

5.1 DEVICE CONFIGURATION AND MODELING

5.1.1 *Device Configuration*

As illustrated by Figure 5.1a, the proposed PINC is composed of a GST-on-silicon hybrid waveguide (where a thin film of GST with a width of w_{GST} and a thickness of h_{GST} is placed on top of the silicon rib waveguide) with a certain length (L) based on a silicon-on-insulator (SOI) wafer with a 220-nm-thick silicon layer on top of a 3-μm-thick buried oxide. The geometry is similar to those in the previous chapters. To conduct the electrical switching, the PINC is conformally covered with monolayer graphene as the external heater with palladium (Pd) contacts and a capping layer of SiO_2. Graphene, a single layer of carbon atoms arranged in a honeycomb lattice, has recently been introduced to integrated nanophotonic devices as a transparent heater [30,98,99] due to its high intrinsic in-plane thermal conductivity, ultra-low heat capacity, tunable transparency and conductivity as well as good flexibility and compatibility with CMOS processes [78,79,100-104]. Consequently, graphene is a promising candidate for external heaters in PINCs with great potential for high-speed and low-energy electrical switching. Rib waveguides are adopted here to reduce the step height for crackless transfer of graphene in practical applications. In order to evaluate the optical performance of the PINC, the input and output ports of the PINC are assumed to be connected with regular silicon waveguides, which is the case for most applications.

Differing from the self-heating approaches, electrical switching using external heaters relies on the transfer of electrical pulse-generated Joule heat from heaters to PCMs to actuate the phase transitions. For amorphization (Figure 5.1b, Reset), a single pulse with high power is applied to the contacts to increase the temperature of PCMs above the melting point (T_m) and then immediately removed to obtain rapid quenching, leaving PCMs in the disordered glass state with low refractive index (n) and extinction coefficient (κ). For crystallization (Figure 5.1b, Set), PCMs are heated just above the glass transition temperature (T_g) but below T_m by applying a pulse with relatively low power for a long time to enable nucleation of small crystallites and subsequent growth of them, resulting in high optical constants in the crystalline state.

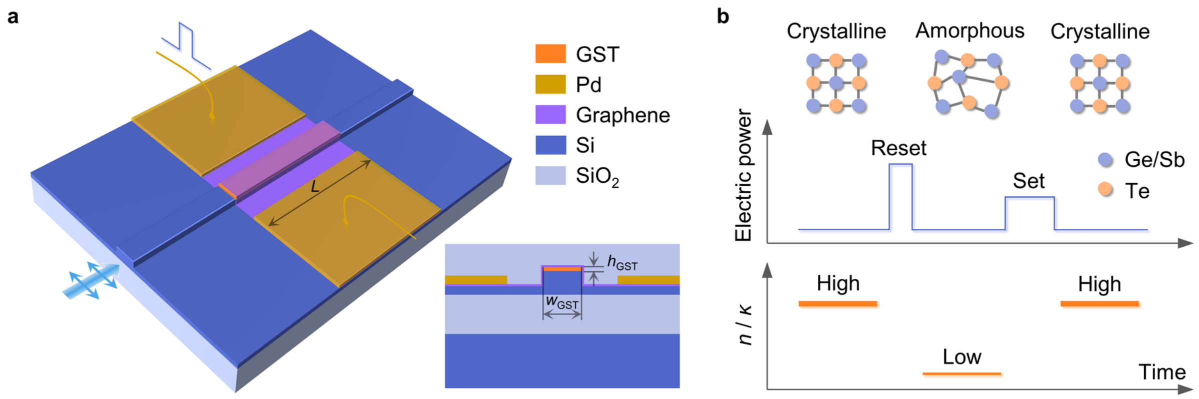

Figure 5.1. Device configuration. (a) Schematic of the proposed PINC with a graphene heater. Here, the silica cladding is hidden for clarity. The two ports of the PINC are connected with regular silicon rib waveguides in this case. Inset: cross-section of the hybrid cell. (b) Operation principle of electrical switching of the PINC with an external heater. The lattice structure, refractive index (n), and extinction coefficient (κ) of GST for amorphous and crystalline states and the electric power of the reset and set pulses are illustrated.

5.1.2 *Model Description*

The optical performance of the PINC was simulated using the same wave optics model as described in Chapter 2. The graphene was modeled as surface current density boundaries that introduce Ohmic loss due to the optical-conductivity-induced surface current [105].

To analyze the Set and Reset processes of the proposed PINC, we established a fully coupled electro-thermal 2D time-domain FEM model based on the cross-section of the PINC (Figure 5.1a, inset) using COMSOL Multiphysics. 2D simulations are more than sufficient to evaluate the heating performance given that the geometry of the PINC remains constant in the light propagation direction (assumed to be 1 μm in this work) and the boundary-effect-induced nonuniform heating in the interface between the PINC and the regular waveguides can be alleviated by fully covering the PINC with a larger heater [68]. Specifically, an electrical model (Electric Currents, Shell Interface) based on the current continuity equation was utilized to predict the current and electric potential distribution in graphene. A thermal model (Heat Transfer in Solids Interface) based on the heat transfer equation $\rho C_p \frac{\mathrm{d}T}{\mathrm{d}t} = \nabla \cdot (k_{\mathrm{th}} \nabla T) + Q_{\mathrm{e}}$ (where ρ is the material density, C_p is the specific heat at constant pressure, k_{th} is the thermal conductivity, and Q_{e} is the heat source) was used to predict the temperature distribution in the whole device. The two models are cross-coupled via Joule heating and the temperature-dependent material properties (Table 5.1).

In the electrical model, the graphene was modeled as a thin electrically conductive shell (boundary) with a thickness of 0.335 nm. The metal contacts were connected to the two sides of the graphene shell and the applied pulses were assumed to have ideal shapes. Compared with the resistance of graphene, the contact resistances between the metal contacts and graphene are negligible [30] and thus were not included in the model.

In the thermal model, the infinite element domains were adopted for the left, right, and bottom boundary regions of the model while the convective heat flux boundary condition was used on the surface with a heat transfer coefficient of 5 W/($\mathrm{m}^2 \cdot \mathrm{K}$). Considering the relative thinness of GST and graphene and high operating temperature, thermal boundary resistance (TBR) and surface-to-surface radiation boundaries were utilized. Besides, the graphene was similarly modeled as a thin thermal conduction boundary based on the thermally thin approximation with a thickness of 0.335 nm. For simplicity without losing generality, the phase transition processes were phenomenologically modeled as that the material properties of GST are weighted sums of those in the amorphous and crystalline states in a small temperature interval of $\Delta T_{\mathrm{m}} = 10$ K ($\Delta T_{\mathrm{g}} = 100$ K) centered at $T_{\mathrm{m}} = 888$ K ($T_{\mathrm{g}} = 673$ K) of GST for melting (quenching and crystallization) with latent heat of 66.81 kJ/kg (exothermic heat of 37.22 kJ/kg) involved [97,106]. Note that T_g is set to be higher than usual (~423 K) due to the increased T_g at a high heating rate [106]. The model can be further improved by incorporating accurate kinetic description of the phase transitions, including melting, vitrification, nucleation, and growth.

5.1.3 *Material Parameters*

Table 5.1 lists the main material parameters used in our simulations. Note that, TBR was applied to all the internal boundaries and depends both on the temperature and phase of GST [107-110]. The optical conductivity of graphene is calculated according to the Kubo formula at the Fermi level of −0.26 eV [111]. The refractive index and electrical conductivity of ITO are determined by Drude model with a carrier density of 3 × 10^{20} cm^{-3} [112].

Table 5.1. Main Material Parameters Used in Simulations[*]

	$\boldsymbol{n}$	$\boldsymbol{\kappa}$	$\boldsymbol{\sigma_{DC}}$ **(S m^{-1})**	$\boldsymbol{k_{th}}$ **(W m^{-1} K^{-1})**	$\boldsymbol{C_p}$ **(J kg^{-1} K^{-1})**	$\boldsymbol{\rho}$ **(kg m^{-3})**
Si	3.4777 + Δn [12]	$\Delta\kappa$ [12]	N/A	$k_{th}(T)$ [113]	$C_p(T)$ [114]	2329
SiO$_2$	1.444	0	N/A	$k_{th}(T)$ from COMSOL	$C_p(T)$ from COMSOL	2200
ITO	1.4497 [112]	0.0923 [112]	2 × 10^5 [112]	3.2 [110]	$C_p(T)$ from COMSOL	7100
Graphene	$\sigma = 6.05 \times 10^{-5} + 6.19$ 10^{-6} i [111,115]		$\sigma_{DC}(T)$ (R_s = 800 W/□ at 293 K) [116]	$k_{th}(T)$ (160 at 293 K) [79,117]	$C_p(T)$ [79]	2271
Pd	3.1640	8.2121	N/A	71.8	244	12023
aGST	3.8884 [39]	0.024694 [39]	N/A	0.19 [118]	213 [119]	5870 [120]
cGST	6.6308 [39]	1.0888 [39]	N/A	$k_{th}(T)$ [118]	199 [119]	6270 [120]

[*] σ, optical conductivity. All the optical parameters are for 1,550 nm. σ_{DC}, electrical conductivity. R_s, sheet resistance. T, temperature. Δn and $\Delta\kappa$ are dependent on carrier densities of electrons and holes and can be calculated from Eq. (6.3) and Eq. (6.4) in Ref. [12].

5.2 OPTICAL PERFORMANCE

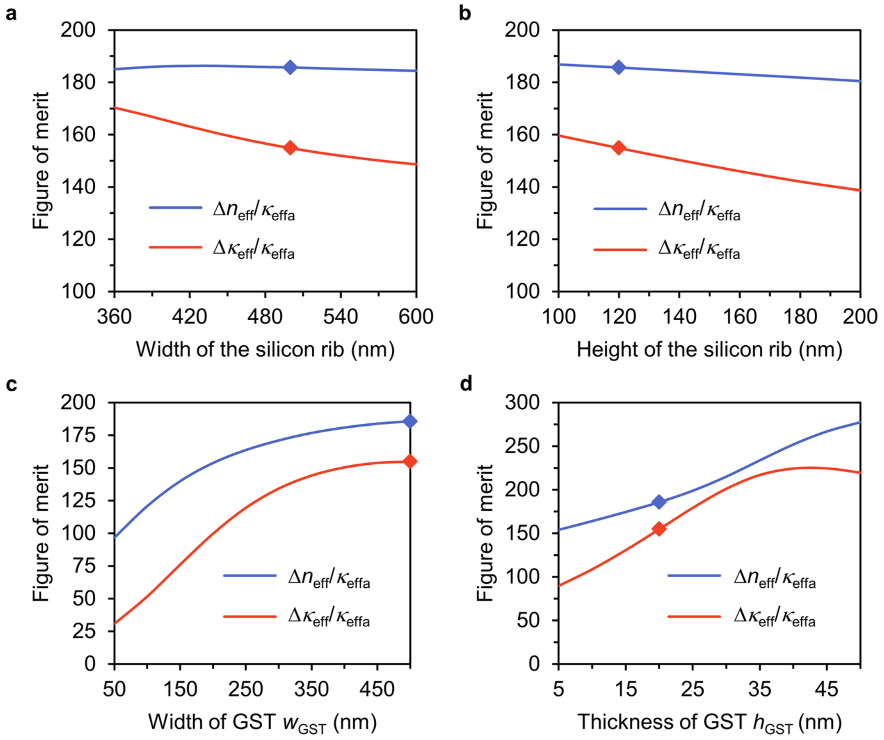

Figure 5.2. Dependence of optical figure of merits on the (a) width and (b) height of the silicon rib waveguide and the (c) width and (d) thickness of the GST film at 1550 nm. By default, the width and thickness of the GST are 500 nm and 20 nm, respectively, while the width and height of the silicon rib are fixed to be 500 nm and 120 nm, respectively. This default waveguide geometry is marked as the dots in the figures and adopted for the following analysis unless specifically pointed out. Neither heaters nor metal contacts are involved at this stage.

For large-scale programmable photonic applications, strong optical modulation and low insertion loss are essential for the optimal optical performance of the PINCs. Here, we define an optical figure of merit $FOM_1 = \Delta n_{\mathrm{eff}}/\kappa_{\mathrm{effa}}$, where Δn_{eff} denotes the effective refractive index (n_{eff}) change between the PINC with cGST aGST that determines the modulation strength and κ_{effa} is the effective extinction coefficient (κ_{eff}) of the PINC with aGST that reflects the insertion loss of the device as generally the loss for cGST is much larger than that for aGST. Both of the parameters are of great importance for optical phase modulation and the previously discussed phase-change coupling modulation (Chapter 4). One can also define the optical figure of merit as $\Delta\kappa_{\mathrm{eff}}/\kappa_{\mathrm{effa}}$ for attenuation modulation (with $\Delta\kappa_{\mathrm{eff}}$ being the effective extinction coefficient change). However, here we will primarily focus on FOM_1 since both of the figure of merits have similar behavior (Figure 5.2). As the optical performance of the GST-on-silicon waveguides are quite broadband near 1550 nm for at least 40 nm [39], the following analysis is conducted at the single wavelength of λ = 1550 nm.

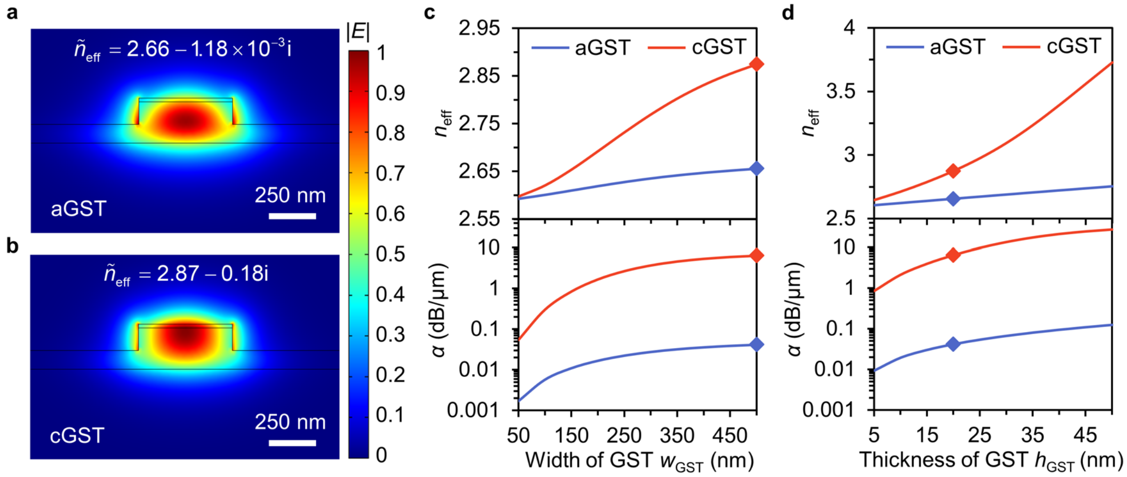

Figure 5.3. Dependence of optical performance on the waveguide geometry. (a,b) Normalized electrical field profile and complex effective index ($\tilde{n}_{\mathrm{eff}}$) of the fundamental quasi-transversal electric (TE) mode of the GST-on-silicon hybrid waveguide with (a) aGST and (b) cGST at a wavelength (λ) of 1550 nm. The width and thickness of the GST are 500 nm and 20 nm, respectively. (c,d) Effective refractive index (n_{eff}) and attenuation coefficient ($\alpha = 4\pi\kappa_{\mathrm{eff}}/\lambda$, λ = 1550 nm) of the hybrid waveguide as a function of the (c) width and (d) thickness of the GST with h_{GST} = 20 nm in (c) and w_{GST} = 500 nm in (d). The marked dots correspond to the structure in (a) and (b) and denote the adopted waveguide geometry for the following analysis unless specifically pointed out. Here, the width and height of the silicon rib are fixed to be 500 nm and 120 nm, respectively. Neither heaters nor metal contacts are involved at this stage.

Improvement of FOM_1 can be achieved by optimizing the geometry of the GST-on-silicon hybrid waveguide. As FOM_1 does not strongly depend on the dimensions of the silicon rib (Figure 5.2a,b), only the influence of the size of the GST film is discussed here while the width and height of the silicon rib are fixed to be 500 nm and 120 nm, respectively. According to the mode analysis, strong modification of the mode profile and the complex effective index ($\tilde{n}_{\mathrm{eff}} = n_{\mathrm{eff}} - \kappa_{\mathrm{eff}}\,\mathrm{i}$) can be observed once the GST is electrically switched between the amorphous (Figure 5.3a) and crystalline (Figure 5.3b) states, indicating substantial refractive and absorptive modulation effects. Figure 5.3c,d summarize the variation of the effective refractive index and attenuation coefficient ($\alpha = 4\pi\kappa_{\mathrm{eff}}/\lambda$) of the hybrid waveguide with respect to the GST geometry for aGST and cGST. As expected, both the parameters and FOM_1 (Figure 5.2c,d) increase with the increase of the GST width and thickness. Therefore, in the following analysis, we select the width of the GST film to be as large as 500 nm (same as the width of the silicon rib). However, the thickness of the GST film is set to be 20 nm by default unless otherwise specified considering the trade-off between FOM_1 and the difficulty in switching (to be discussed later) as well as the signal-to-noise ratio in real experiments.

The optical performance can also be enhanced by reducing the additional loss from the metal contacts and heaters. Although placing the electrodes far away from the rib can theoretically avoid high insertion loss (Figure 5.4), it will compromise the energy efficiency since part of the generated heat will be dissipated around the long slab region. In this case, we choose the distance between the electrodes and the rib to be as close as 500 nm (the thickness of the metal is set to be 50 nm) while maintaining moderate additional loss of ~0.01 dB/µm. The wet-transferred graphene grown by chemical vapor deposition usually has a Fermi level of around −0.28 eV ~ −0.23 eV [105,121]. Here, we assume the Fermi level of graphene to be −0.26 eV that leads to additional loss of ~0.1 dB/µm (Table 5.1). To suppress the loss from graphene, one can electrically tune the Fermi level of graphene to the Pauli blocking region where interband transitions of electrons are prohibited (*i.e.* $E_F < -0.4$ eV for the wavelength of 1550 nm) through a gate electrode [101-104]. This can potentially reduce the loss of graphene to ~0.002 dB/μm while the increased energy consumption is significantly less than the switching energy (to be discussed later) and thus is negligible. As a result, our proposed PINC exhibits a FOM_1 of ~50 (~140 with gated graphene) and propagation loss per unit length of ~0.15 dB/μm (~0.05 dB/μm with gated graphene) with an attenuation modulation of ~6.46 dB/μm and an optical phase modulation of ~0.28 π/μm at 1550 nm. The loss due to the mode mismatch between the regular silicon waveguide and the hybrid waveguide is ~0.03 dB on each side.

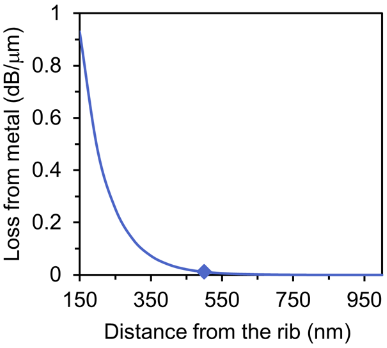

Figure 5.4. Additional loss introduced from metal contacts as a function of the distance between the edges of the electrodes and the rib waveguide. The marked dot corresponds to the adopted distance in the main text.

5.3 HEATING PERFORMANCE

5.3.1 *Temperature Distribution*

In order to operate the electrical switching with high heating performance in terms of high switching speed and energy efficiency, the real-time temperature (T) distribution of the PINC in response to an electrical pulse was calculated and analyzed based on the electro-thermal model. To successfully actuate the phase transitions without damaging the device, the raised temperature during the heating must be subjected to several constraints (the cooling rate during the quenching is also required to be about 10^{10}-10^{11} K/s [97] that is generally satisfied in our simulations). For crystallization, the temperature within the GST should be greater than $T_g + \Delta T_g/2$ to ensure adequate nucleation and growth but less than $T_m - \Delta T_m/2$ to prevent re-amorphization. For amorphization, the temperature of the GST has to be elevated above $T_m + \Delta T_m/2$ but not so high to induce ablation. Besides, the temperature within the electrodes, heater, silicon waveguide, and silica cladding should always be kept below their melting points. In other words, the temperature gradient within the GST and the heat accumulating in other regions limit the implementation of the phase transitions.

Figure 5.5a presents a typical temperature profile (without phase transitions) of the PINC with aGST at the end of a pulse with electrical power (P_0) of 5 mW and a pulse width (Δt) of 50 ns. In particular, the data cut along the x axis (Figure 5.5b) and y axis (Figure 5.5c) reveal that due to the flatness of the graphene, the GST is almost uniformly heated in the horizontal direction except the edges. However, the temperature of the GST in the vertical direction exhibits a large gradient with a much higher value close to the heater. Therefore, the temperature gradient within the GST (ΔT) can be represented by the absolute temperature difference between the top (T_{top}) and bottom (T_{bottom}) surface of the GST film along the y axis (*i.e.* $\Delta T = |T_{top} - T_{bottom}|$).

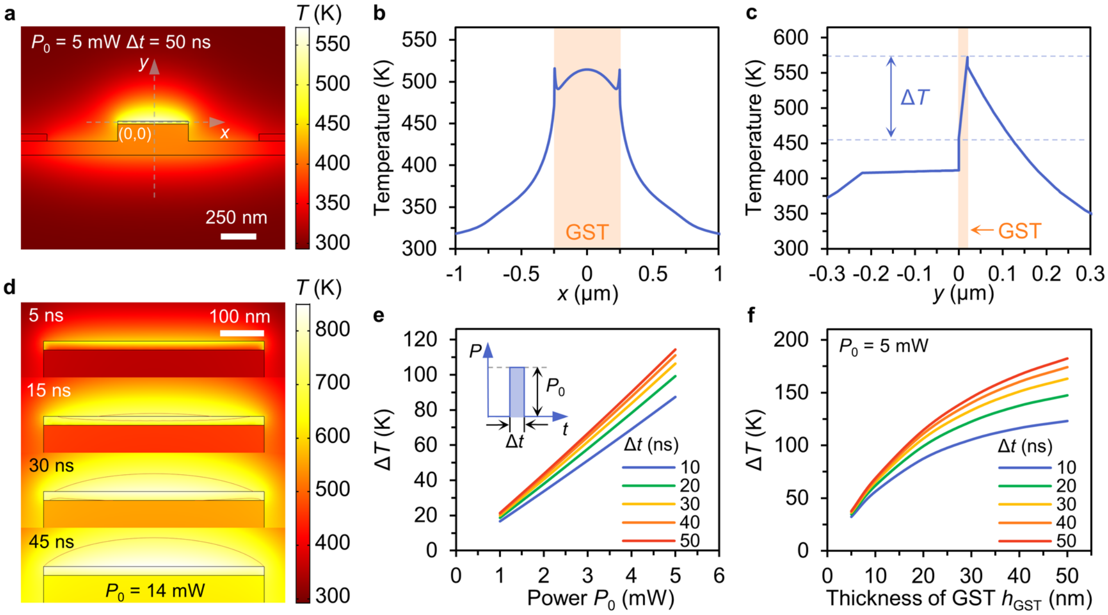

Figure 5.5. Temperature distribution analysis. (a) Temperature (T) profile of the PINC for aGST at the end of a pulse (P_0 = 5 mW, Δt = 50 ns). No phase transition is induced due to this pulse. The dashed lines denote the coordinate system with the x (y) axis parallel (perpendicular) to the surface of the GST film and the origin located at the center of the GST cross-section. (b) Temperature profile along the x axis in (a). (c) Temperature profile along the y axis in (a). The orange shaded areas in (b) and (c) represent the position of the GST film. (d) Temperature distribution at different times for a crystallization (Set) process (P_0 = 14 mW). The red lines denote the contour of T = 723 K, within which the GST is assumed to be crystallized. (e) Temperature gradient (ΔT, also marked in (c)) at the end of a pulse as a function of pulse power for different pulse widths. Inset: illustration of the applied pulse. (f) Temperature gradient at the end of a pulse as a function of GST thickness for different pulse widths (P_0 = 5 mW). The pulse energy is selected to be sufficiently low to avoid causing any phase transition of aGST in (e) and (f).

With a moderate temperature gradient (Figure 5.6, ΔT remains ~100 K during the phase transition), the crystallization process (Figure 5.5d, P_0 = 14 mW) can proceed without re-amorphization. However, a very high-power pulse or a thick GST film will result in serious re-amorphization (Figure 5.7) due to the large temperature gradient within the GST. Further analysis (Figure 5.5e,f) confirms that the temperature gradient at the end of a heating pulse (without phase transitions) rises dramatically with the increase of the pulse power and the thickness of the GST film but increases less sensitively with the pulse width. Since small ΔT is desirable for a practical Set (Reset) process without any re-amorphization (ablation) and melting of other materials, a thin film of GST and a pulse with moderate power are preferred. In the following analysis, we will investigate the influence of pulse power, pulse width, and the thickness of the GST film on the switching speed and energy efficiency.

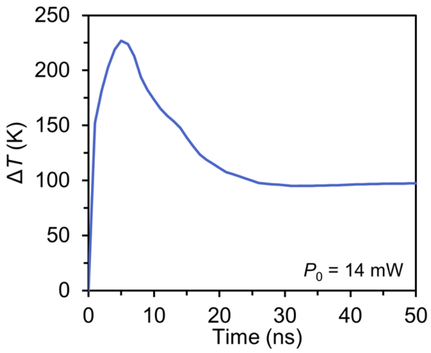

Figure 5.6. Real-time temperature gradient during the crystallization process (P_0 = 14 mW, Δt = 50 ns).

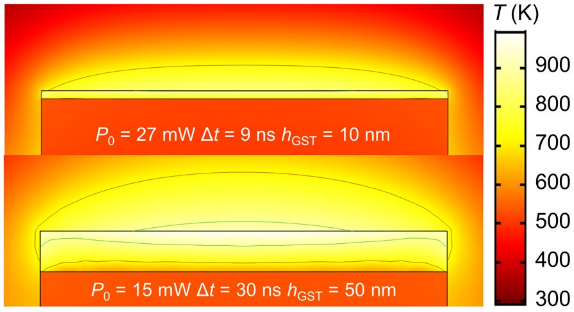

Figure 5.7. Temperature distribution at the end of a pulse indicating re-amorphization during the crystallization process due to much too high power (upper panel, P_0 = 27 mW, Δt = 9 ns, h_{GST} = 10 nm) and large GST thickness (lower panel, P_0 = 15 mW, Δt = 30 ns, h_{GST} = 50 nm). The red (green) lines denote the contour of T = 723 K (T = 883 K) for the crystallization (re-amorphization) boundary.

5.3.2 *Transient Response and Switching Speed*

The switching speed of the PINC is limited by the pulse width and the dead time (τ, 1/e cooling time) due to the thermal relaxation. As the Set process usually requires a relatively longer pulse and thus determines the ultimate speed, we mainly discuss the thermal relaxation of cGST and the crystallization period (t_{ac}, defined as the summation of the required pulse width Δt_{ac} and corresponding dead time τ_{ac} for crystallization).

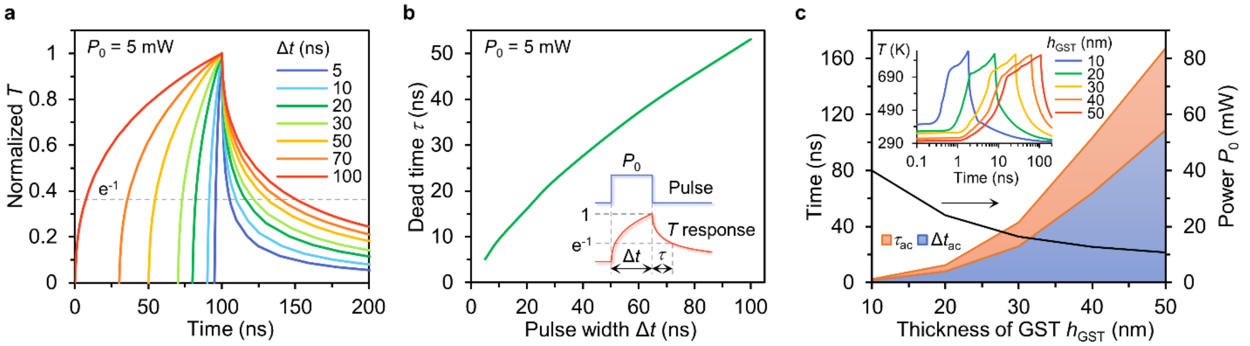

Figure 5.8. Transient response and speed analysis. (a) Normalized temperature response in the center of the GST cross-section to the pulses with different pulse widths. The power of the pulse is chosen to be as low as 5 mW in order to heat the cGST without inducing any phase transition. The dashed line denotes the position where the temperature is 1/e of the maximum. (b) Extracted dead time (τ, 1/e cooling time) from (a) as a function of pulse width. Inset: illustration of the applied pulse and temperature response. (c) Area chart of the minimum pulse width (Δt_{ac}) and corresponding dead time (τ_{ac}) required to achieve complete crystallization actuated by the maximum allowed pulse power (black line) as a function of GST thickness. Inset: transient temperature response of the crystallization process for different thicknesses of GST.

As presented in Figure 5.8a,b, the transient temperature response due to the heating and cooling of the cGST (without phase transitions) shows considerably higher cooling rates for shorter pulses. This could be intuitively understood that for longer pulses, more energy will get lost into the waveguide and substrate due to the thermal diffusion [58,60], so that a larger heat capacity and a longer thermal time constant are expected leading to a longer dead time (and a lower energy efficiency as will be discussed later). In contrast, the dead time depends little on the pulse power (Figure 5.9a) and the thickness of the GST film (Figure 5.10a,b).

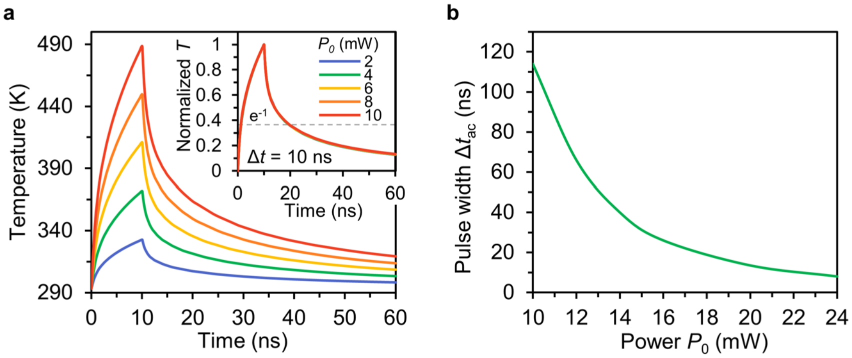

Figure 5.9. Power-dependent transient response. (a) Temperature response in the center of the GST cross-section to the pulses with different pulse power. Inset: corresponding normalized temperature response. The dashed line denotes the position where the temperature is 1/e of the maximum. The power of the pulse is chosen to be low enough in order to heat the cGST without inducing any phase transition and the pulse width is 10 ns. (b) Minimum pulse width required to achieve complete crystallization as a function of pulse power.

This is, however, not the case for the crystallization. The minimum pulse width (Δt_{ac}) required to achieve complete crystallization rapidly decreases with the increase of the pulse power (Figure 5.9b, with a fixed GST thickness) and linearly drops with the decrease of the GST thickness (Figure 5.10c, under fixed pulse power). As a result, the dead time (τ_{ac}) decreases a lot accordingly (because the pulse width is shorter). This is especially conspicuous if we consider the optimal (fastest) case (Figure 5.8c) that the maximum pulse power allowed to actuate crystallization without re-amorphization (limited by the temperature gradient as discussed earlier) is applied. The crystallization period substantially reduces with the increased power for the thinner GST film. Therefore, to obtain high-speed operations, a thin film of GST and a short pulse (enabled by using a high-power pulse) are needed. For the PINC with 20-nm-thick GST, the switching speed can be as fast as ~80 MHz (with $\Delta t_{\mathrm{ac}} = 8$ ns, $\tau_{\mathrm{ac}} = 4.47$ ns) that is one or more orders of magnitude larger than previous results [48,57,61,68,95]. The speed is also two or more orders of magnitude larger than that of the traditional volatile, weak thermo-optic effect-based optical switches/modulators [30,98,99] which is limited due to the requirement of the steady state and the tuning of large-volume materials achieved by a much longer pulse with a much slower cooling rate. It is worth noting that for partial crystallization, Δt_{ac} can be even less than 1 ns for 10-nm-thick GST (Inset of Figure 5.8c), inferring that gigahertz operations are possible.

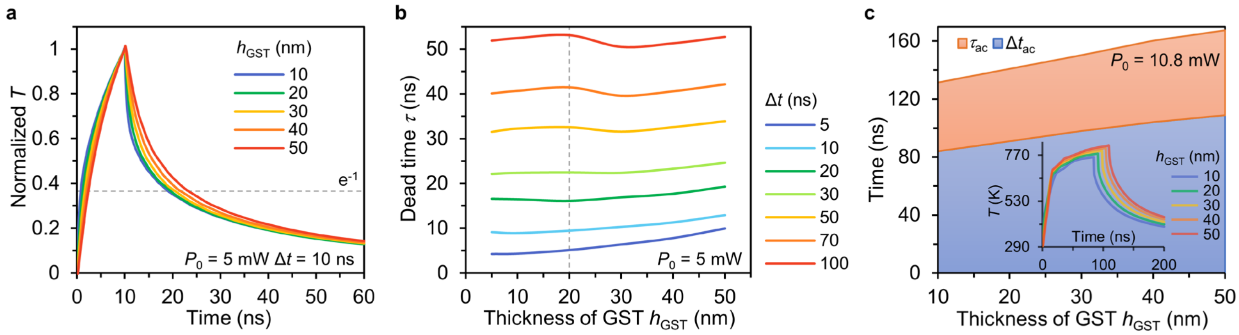

Figure 5.10. GST thickness-dependent transient response. (a) Normalized temperature response in the center of the GST cross-section for different GST thicknesses. The power of the pulse is chosen to be as low as 5 mW in order to heat the cGST without inducing any phase transition and the pulse width is 10 ns. The dashed line denotes the position where the temperature is 1/e of the maximum. (b) Extracted dead time as a function of GST thickness for different pulse widths. The dashed line denotes the adopted thickness in the main text. (c) Area chart of the minimum pulse width and corresponding dead time required to achieve complete crystallization actuated by a fixed pulse power (P_0 = 10.8 mW) as a function of GST thickness. Inset: transient temperature response of the crystallization process for different thicknesses of GST.

5.3.3 *Energy Efficiency*

In order to achieve high energy efficiency, similar rules of thumb can be followed. Here, the energy efficiency (η) is defined as the ratio of the absorbed heat energy in GST (E_{GST}) at the end of a pulse and the applied electrical pulse energy (E_{pulse}) and can be given by

$$\eta = \frac{E_{\mathrm{GST}}}{E_{\mathrm{pulse}}} = \frac{\int \rho C_p \left(T - T_0\right) \mathrm{d}V}{P_0 \Delta t} \tag{5}$$

where T_0 is the initial ambient temperature (293 K) and the integral domain is over the entire GST film. As the Set process usually consumes more energy, we primarily discuss the energy efficiency of heating the aGST and crystallization.

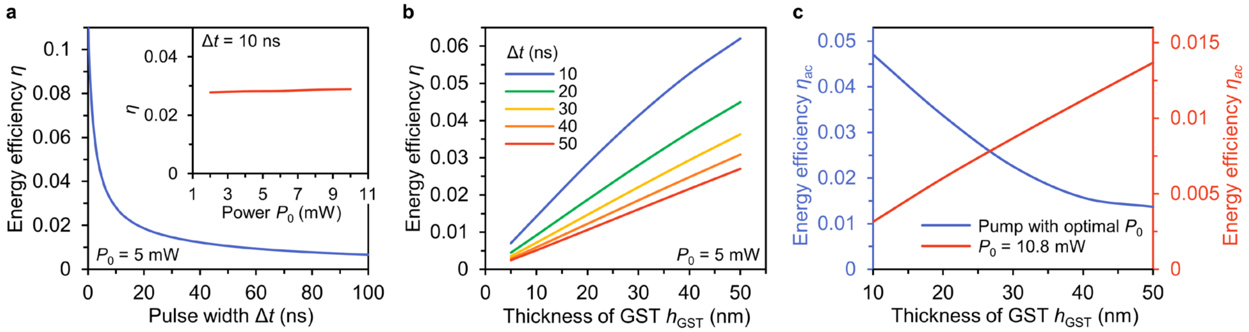

Figure 5.11. Energy efficiency analysis. (a) Energy efficiency (η) as a function of pulse width. Inset: pulse-power insensitive energy efficiency (Δt = 10 ns). (b) Energy efficiency as a function of GST thickness for different pulse widths. The pulse power is selected as low as 5 mW for (a) and (b) in order to heat the aGST without inducing any phase transition. (c) GST-thickness dependent energy efficiency for crystallization (η_{ac}) actuated by a pulse with optimal power (blue line) and fixed power (red line).

Similar to the dead time, the energy efficiency of heating (without phase transitions) significantly diminishes with the increase of the pulse width (Figure 5.11a) but is insensitive to the change of the pulse power (Inset of Figure 5.11a and Figure 5.12). However, the energy efficiency is improved with the increase of the GST film (Figure 5.11b). This may mislead one to choose a thick GST film for low energy consumption. Indeed, if the crystallization is involved, a thin film GST requires a much shorter pulse to optimally actuate the phase transitions (using the maximum allowed power, Figure 5.8c) that ultimately results in higher energy efficiency for crystallization (η_{ac}, blue line in Figure 5.11c). In comparison, if a pump pulse with a fixed power is utilized, since the required pulse width does not increase much (Figure 5.10c), η_{ac} will still rise with the increase of the GST thickness (red line in Figure 5.11c). Consequently, a thin film of GST and a short pulse optimized by high power are critical to enable high energy efficiency. In other words, a fast PINC is also an energy-efficient device. For the PINC with 20-nm-thick GST, the consumed energy for crystallization can be optimized to be as low as ~0.192 nJ (19.2 aJ/nm^3) with energy efficiency of ~3.5% that is at least one order of magnitude more efficient than previous results [48,57,61,68]. Based on a similar trend, the consumed energy for amorphization can be as low as 0.066 nJ (6.6 aJ/nm^3) that is almost two or more orders of magnitude more efficient than previous results [48,57,61,68]. Note that the energy efficiency can be further improved if partial crystallization or amorphization is needed which is essential for multi-level operations. In this case, the pulse width can be much shorter (< 1 ns as discussed earlier) so that it is possible to reduce the energy consumption to near the fundamental limit (1.2 aJ/nm^3) [47].

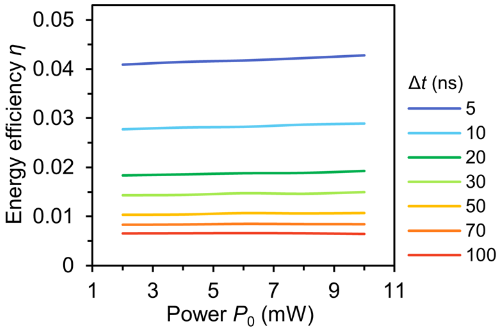

Figure 5.12. Power-dependent energy efficiency for different pulse widths. The pulse power is selected to be low enough in order to heat the aGST without inducing any phase transition.

5.4 COMPARISON WITH ITO AND PIN DIODE HEATERS

From the above analysis, the proposed PINCs with graphene heaters exhibit excellent optical and heating performance. However, there exist two other candidates for transparent heaters. First, ITO is a common transparent conductor that has been widely used in optoelectronics and display technology. Moreover, silicon itself could act as a transparent heater as long as the cores of the waveguides are not heavily doped. In this case, to achieve enough conductivity while maintaining low loss, a PIN junction could be adopted [48]. This type of heaters is only valid for silicon photonic platform in contrast to those nonvolatile silicon nitride photonic devices. Here, we compare the performance of PINCs with ITO, PIN diode, and graphene heaters through similar electro-thermal models.

5.4.1 *Device Configuration and Modeling*

As illustrated in Figure 5.13, all three types of PINCs have the same rib waveguides and electrodes, but for the PINCs with ITO heaters, the rib waveguides are conformally covered with 20-nm-thick ITO while for the PINCs with PIN diode heaters, the slabs are heavily doped by boron and phosphorus ion implantation (10^{20} cm^{-3}), 100 nm away from the left and right edge of the rib, respectively.

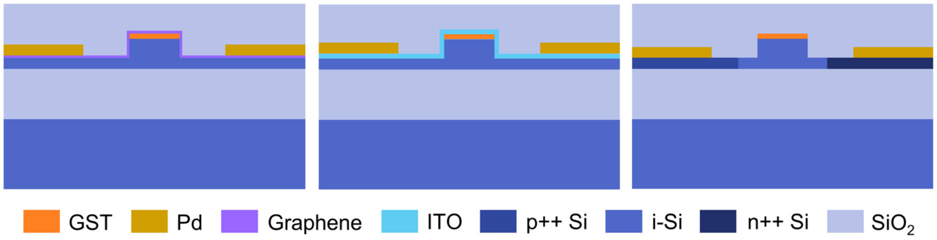

Figure 5.13. Cross-section schematics of the PINCs with graphene, ITO, and PIN diode heaters. p++ (n++), heavily doped p (n)-type silicon region. i, intrinsic silicon region.

Based on an identical model, the PINCs with ITO heaters were simulated except that instead of being treated as a thin film boundary, the ITO here was normally modeled as a 2D domain. For the PINCs with PIN diode heaters, a semiconductor model (Semiconductor Interface) based on the Poisson's equation, current continuity equation, and drift-diffusion current density equations [122] was exploited to estimate the electric potential, current density, and carrier density distributions in the PIN junctions while the thermal model was identical to that for the PINCs with graphene heaters. In particular, the Fermi-Dirac carrier statistics and Jain-Roulston bandgap narrowing model were utilized due to the high doping level. The Arora mobility model was added to simulate the effect of phonon/lattice and impurity scattering while the Fletcher mobility model was used to describe the carrier-carrier scattering at high voltage. Trap-assisted recombination and Auger recombination for high bias were also considered in the model. The metal contacts were assumed to be ideal Ohmic and the applied pulses had ideal shapes. All the other external boundaries were electrically insulated. Figure 5.14 shows the current-voltage (I-V) curve of the silicon PIN diode. The carrier density distribution at semiconductor equilibrium was also employed to determine the complex refractive index of the doped silicon (Table 5.1) for mode analysis.

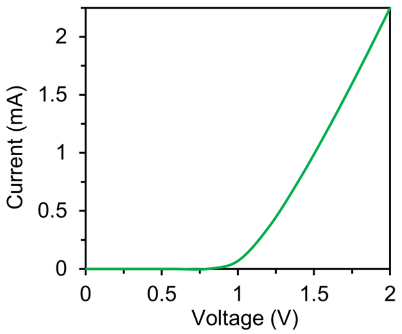

Figure 5.14. Current-voltage (I-V) curve of the silicon PIN diode.

5.4.2 *Performance Comparison*

Due to the very different structures and material properties (Table 5.1), the PINCs with these heaters display extremely distinct transient temperature response and temperature distributions for optimal crystallization (Figure 5.15) and amorphization (Figure 5.16) processes. As a result, their heating performance including the switching speed and energy efficiency is also very different. For instance, the PINCs with graphene heaters show the highest switching speed thanks to the ultra-low heat capacity and high in-plane thermal conductivity of graphene, the PINCs with ITO heaters exhibit very large temperature gradient near the GST due to the low thermal conductivity of ITO, and the PINCs with PIN diode heaters have severe thermal diffusion because of the high thermal conductivity of silicon. Note that despite directly contacting with silicon, graphene and ITO heaters limit the thermal dissipation to silicon due to the existence of the TBR on the material interfaces as thermal barriers [109].

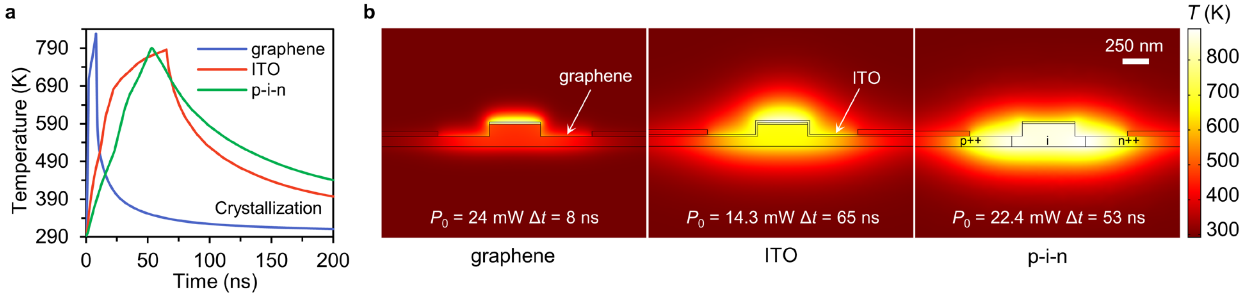

Figure 5.15. Comparison of temperature response of the PINCs with different heaters for crystallization. (a) Transient temperature response of the PINCs with different heaters for crystallization. (b) Temperature distribution at the end of a pulse during the crystallization process in (a) for the PINCs with graphene, ITO, and PIN diode heaters. The power and width of the Set pulse for three heaters are listed in the corresponding figures. p++ (n++), heavily doped p (n)-type silicon region. i, intrinsic silicon region.

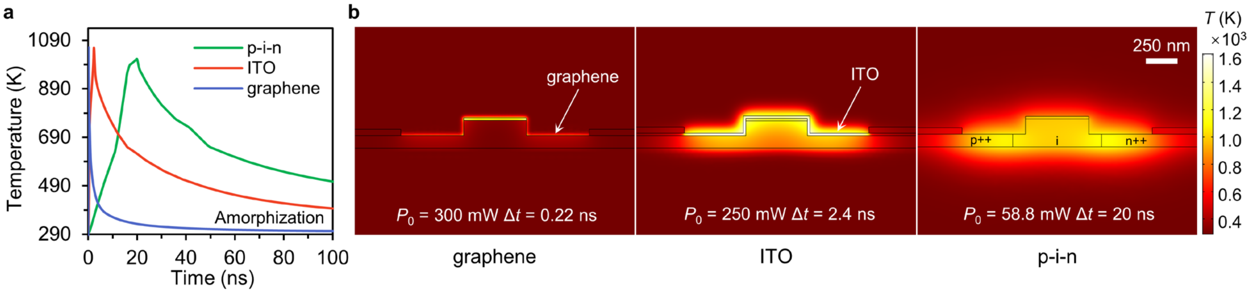

Figure 5.16. Comparison of temperature response of the PINCs with different heaters for amorphization. (a) Transient temperature response of the PINCs with different heaters for amorphization. (b) Temperature distribution at the end of a pulse during the amorphization process in (a) for the PINCs with graphene, ITO, and PIN diode heaters. The power and width of the Set pulse for three heaters are listed in the corresponding figures. p++ (n++), heavily doped p (n)-type silicon region. i, intrinsic silicon region.

To quantitively evaluate their heating performance, we define a heating figure of merit $FOM_2 = 1/E_{\text{tot}}/t_{\text{ac}}$, where E_{tot} indicates the total energy consumption for one cycle of switching that is the summation of the optimal electrical pulse energy for crystallization (E_{ac}) and amorphization (E_{ca}) and t_{ac} denotes the crystallization period that determines the switching speed. The overall figure of merit (*FOM*) for the PINCs can thus be described as the product of the optical and heating figure of merits (*i.e.* $FOM = FOM_1 \times FOM_2$).

Table 5.2. Performance Comparison of the PINCs with Different Heaters*

Heater	Δn_{eff}	κ_{effa}	Crystallization				Amorphization				FOM_1	FOM_2 ($\text{nJ}^{-1}\cdot\text{ns}^{-1}$)	FOM ($\text{nJ}^{-1}\cdot\text{ns}^{-1}$)
			Δt_{ac} (ns)	τ_{ac} (ns)	P_0 (mW)	E_{ac} (nJ)	Δt_{ca} (ns)	τ_{ca} (ns)	P_0 (mW)	E_{ca} (nJ)			
graphene	0.22	4.38×10^{-3}	8	4.47	24	0.192	0.22	1.09	300	0.066	50 or 140 (gated)	0.31	16 or 43 (gated)
ITO	0.22	4.74×10^{-3}	65	58.84	14.3	0.93	2.4	24.66	250	0.6	46	0.0053	0.24
PIN	0.21	1.82×10^{-3}	53	108.19	22.4	1.187	20	56.02	58.8	1.176	117	0.0026	0.31

*Δt_{ac} (Δt_{ca}), pulse width for crystallization (amorphization). τ_{ac} (τ_{ca}), dead time for crystallization (amorphization). E_{ac} (E_{ca}), optimal pulse energy for crystallization (amorphization).

Table 5.2 lists the essential performance and figure of merits for the PINCs with three types of heaters. According to Table 5.2, without tuning the Fermi level, the PINCs with graphene heaters can provide the best heating performance and overall performance with FOM_2 and *FOM* two orders of magnitude higher. Whereas the PINCs with PIN diode heaters have the best optical performance due to the low loss, they have the worst heating performance due to the severe heat dissipation. The overall performance for the PINCs with ITO and PIN diode heaters is close, but for ITO heaters, planarization is needed for practical applications and the large temperature gradient near the GST is concerning. In contrast, for PIN diode heaters the fabrication is relatively simple and CMOS-compatible, and the temperature gradient is small due to the high thermal conductivity of silicon. In fact, such PIN diode heaters are already part of the silicon photonics foundry processes and thus can be readily adopted for integrated phase-change photonics. Consequently, we will utilize PIN diode heaters in the experimental demonstration of electrical switching as will be discussed in the next chapter.

The optical performance and the conductivity of the heaters for all the PINCs strongly rely on the carrier density of the heater materials. By electrical tuning the Fermi level to the Pauli blocking region, the additional loss from graphene is significantly suppressed so the PINCs with graphene will have the best optical performance. In the meanwhile, the conductivity of graphene is desirably increased, meaning that a lower operation voltage is needed (the present voltage for Reset is ~20 V). For the PINCs with ITO and PIN diode heaters, since the increase of the carrier density will increase the extra loss, there exists a tradeoff to keep a moderate conductivity while maintaining low optical loss. Note that the high power listed in Table 5.2 is just used for the optimal heating performance. In practical applications, tens of milliwatts are enough to actuate the phase transitions.

5.5 SUMMARY

In this chapter, we have modeled and analyzed electrical switching of nonvolatile GST-clad integrated nanophotonic cells with graphene heaters on the programmable GST-on-silicon platform. By leveraging the ultra-low heat capacity and high in-plane thermal conductivity of graphene, a high switching speed of ~80 MHz and high energy efficiency of 19.2 aJ/nm^3 (6.6 aJ/nm^3) for crystallization (amorphization) are optimally achieved (via a thin film of GST and a short pulse optimized by high power) for complete phase transitions ensuring strong attenuation (~6.46 dB/μm) and optical phase (~0.28 π/μm at 1550 nm) modulation. Gigahertz operations and energy efficiency near the fundamental limit are possible for partial crystallization or amorphization during multi-level operations. Compared with ITO and silicon PIN diode heaters, the PINCs with graphene heaters have the best heating and overall performance with two orders of magnitude higher figure of merits. By gating the graphene to the Pauli blocking region, even better optical performance and lower operation voltage can be expected. To further optimize the heating performance and conduct multi-level operations, a single structured pulse or pulse sequences can be considered. The optical performance for multi-level operations can then be determined by the degree of crystallization according to the electro-thermal model [48,71]. With high speed, high energy efficiency, and small footprints while maintaining good optical performance, our proposed PINCs with graphene heaters allow scalable control over the states of PCMs and thus promise the development of the future large-scale PCM-based programmable PICs. The comprehensive model built in this work also assist the analysis and understanding of the thermal-conduction heating-enabled switching processes on PICs and facilitate the design and optimization of the PINC-based devices such as nonvolatile phase-change optical switches/modulators, directional couplers, photonic memories, and optical neurons and synapses.

Chapter 6.

EXPERIMENTAL DEMONSTRATION OF ELECTRICAL SWITCHING WITH PIN DIODE HEATERS

Guided by the theoretical modeling of electrical switching in the last chapter, we are now able to experimentally demonstrate electrical control of the GST-on-silicon platform. Recently, electrical switching with external heaters has shown promising results in PCM-integrated photonics [57,61,68,95]. However, in these demonstrations, a large insertion loss is incurred due to the use of ITO heaters [61,68,95] or uniformly doped silicon heaters [57], large driving voltages (> 10 V) are applied, and the number of switching cycles is limited to ~5–50.

In this chapter, we experimentally show that, by integrating GST on silicon PIN diode heaters, it is feasible to reversibly trigger large-area phase transitions with low voltages, near-zero additional, loss long endurance. Utilizing GST-on-silicon waveguides and microring resonators, we demonstrate CMOS-compatible, compact, and energy-efficient nonvolatile electrically reconfigurable photonic switching units that exhibit strong attenuation and optical phase modulation effects and are suitable for creating large-scale programmable electronic-photonic systems. This chapter is adapted with permission from Ref. [48]. Copyright 2020 Wiley-VCH.

6.1 EXPERIMENTAL METHOD

6.1.1 *Device Structure and Fabrication*

As illustrated in Figure 6.1a, our photonic switching units were similarly fabricated (see Chapter 2) based on the previously demonstrated GST-on-silicon platform. The rib waveguides, microring resonators, and grating couplers (with a pitch of 744 nm and a duty cycle of 0.5, inset of Figure 6.1b) were defined by EBL and etched by ICP-RIE. The partially etched silicon waveguide consists of a 500-nm-wide rib on a 100-nm-thick slab layer, supporting the propagation of single-mode transverse electric (TE) light. To form the PIN junction, the slab is heavily doped by boron and phosphorus ion implantation, 200 nm away from the left and right edge of the rib in the active region, respectively. The separation distance is close enough to the rib to reduce the resistance, but still far enough from the TE mode distribution to ensure a negligible optical loss. The doping concentration is chosen as 10^{20} cm^{-3} to achieve high conductivity as well as Ohmic contact with the Ti/Pd signal (S) and ground (G) electrodes for low-voltage operations. Specifically, the p++ (n++) region was defined by another EBL using 600-nm-thick PMMA resist and implanted by boron (phosphorus) ions with a dosage of 2×10^{15} ions/cm^2 and ion energy of 14 keV (40 keV). The ion implantation was conducted at a tilt angle of 7 degrees to misalign with the silicon lattice and thus achieve uniform deep doping. Subsequently, the chips were annealed at 950 °C for 10 mins to activate the dopants. Before metallization, the surface native oxide was removed by immersing the chips in 10:1 buffered oxide etchant (BOE) for 10 s to ensure Ohmic contact. The metal contacts were then immediately patterned by the fourth EBL using PMMA and formed by electron-beam evaporation (CHA SEC-600) and lift-off of Ti/Pd (5 nm/180 nm) layers. Pd is adopted because of its high temperature tolerance. After metallization, a 10-nm or 20-nm thin-film of GST patch was sputtered onto the EBL-defined window of the rib followed by a lift-off process, inducing strong mode modification upon phase transitions through evanescent coupling. The GST and part of the electrodes near the heating region were then encapsulated by 30-nm-thick Al_2O_3 through EBL patterning with PMMA, atomic layer deposition (ALD, Oxford Plasmalab 80PLUS OpAL ALD) at 100 °C, and lift-off (Figure 6.1a-c) to avoid oxidation and prevent the melted GST from reflowing and deforming during the amorphization process [61], thus allowing high cyclability of the device. Finally, RTA was performed to ensure the complete crystallization of the

GST. To obtain uniform heating and a large alignment tolerance in EBL, the width and the length (in the direction of light propagation) of the GST patch are set to be smaller than those of the rib in the active region by 50 nm on each side (Figure 6.1a,d).

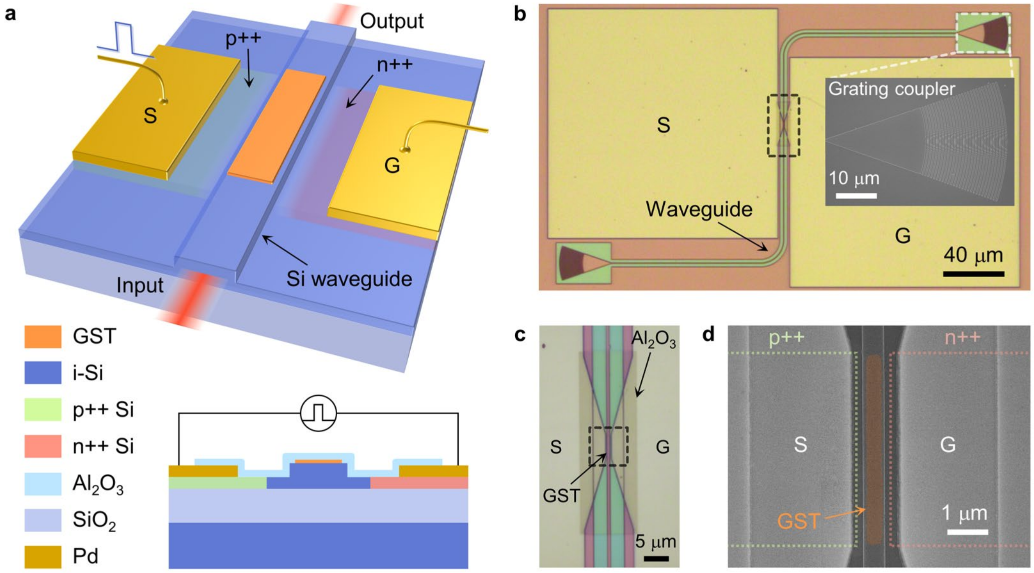

Figure 6.1. Nonvolatile electrically reconfigurable photonic switching units. (a) Schematic of the device. For clarity, the top thin-film Al_2O_3 encapsulating layer is not displayed. Inset: cross-section of the device. (b) Top-view optical microscope image of the switching unit on a waveguide with 10-nm-thick GST and a 5-μm-long active region. Inset: SEM image of the grating coupler. (c) Optical microscope image of the black dashed area in (b). (d) SEM image of the active region boxed in (c). False color is used to highlight the GST (orange). S (G), signal (ground) electrode. p++ (n++), heavily doped p (n)-type silicon region. i, intrinsic silicon region.

6.1.2 *Static Measurement*

The photonic switches were characterized by the same vertical fiber-coupling setup (see Chapter 2). All the measurements were performed under ambient conditions while the temperature of the stage was fixed at ~22 °C to prohibit the serious thermal shift of the resonators. Focusing grating couplers optimized for ~1550 nm were employed to couple light into and out of the devices operated at an angle of ~25 degrees. The power of the coupled light was kept to be sufficiently low (< 100 μW) in order to minimize the thermo-optic effects of GST [83] and silicon [84] and avoid causing any phase transition. Based on this setup, we performed the transmission spectrum measurement after each important fabrication step for all the devices including the reference devices without any doping, metal, or GST to assist the insertion loss analysis and normalization.

The setup used for static measurements including the transmission, I-V characteristic, and cyclability operations (to be discussed later) is shown in Figure 6.2a. To measure the I-V characteristic and conduct electrical switching, electrical signals were applied to the contacts by a pair of DC probes controlled by two probe positioners (Cascade Microtech DPP105-M-AI-S). In particular, the current sweep and voltage measurement were provided by a source meter (Keithley 2450) and the Set and Reset pulses were generated from a pulse function arbitrary generator (Keysight 81160A). The measured I-V curves were used to estimate the power of the applied pulses. By comparing the pulses directly from the pulse generator and those from the probes via a fast oscilloscope (Agilent DSO1022A), no signal distortion was found, suggesting that the probe system has enough response speed for the experiment. Limited by the low control speed of the pulse generator (each pulse takes over 0.1 s), cyclability operations with a higher order of magnitude will take hours and thus are not conducted since the setup will get badly misaligned within such long time.

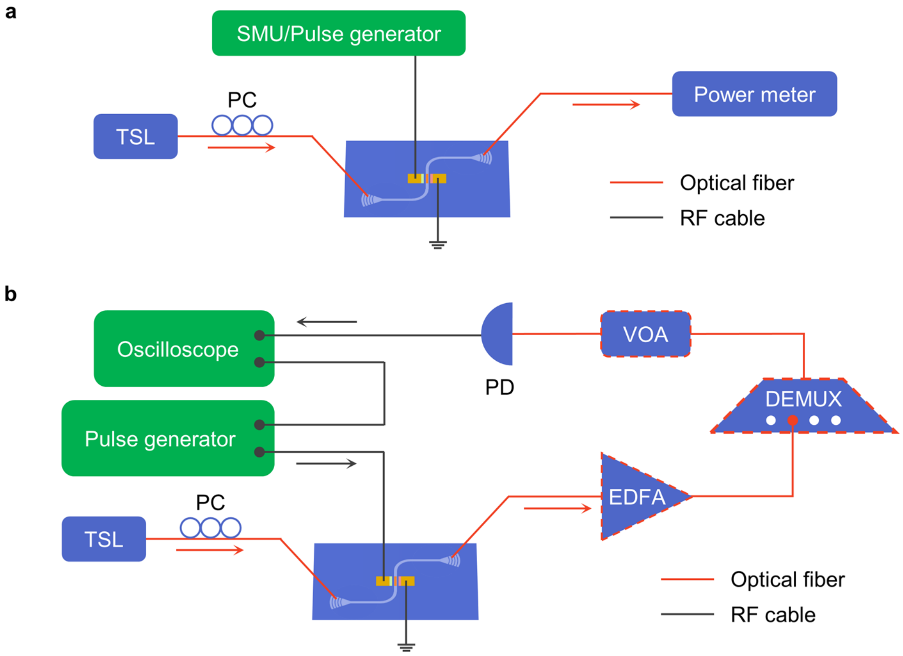

Figure 6.2. Experimental setups. (a) Setup for static measurement. (b) Setup for transient response measurement. The tools framed with dashed red lines were used for measuring the pulse width modulation (PWM) effects. TSL, tunable laser. PC, polarization controller. SMU, source meter unit. EDFA, erbium-doped fiber amplifier. DEMUX, optical demultiplexer. VOA, variable optical attenuator. PD, photodiode.

6.1.3 *Transient Response Measurement*

The setup used to measure the transient response of the photonic switching units due to electrical heating including phase transitions, pulse amplitude modulation (PAM), pulse width modulation (PWM), and real-time transmission of microring resonators at different wavelengths (to be discussed later) is shown in Figure 6.2b. To obtain the time-resolved response of the photonic switches under the electrical pulses, high-speed low-noise photoreceivers (New Focus 1811 and 1611) were used to measure the dynamic optical signals and the converted output electrical signals were recorded using the oscilloscope triggered by the applied pulses from the pulse generator. The 125-MHz photoreceiver (New Focus 1811) has enough response speed and appropriate linear operation region to analyze the process of phase transitions, PAM effects, and transient response of the microrings at different wavelengths. However, for the analysis of PWM effects, the 1-GHz photoreceiver (New Focus 1611) is necessary. Since its linear operation power is ~1 mW, the output light from grating couplers was first amplified by an optical fiber amplifier (Amonics AEDFA-30-B-FA) and filtered by a narrow-band optical demultiplexer (DEMUX, JDS WD1504D4A-DSC4). The power of the amplified light was then attenuated by a variable optical attenuator (Keysight 81570A) to meet the requirement of linear operation. In this experiment, the wavelength of the input light was fixed at 1549.32 nm in corresponding to the nominal central wavelength of the second channel of the DEMUX.

6.1.4 *Device Modeling and Simulation*

We also developed a coupled electro-thermal 2D FEM model to qualitatively simulate the electrical switching of the photonic devices with PIN diode heaters using the method described in Chapter 5. The schematic of the model was consistent with the actual device cross-section except that the dopants here were assumed to be uniformly distributed for the sake of simplicity.

The mode profiles of the photonic switching units were also modeled based on the same geometry but simulated using a frequency-domain 2D FEM wave optics model as described before. The carrier density and temperature distributions calculated from the electro-thermal model were employed to determine the complex refractive index of the materials (Table 6.1) during the Set and Reset processes. The transmission of the switching units was then estimated based on the solved effective indices. More sophisticated simulations can be conducted by including the kinetic models of melting, vitrification, nucleation, and growth [97] and applying accurate material parameters obtained by material characterizations in the future.

Table 6.1 lists the main material parameters used in this chapter. As the GST is partially crystallized during the phase transitions, the complex refractive index of GST was approximated from the effective permittivity equation based on an effective-medium theory [71] where the complex refractive index of the amorphous and crystalline GST and the degree of crystallization from the electro-thermal model were utilized.

Table 6.1. Main Material Parameters Used in the Chapter*

	n	**κ**	**β (K^{-1})**	**γ (K^{-1})**	**k_{th} ($W\ m^{-1}\ K^{-1}$)**	**C_p ($J\ kg^{-1}\ K^{-1}$)**	**ρ ($kg\ m^{-3}$)**
Si	$3.4777 + \Delta n$ [12]	$\Delta\kappa$ [12]	1.8×10^{-4}	—	$k_{th}(T)$ [113]	$C_p(T)$ [114]	2329
SiO_2	1.444	0	—	—	$k_{th}(T)$ from COMSOL	$C_p(T)$ from COMSOL	2200
Al_2O_3	1.5886	0	—	—	1.9 [123]	$C_p(T)$ [124]	3100
Pd	3.1640	8.2121	—	—	71.8	244	12023
aGST	3.8884 [39]	0.024694 [39]	1.1×10^{-3} [83]	4.1×10^{-4} [83]	0.19 [118]	213 [119]	5870 [120]
cGST	6.6308 [39]	1.0888 [39]	-2.2×10^{-4} [83]	1.56×10^{-3} [83]	$k_{th}(T)$ [118]	199 [119]	6270 [120]

*β, thermo-optic coefficient for refractive index. γ, thermo-optic coefficient for extinction coefficient. All the optical parameters are for 1550 nm. Δn and $\Delta\kappa$ are dependent on carrier densities of electrons and holes and can be calculated from Eq. (6.3) and Eq. (6.4) in Ref. [12].

6.2 OPERATING PRINCIPLE AND PERFORMANCE

In contrast to optical heating and electrical threshold switching, phase transitions of our photonic switching units rely on the transfer of the electrical pulse-generated Joule heat from the in-situ silicon waveguide PIN junctions. Hence, the switching region can be locally selected and be arbitrarily extended by increasing the size of the heaters, enabling large-scale integration and large-area functional devices such as directional couplers [55]. A 5-µm-long switching unit (*i.e.* the length of the GST patch is 4.9 µm) was operated here to demonstrate the transient response of the optical transmission (Figure 6.2b) and the simulated temperature distributions for the crystallization (Set) and amorphization (Reset) processes. For the Set process (Figure 6.3a), we applied a single pulse of 3.5 V (~10 mW) for 50 µs with a long falling edge of 30 µs (switching energy of ~650 nJ, 12-ns rising edge for all the pulses in this paper) to ensure that the GST was heated to just above its glass transition temperature (T_g) but below the melting point (T_m) for a long enough time. The nucleation of small crystallites and subsequent growth can, therefore, proceed, leading to an elevated refractive index (n) and extinction coefficient (κ) of the GST and a reduced optical transmission of the device after the pulse. For the Reset process (Figure 6.3b), a single pulse of 6.6 V (~110 mW) for 100 ns (switching energy of ~11 nJ) with a short falling edge of 12 ns (same for all the other Reset pulses) was utilized to melt the GST and then rapidly quench it below T_g, forming the disordered glass state with low optical constants and increased optical transmission of the device after the pulse. During the phase transitions, an ultrafast free-carrier absorption effect [36] due to the carrier injection into the silicon was observed from the steep change in the transmission at the sharp edges of the pulses. The slowly changed optical transmission at other times is, however, dominated by the thermo-optic effect of GST [83] in response to the heating and cooling processes. The overall switching period is then determined by the pulse width as well as the dead time due to the thermal relaxation (to be discussed later). Since the chip here was not ideally doped, the applied pulse voltages were higher than expected. This was improved in the following switching units on microring resonators that were actuated by much lower driving voltages.

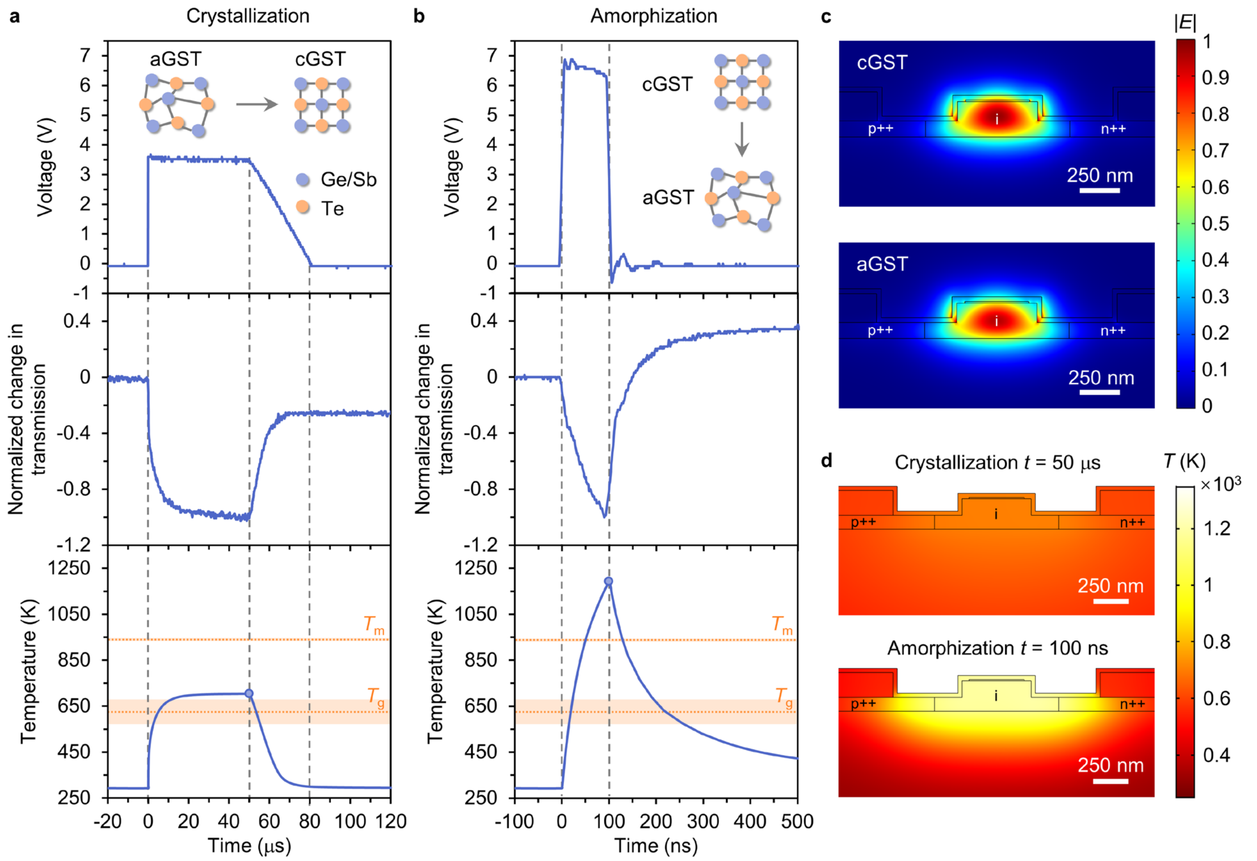

Figure 6.3. Operating principle of the photonic switching units. (a,b) Real-time voltage of the applied electrical pulse (upper panel), corresponding change in optical transmission (with the minimum value normalized to –1) of the switching unit at 1550 nm (middle panel), and simulated temperature response in the center of the GST cross-section to the equivalent pulse with the same power and width (lower panel) for crystallization (Set, a) and amorphization (Reset, b). Insets of the upper panels: schematic of the GST structure changes due to the phase transitions. The orange shaded areas in the lower panel represent the assumed temperature intervals where the properties of GST are weighted sums of those in the amorphous and crystalline states during phase transitions. T_g, glass transition temperature of GST. T_m, melting point of GST. (c) Simulated electric field (|E|) profiles for the fundamental quasi-TE mode of the switching unit at 1550 nm in the crystalline (top, $\tilde{n}_{\mathrm{eff}} = 2.68 - 0.05$ i) and amorphous (bottom, $\tilde{n}_{\mathrm{eff}} = 2.60 - 1.06 \times 10^{-3}$ i) states. (d) Simulated temperature (T) distributions of the switching unit cross-section for crystallization (top) and amorphization (bottom) at the time (t) marked by the dots in the lower panels of (a) and (b), respectively. p++ (n++), heavily doped p (n)-type silicon region. i, intrinsic silicon region. Here, the length of the switching unit is 5 μm and the thickness of the GST is 10 nm.

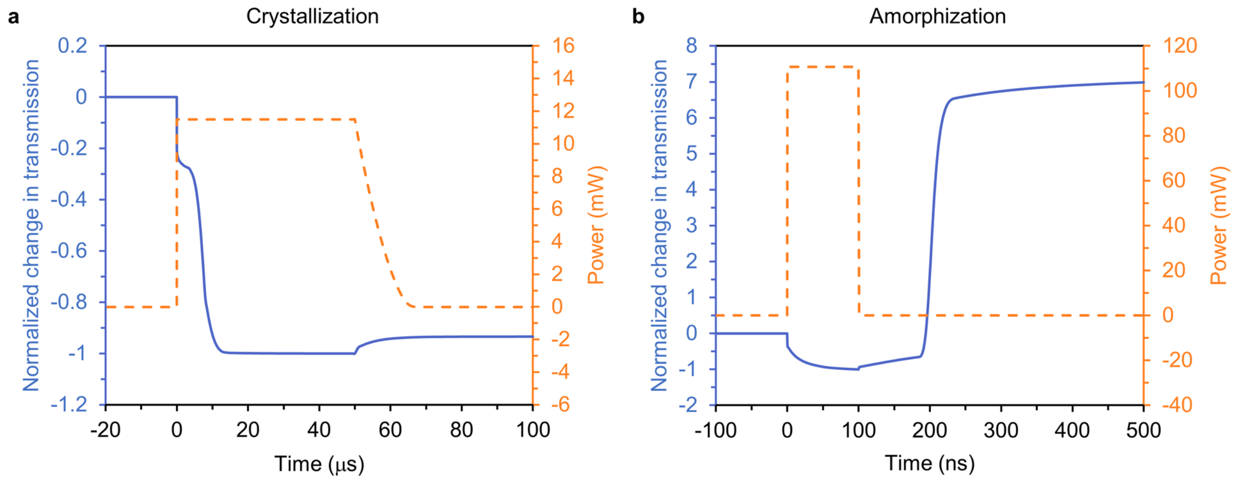

Figure 6.4. Real-time optical transmission during Set and Reset processes. (a,b) real-time power of the applied electrical pulse (dashed line, same as in Figure 6.3) and corresponding normalized change in optical transmission of the simulated switching unit at 1550 nm (solid line) for crystallization (Set, a) and amorphization (Reset, b). Here, the length of the switching unit is 5 μm and the thickness of the GST is 10 nm.

Strong mode modification is expected after the phase transitions according to the simulated mode profiles with amorphous and crystalline GST (Figure 6.3c), implying substantial absorptive and refractive modulation effects of our switching units. As the mode distribution is mostly confined in the transparent intrinsic region, near-zero additional loss (~0.02 dB/μm) is introduced by the PIN junction (to be discussed later), showing promising scalability for large-scale programmable photonic systems. To verify the phase transition processes, we further calculated the real-time optical transmission (Figure 6.4) due to the effective index change based on the simulated carrier density and temperature distributions (Figure 6.3d), exhibiting good qualitative agreement with the experiment. From the calculation, a similar steep change in the transmission at the sharp edges of the pulses can be observed, confirming the ultrafast free-carrier absorption in silicon. We can also find gradually varied transmission regions during the heating and cooling processes reflecting the thermo-optic effect of GST. However, the abrupt change of the transmission at around 10 μs for Set and 200 ns for Reset, where the crystallization (nucleation and growth) and vitrification happen, respectively, was not likewise found in the experiment. This discrepancy can be mainly attributed to the simple model of the phase transitions and the uncertainty in the material properties. The actual fraction of the GST undergoing phase transitions in the experiment is also not determined. Therefore, the calculated large change in the transmission might be over-estimated.

The Set process can also be actuated using current sweeps. Figure 6.5a presents the I–V characteristic of a photonic switching unit on a waveguide during and after the Set by a current sweep, showing a typical rectification behavior of PIN junctions. In contrast to electrical threshold switching [49], no abrupt change of the resistivity is observed in the I–V curves, confirming a different switching mechanism (*i.e.* electrical switching by external heaters) as the GST is not part of the electric circuit due to the relatively large resistance. The corresponding optical output under a current sweep (Figure 6.5b), however, does exhibit an obvious change due to the phase transition. Additionally, we find a transient gradual reduction of the output during the current sweep that can be again attributed to the carrier-injection induced loss from silicon and the thermo-optic effect of GST. Manually applying a current sweep (0–15 mA) and a Reset pulse (a single pulse of 4.3 V for 100 ns) shows that the device can be reversibly switched with a high extinction ratio of ~5 dB (1.25 dB/μm for 20-nm-thick GST) over a broad spectral range (Figure 6.5c). It is notable that although the energy consumption of one switching cycle may be larger compared with electro-optic switches or comparable with thermo-optic switches, due to the nonvolatility of GST, the output states are self-held, precluding any need for external control after the phase transitions. This nonvolatility leads to highly energy-efficient operations.

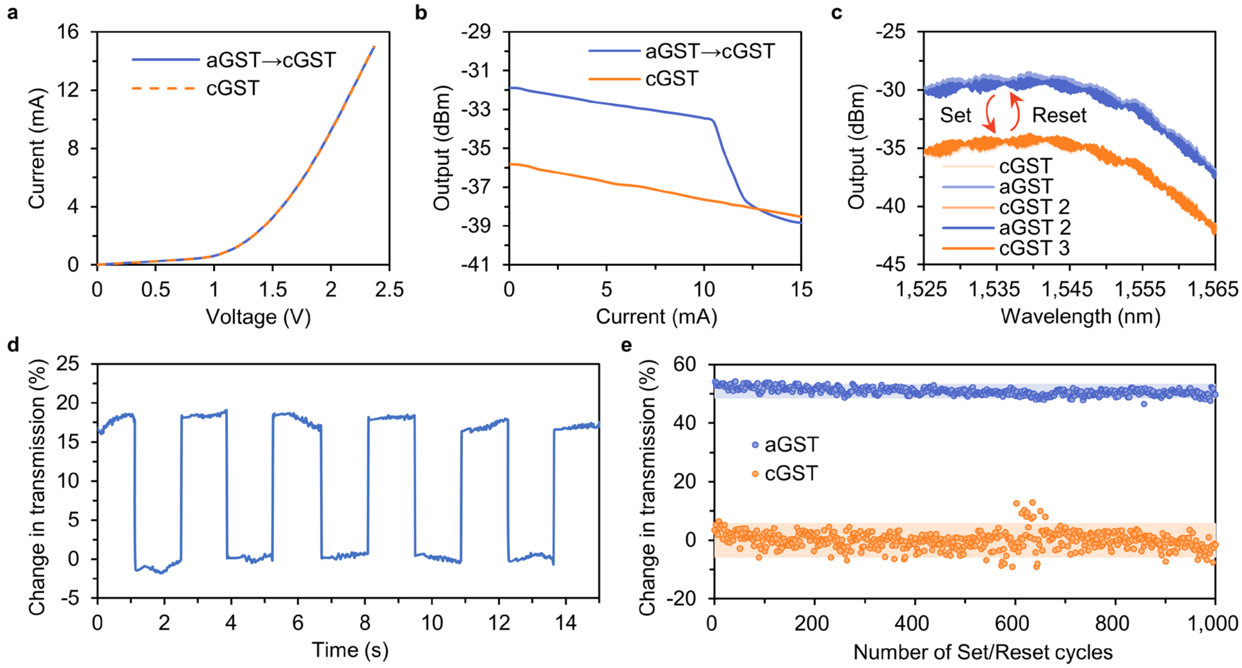

Figure 6.5. Performance of the photonic switching units on waveguides. (a) I–V curves of the photonic switch with 20-nm-thick GST and a 4-µm-long active region obtained via current sweeps (0–15 mA) during and after the Set process, exhibiting a typical rectification behavior of PIN diodes without the electrical threshold switching effect. (b) Corresponding optical output under current sweeps at 1550 nm, showing an abrupt change during the Set process. (c) Optical output spectra of the same device after two reversible Set (0–15 mA sweep) and Reset (a single pulse of 4.3 V or ~200 mW for 100 ns) processes. The periodic fringes in the spectra are due to the back reflection between the input and output grating couplers. (d) Temporal trace of the transmission change in a photonic switch with 10-nm-thick GST and a 4-µm-long active region at 1550 nm during the consecutive Set (a single pulse of 3.4 V or ~8 mW for 1 ms with a falling edge of 0.6 ms) and Reset (a single pulse of 7.1 V or ~140 mW for 100 ns) steps. The sampling rate is ~50 Hz. (e) Cyclability of the transmission change of a photonic switch with 10-nm-thick GST and a 5-µm-long active region at 1550 nm under multiple Set (3.1 V or ~11 mW for 50 µs, 30-µs falling edge, ~715 nJ) and Reset (7 V or ~130 mW for 100 ns, ~13 nJ) cycles. Each pulse is temporally separated by more than 100 µs to ensure long enough thermal relaxation. The blue and orange shaded areas represent the two-standard-deviation intervals for the amorphous and crystalline states, respectively. aGST (cGST), amorphous (crystalline) GST.

To further inspect the state retention and the cyclability of the switching units on waveguides, we applied numerous Set and Reset pulses and recorded the temporal trace (Figure 6.5d) and static states (Figure 6.5e) of the transmission change. The results show that our devices allow stable binary operations with reversible phase transitions over more than 1000 times. No obvious performance degradation was found after repeating the same experiment (1000 transitions) for several times, implying that a significantly longer endurance can be expected. The transmission fluctuation in Figure 6.5d is primarily caused by the gradual misalignment of the setup (Figure 6.2a) during the measurement while a relatively large uncertainty of the transmission in the crystalline state (Figure 6.5e) can be explained due to partial crystallization of the GST.

6.3 APPLICATION IN MICRORING RESONATORS

By integrating the photonic switching units on microring resonators (Figure 6.6a,b), we can achieve even higher optical contrast from such a compact structure by taking the advantages of both the strong attenuation and optical phase modulation effects of GST at the cost of less switching energy. Figure 6.6c shows the transmission spectra of a microring resonator with a radius of 20 μm integrated with a 3-μm-long switching unit covered with 10-nm-thick GST. After several Set and Reset cycles, the spectra remain the same, indicating reversible phase transitions. Thanks to the better doping-induced electrical conductivity in this chip, much lower driving voltages for Set (1 V) and Reset (2.5 V) were required in this experiment. As a result of the combined effects of the resonance shift (~0.02 nm/μm switching unit length) and resonance dip (linewidth and depth) change due to the loss modulation (~0.25 dB/μm switching unit length) upon phase transitions (extracted by the same method as described in Chapter 2), a high on-off extinction ratio up to 14.7 dB was achieved near the resonance wavelength while the total switching energy of a cycle is only ~86 nJ much less than that for the photonic switching units on waveguides with the same GST area or the same switching contrast.

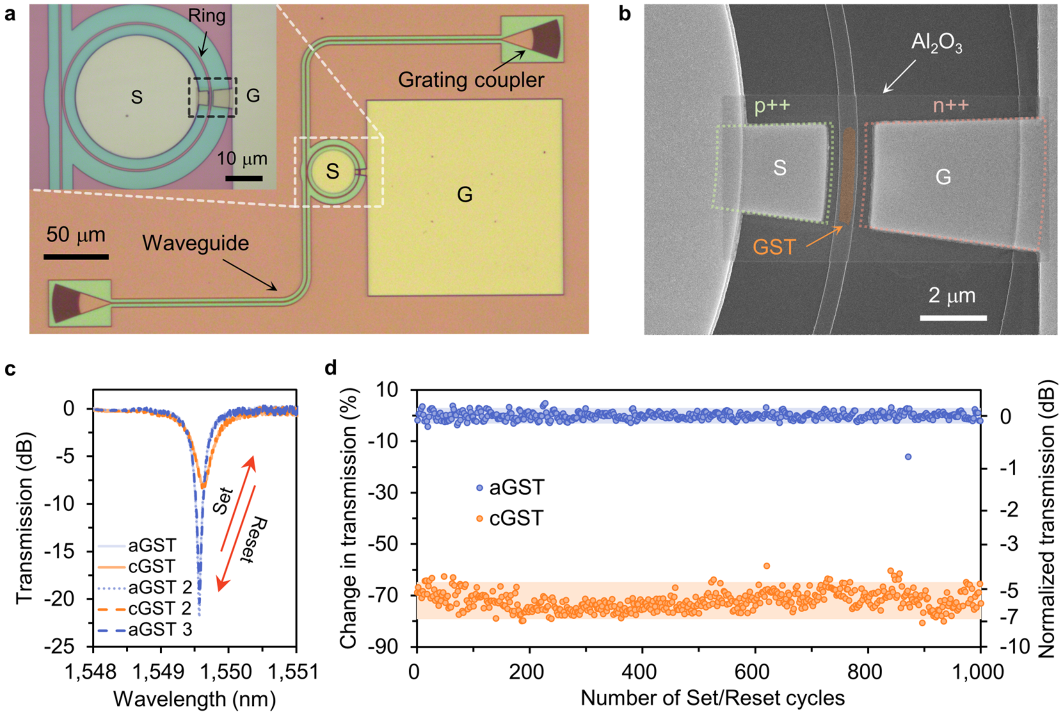

Figure 6.6. Photonic switching units on microring resonators. (a) Top-view optical microscope image of the switching unit on an all-pass microring resonator. Inset: enlarged view of the ring. (b) SEM image of the black dashed area in the inset of (A). False color is used to highlight the GST (orange). S (G), signal (ground) electrode. p++ (n++), heavily doped p (n)-type silicon region. (c) Transmission spectra of a ring switch after a few reversible Set and Reset processes. (d) Cyclability of the transmission change and normalized transmission of a ring switch at 1549.57 nm under multiple Set and Reset cycles. Each pulse is temporally separated by more than 0.1 s. The blue and orange shaded areas represent the two-standard-deviation intervals for the amorphous and crystalline states, respectively. Here, the radius of the rings is 20 μm, the gap between the rings and the bus waveguides is 240 nm, the length of the switching units is 3 μm, and the thickness of the GST is 10 nm. Set, a single pulse of 1 V or ~0.6 mW for 100 μs with a falling edge of 60 μs, ~78 nJ. Reset, a single pulse of 2.5 V or ~80 mW for 100 ns, ~8 nJ. aGST (cGST), amorphous (crystalline) GST.

High cyclability with over more than 1000 phase transitions was also realized (Figure 6.6d) in a microring-based switch with the same structure. Note that due to a slight shift between the probe laser wavelength and the ring resonance, the extinction ratio here is not optimal. The relatively large uncertainty of the transmission in the crystalline state can be attributed to the thermal shift of the resonance wavelength and partial crystallization.

6.4 DISCUSSION

In this section, we discuss the insertion loss and analyze the heating dynamics of the GST-based photonic switching units.

6.4.1 *Insertion Loss*

To analyze the insertion loss (IL) of the photonic switching units, we first performed the mode analysis simulation for the nominal waveguide structures with geometric parameters as outlined in the fabrication processes. The refractive indices of the materials used in the simulation can be found in Table 6.1. As listed in Table 6.2, near-zero additional loss (6.77×10^{-3} dB/µm) is introduced due to the doping and annealing. Metal contacts bring about an IL of ~0.017 dB/µm. Considering that we used relatively thick electrodes (~180 nm) for a good connection near the etching steps and the electrodes were put only 500 nm away from the waveguides to ensure low resistance, a lower IL can be achieved by reducing the thickness of the metal contacts and increasing their distance from the waveguides with improved fabrication. Amorphous GST also introduces a moderate IL of ~0.012 dB/µm. The total IL, defined as the loss in the amorphous state, is thus the sum of the IL from the above sources and is ~0.035 dB/µm. By comparing the loss between the amorphous and crystalline states, we can acquire a theoretical on-off extinction ratio (ER) of ~1.77 dB/µm. Note that from the effective index change, we can also expect a resonance shift of ~0.48 nm/μm for a microring resonator with a radius of 20 μm through Eq. (2) in Chapter 2. The lower experimental result (~0.02 nm/μm) can be attributed to partial crystallization and potential material degradation during the fabrication processes.

Table 6.2. Simulated Complex Effective Index and Attenuation Coefficient of the Photonic Switching Unit after Each Important Fabrication Step at 1550 nm

	n_{eff}	κ_{eff}	α (dB/μm)
As-fabricated rib waveguide	2.55	0	0
After doping and annealing	2.55	1.92×10^{-4}	6.77×10^{-3}
After metallization	2.55	6.61×10^{-4}	2.33×10^{-2}
After sputtering (10 nm aGST)	2.58	9.98×10^{-4}	3.51×10^{-2}
After RTA (10 nm cGST)	2.68	0.05	1.81

The IL can also be evaluated through the measured transmission spectra of the waveguides after each important fabrication step. For waveguides, the IL due to a certain fabrication step is calculated as the difference of the transmission differences between the target and reference device (with the same structure but without any doping, metal, or GST) before and after the fabrication step. The reference devices were used to exclude the IL from the grating couplers and alignment variances. As shown in Figure 6.7a, the IL induced by the doping and annealing is less than 0.4 dB for the 5-μm-long switching unit, but it is difficult to determine the exact IL because of the ripples from the back reflection and the normalization error from the reference device. A larger IL compared to the simulation is also possible due to extra scattering loss. The IL from metal contacts is ~1 dB which is significantly higher than the theoretical value. This can be attributed to the positional deviation of the electrodes owing to the limited alignment precision. The IL introduced by amorphous GST is ~0.4 dB which is still higher than expected and can be explained by the unwanted scattering loss due to the surface roughness of GST (see Chapter 2). The total IL is thus around 1.6 dB while the ER is ~1.2 dB. The lower ER compared to the simulation is also attributed to partial crystallization and material degradation.

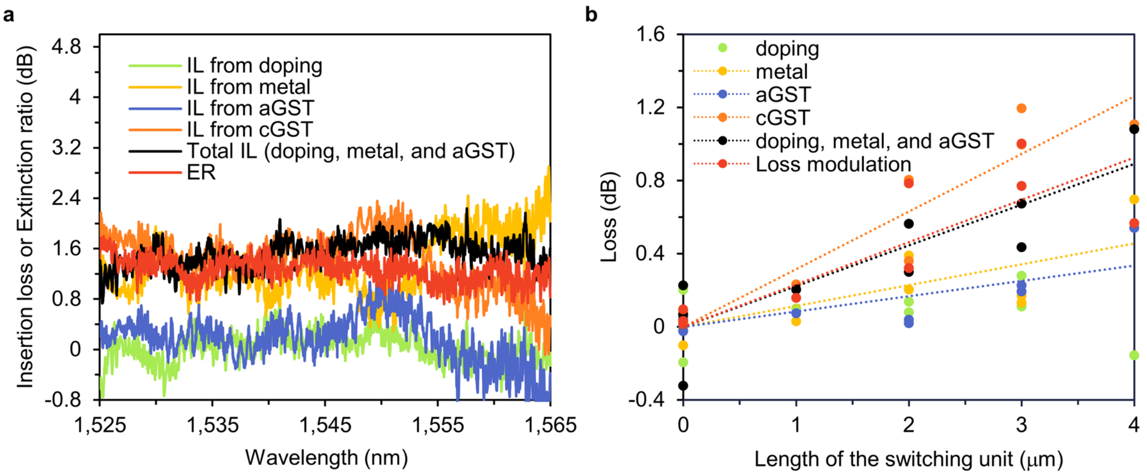

Figure 6.7. Insertion loss analysis based on experimental results. (a) Insertion loss (IL) spectra introduced by each important fabrication step and extinction ratio (ER) between two states of a photonic switching unit on a waveguide with 10-nm-thick GST and a 5-μm-long active region (same device as in Figure 6.5e). (b) Loss from each important fabrication step and loss modulation of microring resonators with different lengths of switching units near 1550 nm. Here, the radius of the rings is 20 μm, the gaps between the rings and the bus waveguides are 240 nm, 270 nm, or 330 nm, and the thickness of the GST is 10 nm. Every dot represents the experiment data of a single device. The dotted lines are the linear fitting of the experiments.

Additionally, IL analysis can be performed by the length-dependent loss statistics from microring resonators. In particular, the quality factors and resonance wavelengths of resonance dips for the rings with different lengths of switching units were first extracted by fitting the measured spectra to a Lorentzian function. The loss introduced by each fabrication step can then be estimated as the difference in the loss of the rings before and after the step through Eq. (1) in Chapter 2. As plotted in Figure 6.7b, the loss from each step except doping is linearly proportional to the length of the switching units while the loss due to doping randomly locates near 0 dB, suggesting a negligible additional loss from the PIN junction. As a result, we estimated the IL from metal contacts to be ~0.1 dB/μm, the IL from amorphous GST to be ~0.08 dB/μm, the total IL to be ~0.2 dB/μm, and the IL from crystalline GST to be ~0.3 dB/μm. Therefore, the IL from doping is calculated to be ~0.02 dB/μm and the loss modulation between two states to be ~0.23 dB/μm. These results are comparable with those estimated by the single waveguide.

6.4.2 *Heating Dynamics*

We studied the heating dynamics of our photonic switching systems by PAM, PWM and microring resonators. During the whole experiment, the GST was kept in the crystalline state by pumping with extremely low pulse energy.

For PAM, electrical pulses with a fixed width and variable amplitudes were employed to a switching unit on a waveguide. As presented in Figure 6.8a, with the increase of the pulse amplitude, the dynamic change in the transmission increases accordingly. Note that this transmission change originates from the ultrafast free-carrier absorption effect of silicon and the slow thermo-optic effect of GST. The rise time and the dead time (cooling time constant) of the system, however, remain the same, suggesting a pulse amplitude-independent heating and cooling rate. Whereas the heating dynamics does not rely on the pulse amplitude, PWM, where the pulse width was varied but the pulse amplitude was fixed, displays considerably higher cooling rates for shorter pulses (Figure 6.8b). This could be intuitively understood that for longer pulses, more energy will get lost into the waveguide and substrate due to the thermal diffusion [58,60], so that a larger heat capacity and a longer thermal time constant are expected leading to a longer dead time. Hence, in order to ensure low energy consumption and high-speed operations, relatively short pulses are preferred. Considering that the temperature gradient in the GST increases significantly with the increase of pulse amplitude (see Chapter 5), pulses with low voltage are also desirable to avoid re-amorphization, ablation, and melting of silicon.

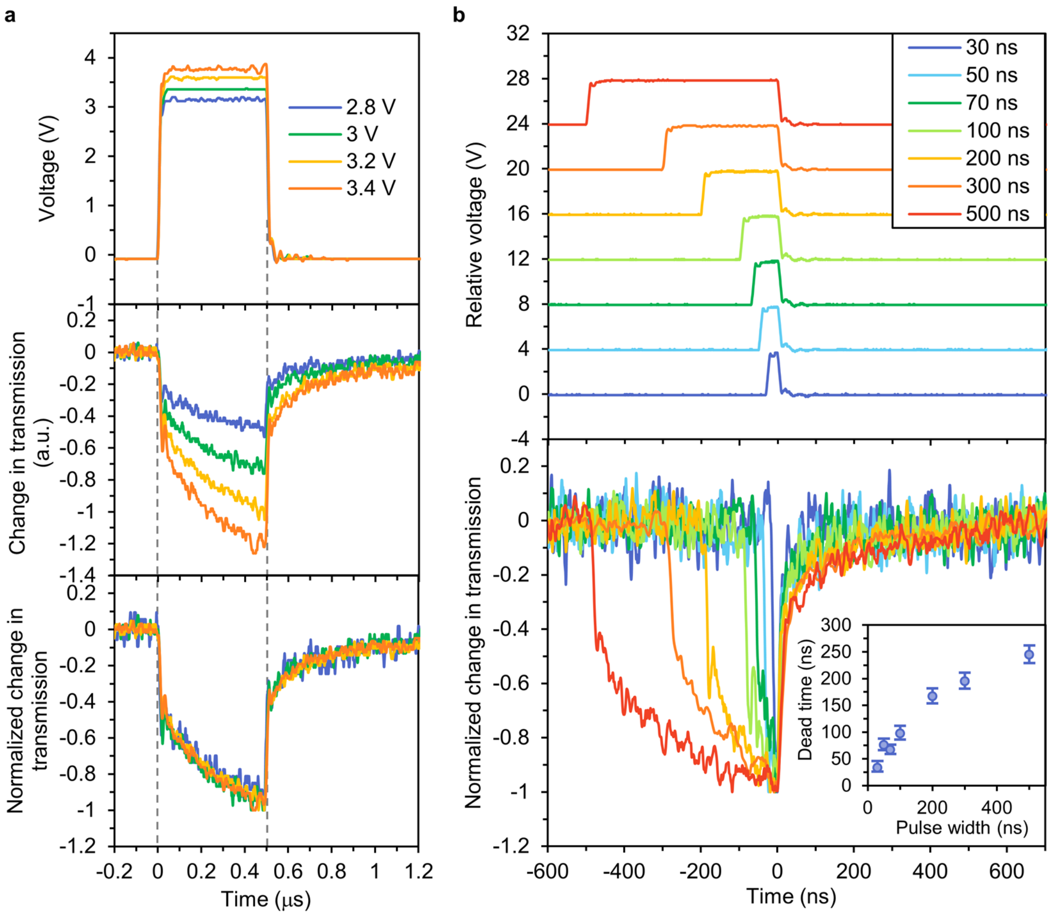

Figure 6.8. Heating dynamics of the photonic switching unit on the waveguide. (a) Electrical pulses (upper panel), corresponding transmission response (middle panel) and its normalization (lower panel) of the switching unit at 1550 nm for pulse amplitude modulation (PAM). (b) Electrical pulses (upper panel) and normalized transmission response (lower panel) of the switching unit at 1550 nm for pulse width modulation (PWM). The curves of the electrical pulses with different pulse widths have been vertically offset for clarity. Inset of lower panel: extracted dead time (1/e cooling time) as a function of pulse width with 95% confidence bounds. Here, the length of the switching unit is 5 μm and the thickness of the GST is 10 nm (same device as in Figure 6.3). The pulse energy was chosen to be sufficiently low to prevent any phase transition.

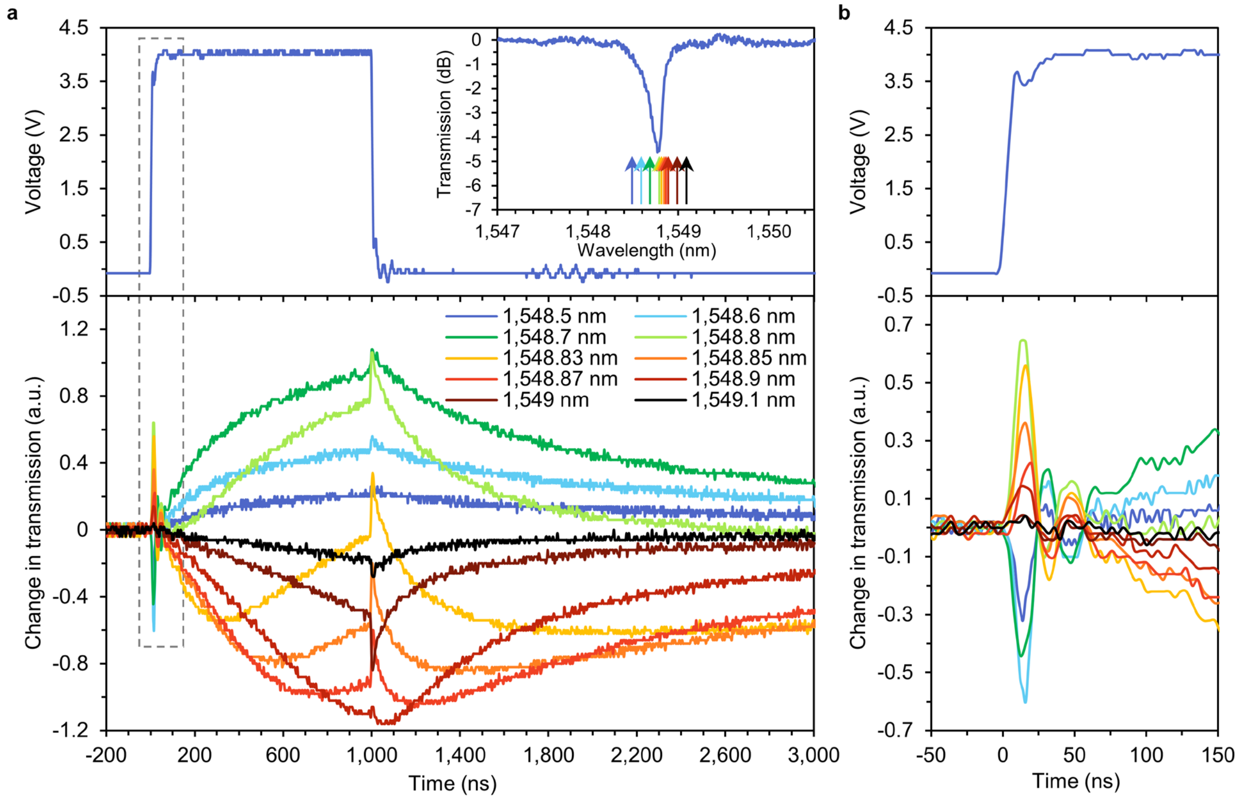

Figure 6.9. Heating dynamics of the switching unit on the microring resonator. (a) Electrical pulse (upper panel) and corresponding transmission response (lower panel) of the ring measured at different wavelengths. Inset of upper panel: transmission spectrum of the ring without any voltage applied. The probe wavelengths are annotated in the spectrum by the arrows using the same colors as in the lower panel. (b) Zoom-in inspection of the grey dashed area in (a), indicating a combination of the free-carrier effect and cavity oscillatory behavior in response to the step signal. Here, the radius of the ring is 20 μm, the gap between the rings and the bus waveguides is 330 nm, the length of the switching unit is 2 μm, and the thickness of the GST is 10 nm. The pulse energy was chosen to be sufficiently low to prevent any phase transition.

From the real-time optical transmission of a switching unit on a microring resonator (Figure 6.9), dynamic optical phase modulation can be observed. Here, the probe wavelengths (inset of Figure 6.9a) were selected to be gradually shifted from the left side of the resonance to the right side. Due to the ultrafast free-carrier dispersion and absorption effect of silicon, the resonance shift and resonance dip (linewidth and depth) change happen immediately at the beginning and end of the pulse, resulting in a sharp change in the transmission. The slowly varied optical transmission at other times is, however, dominated by the resonance shift due to the thermo-optic effect of silicon. Oscillatory behavior in the transmitted light (Figure 6.9b) was also observed at the rising edge of the pulse, which is the signature of the second-order filter and occurs due to the high quality factor (*Q*) of the optical cavity [125]. This behavior is, however, absent at the falling edge owing to the fact that the elevated loss from the GST at higher temperatures renders a low-*Q* resonator.

6.5 SUMMARY

In summary, we have demonstrated nonvolatile electrically reconfigurable PCM-integrated photonic switches with near-zero additional insertion loss (~0.02 dB/μm) and high endurance (> 1000 transitions) using in-situ silicon waveguide PIN heaters. By leveraging the remarkable broadband attenuation and optical phase modulation of GST, high extinction ratios are obtained within small footprints (1.25 dB/μm for waveguides and ~15 dB for a microring with a 3-μm-long switching unit) under low driving voltages (down to 1 V for Set and 2.5 V for Reset). The static (nonvolatile) nature of the modulation ensures intrinsically high energy-efficiency. We expect that the extinction ratio can be further improved by carefully choosing the power of the applied pulses to achieve complete phase transitions or simply increase the length of the switching units. Multi-level operations can be potentially achieved when the intermediate states are reached via engineering pulse shape, power, and duration [3,39,57-59,61-63,72]. The insertion loss of the devices can be reduced through thinner electrodes and improved fabrication as well as emerging wide-bandgap PCMs [93,94]. Moreover, the speed of the devices (reported in our paper ~10 kHz) can be enhanced to as fast as ~4 MHz by optimally increasing the pulse power to reduce the pulse width and dead time without inducing re-amorphization or ablation (see Chapter 5). However, the error tolerance in setting the electrical power decreases with the increase of the pulse power and a better-controlled environment will be needed to avoid any damage to the GST. To realize multi-port and broadband photonic switches, our photonic switching units can be integrated on the previously discussed three-waveguide directional coupler structure (see Chapter 4). The devices can also be similarly applied to more commonly used SiO_2-clad silicon PICs without losing their high performance (see Chapter 5). With low-energy, compact, low-loss, low-voltage, and high-cyclability operations at moderate speeds as well as the easy-to-deposit property of PCMs and the mature CMOS technology for silicon PIN diodes, our static photonic switching units promise large-scale integration of programmable PICs and pave the way for CMOS-integrated programmable electronic-photonic systems such as ONNs and optical FPGAs.

Chapter 7.

CONCLUSIONS AND OUTLOOK

In conclusion, to support large-scale programmable photonic networks for the future photonic information processing, we have demonstrated an energy-efficient and compact nonvolatile integrated phase-change photonic platform with strong broadband attenuation modulation and optical phase modulation using GST-clad silicon waveguides. Based on this platform, we have developed reversible all-optical multi-level operation (of a high-extinction-ratio microring switch), low-loss broadband multi-port directional coupler switches, and models and prototypes of highly scalable electrical control techniques.

In order to further improve the performance of the platform and realize chip-scale PCM-based programmable electronic-photonic systems, it is worthwhile to explore the following directions:

- Transparent PCMs: As discussed in Chapter 5, the extinction coefficient of the PCMs in the amorphous state determines the ultimate intrinsic insertion loss of the devices for optical phase modulation and the previously discussed phase-change coupling modulation. It is exceptionally desirable to find a wide-bandgap PCM with a negligible extinction coefficient but, in the meanwhile, a high refractive index contrast at the wavelengths of interest. Recently, several groups have explored the properties and switching processes of such transparent PCMs including $Ge_2Sb_2Se_4Te_1$ (GSST) [94] and Sb_2S_3 (Stibnite) [93]. Amorphous GSST has shown a broadband transparent window in the IR region. Widely available Sb_2S_3 has a bandgap of ~2 eV in the amorphous state, so it enables lossless operation in the visible range. We have preliminarily shown that Sb_2S_3 also has a very low loss in the near-IR [126]. Reversible electrical switching of Sb_2S_3 on PICs is the next step.

- Tunable beam splitter and phase shifter: For programmable PICs, several intermediate states between cross and bar states are required meaning that the switch needs to act as a tunable beam splitter. While it is simple to achieve in the conventional MZI-based switches by thermo-optic or electro-optic phase tuning, it is not very straightforward for our multi-port DC-based structures since the ideal device intermediate states cannot be obtained through partial crystallization. Due to the intrinsic length-dependent property of DCs, we need to segmentally actuate the PCMs (inducing strong mode modification) to achieve different effective coupling lengths corresponding to different intermediate states. In addition to the intensity modulation, phase information is also of importance to programmable photonics where phase shifters are usually necessary. Unfortunately, due to the high loss from the PCMs in the crystalline state, it is also not straightforward to make a low-loss phase shifter using PCMs [95]. Recent simulations show that this could be realized relying on a similar coupling mechanism as reported in Chapter 4 [127]. Electrical switching of the tunable beam splitters and phase shifters with high performance is another direction.
- PCM-integrated ONNs: With the electrically controlled high-performance tunable beam splitters and phase shifters based on the transparent PCMs, large-scale programmable electronic-photonic systems such as ONNs and optical FPGAs can be accomplished. As one of the promising non-von Neumann computing approaches, neuromorphic computing has raised intensive attention [7]. Although several PCM-based ONNs has been proposed [71] and demonstrated [24,72], large-scale PCM-based ONNs involving training that can compete with their electronic equivalents [8,128,129] are yet to be resolved. Recently,

based on the binary convolutional neural network—XNOR-Net [130], a PCM-integrated accelerator is proposed [131], suggesting new directions in this field.

- Novel devices. The unique properties of PCMs potentially enable many innovative applications with small footprints and high energy-efficiency, such as mixed-mode operations [51,73], optical limiters [132], tunable optical filters [133], mode [134] and polarization [135] management, and so on. Realization of these devices on PICs can add more functions to programmable photonics.

BIBLIOGRAPHY

[1] M. M. Waldrop, "The chips are down for Moore's law," Nature **530**(7589), 144 (2016).

[2] Z. Ying, C. Feng, Z. Zhao, S. Dhar, H. Dalir, J. Gu, Y. Cheng, R. Soref, D. Z. Pan, and R. T. Chen, "Electronic-photonic arithmetic logic unit for high-speed computing," Nat. Commun. **11**(1), 2154 (2020).

[3] J. Feldmann, M. Stegmaier, N. Gruhler, C. Rios, H. Bhaskaran, C. D. Wright, and W. H. P. Pernice, "Calculating with light using a chip-scale all-optical abacus," Nat. Commun. **8**(1), 1256 (2017).

[4] M. M. Shulaker, G. Hills, N. Patil, H. Wei, H. Y. Chen, H. S. PhilipWong, and S. Mitra, "Carbon nanotube computer," Nature **501**(7468), 526-530 (2013).

[5] K. Kim, J. Y. Choi, T. Kim, S. H. Cho, and H. J. Chung, "A role for graphene in silicon-based semiconductor devices," Nature **479**(7373), 338-344 (2011).

[6] D. Akinwande, C. Huyghebaert, C. H. Wang, M. I. Serna, S. Goossens, L. J. Li, H. S. P. Wong, and F. H. L. Koppens, "Graphene and two-dimensional materials for silicon technology," Nature **573**(7775), 507-518 (2019).

[7] Y. LeCun, Y. Bengio, and G. Hinton, "Deep learning," Nature **521**(7553), 436-444 (2015).

[8] D. Ielmini, and H. S. P. Wong, "In-memory computing with resistive switching devices," Nat Electron **1**(6), 333-343 (2018).

[9] J. J. L. Morton, D. R. McCamey, M. A. Eriksson, and S. A. Lyon, "Embracing the quantum limit in silicon computing," Nature **479**(7373), 345-353 (2011).

[10] A. M. Ionescu, and H. Riel, "Tunnel field-effect transistors as energy-efficient electronic switches," Nature **479**(7373), 329-337 (2011).

[11] S. A. Wolf, D. D. Awschalom, R. A. Buhrman, J. M. Daughton, S. von Molnar, M. L. Roukes, A. Y. Chtchelkanova, and D. M. Treger, "Spintronics: A spin-based electronics vision for the future," Science **294**(5546), 1488-1495 (2001).

[12] L. Chrostowski, and M. Hochberg, *Silicon photonics design: from devices to systems* (Cambridge University Press, 2015).

[13] M. Hochberg, and T. Baehr-Jones, "Towards fabless silicon photonics," Nat. Photon. **4**(8), 492-494 (2010).

[14] C. Sun, M. T. Wade, Y. Lee, J. S. Orcutt, L. Alloatti, M. S. Georgas, A. S. Waterman, J. M. Shainline, R. R. Avizienis, S. Lin, B. R. Moss, R. Kumar, F. Pavanello, A. H. Atabaki, H. M. Cook, A. J. Ou, J. C. Leu, Y. H. Chen, K. Asanovic, R. J. Ram, M. A. Popovic, and V. M. Stojanovic, "Single-chip microprocessor that communicates directly using light," Nature **528**(7583), 534-538 (2015).

[15] A. H. Atabaki, S. Moazeni, F. Pavanello, H. Gevorgyan, J. Notaros, L. Alloatti, M. T. Wade, C. Sun, S. A. Kruger, H. Y. Meng, K. Al Qubaisi, I. Wang, B. H. Zhang, A. Khilo, C. V. Baiocco, M. A. Popovic, V. M. Stojanovic, and R. J. Ram, "Integrating photonics with silicon nanoelectronics for the next generation of systems on a chip," Nature **556**(7701), 349-354 (2018).

[16] J. Wang, S. Paesani, Y. H. Ding, R. Santagati, P. Skrzypczyk, A. Salavrakos, J. Tura, R. Augusiak, L. Mancinska, D. Bacco, D. Bonneau, J. W. Silverstone, Q. H. Gong, A. Acin, K. Rottwitt, L. K. Oxenlowe, J. L. O'Brien, A. Laing, and M. G. Thompson, "Multidimensional quantum entanglement with large-scale integrated optics," Science **360**(6386), 285-291 (2018).

[17] Y. Shen, N. C. Harris, S. Skirlo, M. Prabhu, T. Baehr-Jones, M. Hochberg, X. Sun, S. J. Zhao, H. Larochelle, D. Englund, and M. Soljacic, "Deep learning with coherent nanophotonic circuits," Nat. Photon. **11**(7), 441-446 (2017).

[18] N. C. Harris, G. R. Steinbrecher, M. Prabhu, Y. Lahini, J. Mower, D. Bunandar, C. C. Chen, F. N. C. Wong, T. Baehr-Jones, M. Hochberg, S. Lloyd, and D. Englund, "Quantum transport simulations in a programmable nanophotonic processor," Nat. Photon. **11**(7), 447-452 (2017).

[19] L. Zhuang, C. G. H. Roeloffzen, M. Hoekman, K. J. Boller, and A. J. Lowery, "Programmable photonic signal processor chip for radiofrequency applications," Optica **2**(10), 854-859 (2015).

[20] W. Liu, M. Li, R. S. Guzzon, E. J. Norberg, J. S. Parker, M. Z. Lu, L. A. Coldren, and J. P. Yao, "A fully reconfigurable photonic integrated signal processor," Nat. Photon. **10**(3), 190-195 (2016).

[21] D. A. B. Miller, "SILICON PHOTONICS Meshing optics with applications," Nat. Photon. **11**(7), 403-404 (2017).

[22] J. W. Goodman, *Introduction to Fourier optics* (Roberts and Company Publishers, 2005).

[23] J. Feldmann, N. Youngblood, M. Karpov, H. Gehring, X. Li, M. L. Gallo, X. Fu, A. Lukashchuk, A. Raja, and J. Liu, "Parallel convolution processing using an integrated photonic tensor core," arXiv preprint arXiv:2002.00281 (2020).

[24] C. Wu, H. Yu, S. Lee, R. Peng, I. Takeuchi, and M. Li, "Programmable Phase-change Metasurface for Multimode Photonic Convolutional Neural Network," arXiv preprint arXiv:2004.10651 (2020).

[25] O. Graydon, "Birth of the programmable optical chip," Nat. Photon. **10**(1), 1-1 (2016).

[26] N. C. Harris, J. Carolan, D. Bunandar, M. Prabhu, M. Hochberg, T. Baehr-Jones, M. L. Fanto, A. M. Smith, C. C. Tison, P. M. Alsing, and D. Englund, "Linear programmable nanophotonic processors," Optica **5**(12), 1623-1631 (2018).

[27] D. Perez, I. Gasulla, and J. Capmany, "Programmable multifunctional integrated nanophotonics," Nanophotonics-Berlin **7**(8), 1351-1371 (2018).

[28] D. Perez, I. Gasulla, L. Crudgington, D. J. Thomson, A. Z. Khokhar, K. Li, W. Cao, G. Z. Mashanovich, and J. Capmany, "Multipurpose silicon photonics signal processor core," Nat. Commun. **8**(1), 636 (2017).

[29] S. Chen, Y. Shi, S. He, and D. Dai, "Low-loss and broadband 2 x 2 silicon thermo-optic Mach-Zehnder switch with bent directional couplers," Opt. Lett. **41**(4), 836-839 (2016).

[30] L. H. Yu, Y. L. Yin, Y. C. Shi, D. X. Dai, and S. L. He, "Thermally tunable silicon photonic microdisk resonator with transparent graphene nanoheaters," Optica **3**(2), 159-166 (2016).

[31] L. Lu, S. Y. Zhao, L. J. Zhou, D. Li, Z. X. Li, M. J. Wang, X. W. Li, and J. P. Chen, "16 x 16 non-blocking silicon optical switch based on electro-optic Mach-Zehnder interferometers," Opt. Express **24**(9), 9295-9307 (2016).

[32] L. Qiao, W. Tang, and T. Chu, "32 x 32 silicon electro-optic switch with built-in monitors and balanced-status units," Sci. Rep. **7**, 42306 (2017).

[33] T. J. Seok, K. Kwon, J. Henriksson, J. H. Lu, and M. C. Wu, "Wafer-scale silicon photonic switches beyond die size limit," Optica **6**(4), 490-494 (2019).

[34] N. Sherwood-Droz, H. Wang, L. Chen, B. G. Lee, A. Biberman, K. Bergman, and M. Lipson, "Optical 4x4 hitless silicon router for optical Networks-on-Chip (NoC)," Opt. Express **16**(20), 15915-15922 (2008).

[35] C. Haffner, A. Joerg, M. Doderer, F. Mayor, D. Chelladurai, Y. Fedoryshyn, C. I. Roman, M. Mazur, M. Burla, H. J. Lezec, V. A. Aksyuk, and J. Leuthold, "Nano-opto-electro-mechanical switches operated at CMOS-level voltages," Science **366**(6467), 860-864 (2019).

[36] G. T. Reed, G. Mashanovich, F. Y. Gardes, and D. J. Thomson, "Silicon optical modulators," Nat. Photon. **4**(8), 518-526 (2010).

[37] A. Majumdar, and A. Rundquist, "Cavity-enabled self-electro-optic bistability in silicon photonics," Opt Lett **39**(13), 3864-3867 (2014).

[38] M. Wuttig, H. Bhaskaran, and T. Taubner, "Phase-change materials for non-volatile photonic applications," Nat. Photon. **11**(8), 465-476 (2017).

[39] J. Zheng, A. Khanolkar, P. Xu, S. Deshmukh, J. Myers, J. Frantz, E. Pop, J. Hendrickson, J. Doylend, N. Boechler, and A. Majumdar, "GST-on-silicon hybrid nanophotonic integrated circuits: a non-volatile quasi-continuously reprogrammable platform," Opt. Mater. Express **8**(6), 1551-1561 (2018).

[40] S. Abdollahramezani, O. Hemmatyar, H. Taghinejad, A. Krasnok, Y. Kiarashinejad, M. Zandehshahvar, A. Alù, and A. Adibi, "Tunable nanophotonics enabled by chalcogenide phase-change materials," Nanophotonics-Berlin **1**(ahead-of-print) (2020).

[41] M. Wuttig, and N. Yamada, "Phase-change materials for rewriteable data storage," Nat. Mater. **6**(11), 824-832 (2007).

[42] K. Shportko, S. Kremers, M. Woda, D. Lencer, J. Robertson, and M. Wuttig, "Resonant bonding in crystalline phase-change materials," Nat. Mater. **7**(8), 653-658 (2008).

[43] H. S. P. Wong, S. Raoux, S. Kim, J. L. Liang, J. P. Reifenberg, B. Rajendran, M. Asheghi, and K. E. Goodson, "Phase Change Memory," Proc. IEEE **98**(12), 2201-2227 (2010).

[44] S. Raoux, and M. Wuttig, *Phase change materials: science and applications* (Springer, 2009).

[45] D. Loke, T. H. Lee, W. J. Wang, L. P. Shi, R. Zhao, Y. C. Yeo, T. C. Chong, and S. R. Elliott, "Breaking the Speed Limits of Phase-Change Memory," Science **336**(6088), 1566-1569 (2012).

[46] F. Rao, K. Y. Ding, Y. X. Zhou, Y. H. Zheng, M. J. Xia, S. L. Lv, Z. T. Song, S. L. Feng, I. Ronneberger, R. Mazzarello, W. Zhang, and E. Ma, "Reducing the stochasticity of crystal nucleation to enable subnanosecond memory writing," Science **358**(6369), 1423-1426 (2017).

[47] S. Raoux, F. Xiong, M. Wuttig, and E. Pop, "Phase change materials and phase change memory," MRS Bull. **39**(8), 703-710 (2014).

[48] J. Zheng, Z. Fang, C. Wu, S. Zhu, P. Xu, J. K. Doylend, S. Deshmukh, E. Pop, S. Dunham, M. Li, and A. Majumdar, "Nonvolatile Electrically Reconfigurable Integrated Photonic Switch Enabled by a Silicon PIN Diode Heater," Adv. Mater., 2001218 (2020).

[49] F. Xiong, A. D. Liao, D. Estrada, and E. Pop, "Low-Power Switching of Phase-Change Materials with Carbon Nanotube Electrodes," Science **332**(6029), 568-570 (2011).

[50] J. von Keitz, J. Feldmann, N. Gruhler, C. Rios, C. D. Wright, H. Bhaskaran, and W. H. P. Pemice, "Reconfigurable Nanophotonic Cavities with Nonvolatile Response," ACS Photon. **5**(11), 4644-4649 (2018).

[51] N. Farmakidis, N. Youngblood, X. Li, J. Tan, J. L. Swett, Z. Cheng, C. D. Wright, W. H. P. Pernice, and H. Bhaskaran, "Plasmonic nanogap enhanced phase-change devices with dual electrical-optical functionality," Sci. Adv. **5**(11), eaaw2687 (2019).

[52] S. Raoux, G. W. Burr, M. J. Breitwisch, C. T. Rettner, Y. C. Chen, R. M. Shelby, M. Salinga, D. Krebs, S. H. Chen, H. L. Lung, and C. H. Lam, "Phase-change random access memory: A scalable technology," IBM J. Res. Dev. **52**(4-5), 465-479 (2008).

[53] D. Tanaka, Y. Shoji, M. Kuwahara, X. M. Wang, K. Kintaka, H. Kawashima, T. Toyosaki, Y. Ikuma, and H. Tsuda, "Ultra-small, self-holding, optical gate switch using Ge2Sb2Te5 with a multi-mode Si waveguide," Opt. Express **20**(9), 10283-10294 (2012).

[54] Z. Yu, J. Zheng, P. Xu, W. Zhang, and Y. Wu, "Ultracompact Electro-Optical Modulator-Based Ge2Sb2Te5 on Silicon," IEEE Photon. Technol. Lett. **30**(3), 250-253 (2018).

[55] P. Xu, J. Zheng, J. K. Doylend, and A. Majumdar, "Low-Loss and Broadband Nonvolatile Phase-Change Directional Coupler Switches," ACS Photon. **6**(2), 553-557 (2019).

[56] H. Y. Zhang, L. J. Zhou, J. Xu, N. N. Wang, H. Hu, L. J. Lu, B. M. A. Rahman, and J. P. Chen, "Nonvolatile waveguide transmission tuning with electrically-driven ultra-small GST phase-change material," Science Bulletin **64**(11), 782-789 (2019).

[57] H. Y. Zhang, L. J. Zhou, L. J. Lu, J. Xu, N. N. Wang, H. Hu, B. M. A. Rahman, Z. P. Zhou, and J. P. Ghen, "Miniature Multilevel Optical Memristive Switch Using Phase Change Material," ACS Photon. **6**(9), 2205-2212 (2019).

[58] C. Rios, M. Stegmaier, P. Hosseini, D. Wang, T. Scherer, C. D. Wright, H. Bhaskaran, and W. H. P. Pernice, "Integrated all-photonic non-volatile multi-level memory," Nat. Photon. **9**(11), 725-732 (2015).

[59] Z. Cheng, C. Ríos, W. H. Pernice, C. D. Wright, and H. Bhaskaran, "On-chip photonic synapse," Sci. Adv. **3**(9), e1700160 (2017).

[60] Z. G. Cheng, C. Rios, N. Youngblood, C. D. Wright, W. H. P. Pernice, and H. Bhaskaran, "Device-Level Photonic Memories and Logic Applications Using Phase-Change Materials," Adv. Mater. **30**(32), 1802435 (2018).

[61] C. M. Wu, H. S. Yu, H. Li, X. H. Zhang, I. Takeuchi, and M. Li, "Low-Loss Integrated Photonic Switch Using Subwavelength Patterned Phase Change Material," ACS Photon. **6**(1), 87-92 (2019).

[62] X. Li, N. Youngblood, C. Rios, Z. G. Cheng, C. D. Wright, W. H. P. Pernice, and H. Bhaskaran, "Fast and reliable storage using a 5 bit, nonvolatile photonic memory cell," Optica **6**(1), 1-6 (2019).

[63] C. Ríos, N. Youngblood, Z. Cheng, M. Le Gallo, W. H. Pernice, C. D. Wright, A. Sebastian, and H. Bhaskaran, "In-memory computing on a photonic platform," Sci. Adv. **5**(2), eaau5759 (2019).

[64] M. Rude, J. Pello, R. E. Simpson, J. Osmond, G. Roelkens, J. J. G. M. van der Tol, and V. Pruneri, "Optical switching at 1.55 μm in silicon racetrack resonators using phase change materials," Appl. Phys. Lett. **103**(14) (2013).

[65] T. Moriyama, D. Tanaka, P. Jain, H. Kawashima, M. Kuwahara, X. M. Wang, and H. Tsuda, "Ultra-compact, self-holding asymmetric Mach-Zehnder interferometer switch using Ge2Sb2Te5 phase-change material," IEICE Electron. Express **11**(15), 20140538 (2014).

[66] H. B. Liang, R. Soref, J. W. Mu, A. Majumdar, X. Li, and W. P. Huang, "Simulations of Silicon-on-Insulator Channel-Waveguide Electrooptical 2 x 2 Switches and 1 x 1 Modulators Using a Ge2Sb2Te5 Self-Holding Layer," J. Lightwave Technol. **33**(9), 1805-1813 (2015).

[67] M. Stegmaier, C. Rios, H. Bhaskaran, C. D. Wright, and W. H. P. Pernice, "Nonvolatile All-Optical 1 x 2 Switch for Chipscale Photonic Networks," Adv. Opt. Mater. **5**(1), 1600346 (2017).

[68] K. Kato, M. Kuwahara, H. Kawashima, T. Tsuruoka, and H. Tsuda, "Current-driven phase-change optical gate switch using indium-tin-oxide heater," Appl. Phys. Express **10**(7), 072201 (2017).

[69] W. H. P. Pernice, and H. Bhaskaran, "Photonic non-volatile memories using phase change materials," Appl. Phys. Lett. **101**(17), 171101 (2012).

[70] C. Rios, P. Hosseini, C. D. Wright, H. Bhaskaran, and W. H. P. Pernice, "On-Chip Photonic Memory Elements Employing Phase-Change Materials," Adv. Mater. **26**(9), 1372-1377 (2014).

[71] I. Chakraborty, G. Saha, A. Sengupta, and K. Roy, "Toward Fast Neural Computing using All-Photonic Phase Change Spiking Neurons," Sci. Rep. **8**(1), 12980 (2018).

[72] J. Feldmann, N. Youngblood, C. D. Wright, H. Bhaskaran, and W. H. P. Pernice, "All-optical spiking neurosynaptic networks with self-learning capabilities," Nature **569**(7755), 208-214 (2019).

[73] Y. G. Lu, M. Stegmaier, P. Nukala, M. A. Giambra, S. Ferrari, A. Busacca, W. H. P. Pernice, and R. Agarwal, "Mixed-Mode Operation of Hybrid Phase-Change Nanophotonic Circuits," Nano Lett. **17**(1), 150-155 (2017).

[74] N. Youngblood, C. Ríos, E. Gemo, J. Feldmann, Z. Cheng, A. Baldycheva, W. H. Pernice, C. D. Wright, and H. Bhaskaran, "Tunable Volatility of Ge2Sb2Te5 in Integrated Photonics," Adv. Funct. Mater., 1807571 (2019).

[75] Q. H. Zhang, Y. F. Zhang, J. Y. Li, R. Soref, T. Gu, and J. J. Hu, "Broadband nonvolatile photonic switching based on optical phase change materials: beyond the classical figure-of-merit," Opt. Lett. **43**(1), 94-97 (2018).

[76] R. Soref, "Tutorial: Integrated-photonic switching structures," APL Photon. **3**(2), 021101 (2018).

[77] J. Zheng, S. Zhu, P. Xu, S. Dunham, and A. Majumdar, "Modeling Electrical Switching of Nonvolatile Phase-Change Integrated Nanophotonic Structures with Graphene Heaters," ACS Appl. Mater. Interfaces **12**(19), 21827-21836 (2020).

[78] A. A. Balandin, "Thermal properties of graphene and nanostructured carbon materials," Nat. Mater. **10**(8), 569-581 (2011).

[79] E. Pop, V. Varshney, and A. K. Roy, "Thermal properties of graphene: Fundamentals and applications," MRS Bull. **37**(12), 1273-1281 (2012).

[80] Y. K. Wu, K. Liu, D. W. Li, Y. N. Guo, and S. Pan, "In situ AFM and Raman spectroscopy study of the crystallization behavior of Ge2Sb2Te5 films at different temperature," Appl. Surf. Sci. **258**(4), 1619-1623 (2011).

[81] A. Yariv, "Universal relations for coupling of optical power between microresonators and dielectric waveguides," Electron. Lett. **36**(4), 321-322 (2000).

[82] Y. Wang, X. Wang, J. Flueckiger, H. Yun, W. Shi, R. Bojko, N. A. F. Jaeger, and L. Chrostowski, "Focusing sub-wavelength grating couplers with low back reflections for rapid prototyping of silicon photonic circuits," Opt. Express **22**(17), 20652-20662 (2014).

[83] M. Stegmaier, C. Rios, H. Bhaskaran, and W. H. P. Pernice, "Thermo-optical Effect in Phase-Change Nanophotonics," ACS Photon. **3**(5), 828-835 (2016).

[84] V. R. Almeida, and M. Lipson, "Optical bistability on a silicon chip," Opt Lett **29**(20), 2387-2389 (2004).

[85] G. H. Wei, T. K. Stanev, D. A. Czaplewski, I. W. Jung, and N. P. Stern, "Silicon-nitride photonic circuits interfaced with monolayer MoS2," Appl. Phys. Lett. **107**(9), 091112 (2015).

[86] W. Bogaerts, P. De Heyn, T. Van Vaerenbergh, K. De Vos, S. K. Selvaraja, T. Claes, P. Dumon, P. Bienstman, D. Van Thourhout, and R. Baets, "Silicon microring resonators," Las. Photon. Rev. **6**(1), 47-73 (2012).

[87] C. D. Wright, Y. W. Liu, K. I. Kohary, M. M. Aziz, and R. J. Hicken, "Arithmetic and Biologically-Inspired Computing Using Phase-Change Materials," Adv. Mater. **23**(30), 3408-3413 (2011).

[88] F. Lou, D. X. Dai, and L. Wosinski, "Ultracompact polarization beam splitter based on a dielectric-hybrid plasmonic-dielectric coupler," Opt. Lett. **37**(16), 3372-3374 (2012).

[89] M. Komatsu, K. Saitoh, and M. Koshiba, "Design of miniaturized silicon wire and slot waveguide polarization splitter based on a resonant tunneling," Opt. Express **17**(21), 19225-19234 (2009).

[90] D. F. Gallagher, and T. P. Felici, "Eigenmode expansion methods for simulation of optical propagation in photonics: pros and cons," in *Integrated optics: devices, materials, and technologies VII* (International Society for Optics and Photonics, 2003), pp. 69-82.

[91] H. Yun, W. Shi, Y. Wang, L. Chrostowski, and N. A. F. Jaeger, "2x2 adiabatic 3-dB coupler on silicon-on-insulator rib waveguides," in *Photonics North 2013* (SPIE, 2013), paper 6.

[92] Z. Q. Lu, H. Yun, Y. Wang, Z. T. Chen, F. Zhang, N. A. F. Jaeger, and L. Chrostowski, "Broadband silicon photonic directional coupler using asymmetric-waveguide based phase control," Opt. Express **23**(3), 3795-3806 (2015).

[93] W. Dong, H. Liu, J. K. Behera, L. Lu, R. J. Ng, K. V. Sreekanth, X. Zhou, J. K. Yang, and R. E. Simpson, "Wide Bandgap Phase Change Material Tuned Visible Photonics," Adv. Funct. Mater., 1806181 (2018).

[94] Y. Zhang, J. B. Chou, J. Li, H. Li, Q. Du, A. Yadav, S. Zhou, M. Y. Shalaginov, Z. Fang, H. Zhong, C. Roberts, P. Robinson, B. Bohlin, C. Rios, H. Lin, M. Kang, T. Gu, J. Warner, V. Liberman, K. Richardson, and J. Hu, "Broadband transparent optical phase change materials for high-performance nonvolatile photonics," Nat. Commun. **10**(1), 4279 (2019).

[95] H. Taghinejad, S. Abdollahramezani, A. A. Eftekhar, T. Fan, A. H. Hosseinnia, O. Hemmatyar, A. E. Dorche, A. Gallmon, and A. Adibi, "ITO-Based Microheaters for Reversible Multi-Stage Switching of Phase-Change Materials: Towards Miniaturized Beyond-Binary Reconfigurable Integrated Photonics," arXiv preprint arXiv:2003.04097 (2020).

[96] C. Rios, M. Stegmaier, Z. G. Cheng, N. Youngblood, C. D. Wright, W. H. P. Pernice, and H. Bhaskaran, "Controlled switching of phase-change materials by evanescent-field coupling in integrated photonics," Opt. Mater. Express **8**(9), 2455-2470 (2018).

[97] A. Redaelli, A. Pirovano, A. Benvenuti, and A. L. Lacaita, "Threshold switching and phase transition numerical models for phase change memory simulations," Journal of Applied Physics **103**(11), 111101 (2008).

[98] S. Gan, C. Cheng, Y. Zhan, B. Huang, X. Gan, S. Li, S. Lin, X. Li, J. Zhao, and H. Chen, "A highly efficient thermo-optic microring modulator assisted by graphene," Nanoscale **7**(47), 20249-20255 (2015).

[99] S. Q. Yan, X. L. Zhu, L. H. Frandsen, S. S. Xiao, N. A. Mortensen, J. J. Dong, and Y. H. Ding, "Slow-light-enhanced energy efficiency for graphene microheaters on silicon photonic crystal waveguides," Nat. Commun. **8**, 14411 (2017).

[100] F. Bonaccorso, Z. Sun, T. Hasan, and A. C. Ferrari, "Graphene photonics and optoelectronics," Nat. Photon. **4**(9), 611-622 (2010).

[101] C. H. Liu, J. J. Zheng, Y. Y. Chen, T. Fryett, and A. Majumdar, "Van der Waals materials integrated nanophotonic devices [Invited]," Opt. Mater. Express **9**(2), 384-399 (2019).

[102] M. Liu, X. B. Yin, E. Ulin-Avila, B. S. Geng, T. Zentgraf, L. Ju, F. Wang, and X. Zhang, "A graphene-based broadband optical modulator," Nature **474**(7349), 64-67 (2011).

[103] F. Wang, Y. B. Zhang, C. S. Tian, C. Girit, A. Zettl, M. Crommie, and Y. R. Shen, "Gate-variable optical transitions in graphene," Science **320**(5873), 206-209 (2008).

[104] A. Majumdar, J. Kim, J. Vuckovic, and F. Wang, "Electrical control of silicon photonic crystal cavity by graphene," Nano Lett. **13**(2), 515-518 (2013).

[105] H. Li, Y. Anugrah, S. J. Koester, and M. Li, "Optical absorption in graphene integrated on silicon waveguides," Appl. Phys. Lett. **101**(11), 111110. (2012).

[106] J. Orava, A. L. Greer, B. Gholipour, D. W. Hewak, and C. E. Smith, "Characterization of supercooled liquid Ge2Sb2Te5 and its crystallization by ultrafast-heating calorimetry," Nat. Mater. **11**(4), 279-283 (2012).

[107] Z. Chen, W. Jang, W. Bao, C. N. Lau, and C. Dames, "Thermal contact resistance between graphene and silicon dioxide," Appl. Phys. Lett. **95**(16) (2009).

[108] K. Cil, "Temperature dependent characterization and crystallization dynamics of Ge2Sb2Te5 thin films and nanoscale structures," (2015).

[109] C. Y. Ahn, S. W. Fong, Y. Kim, S. Lee, A. Sood, C. M. Neumann, M. Ashegh, K. E. Goodson, E. Pop, and H. S. P. Wong, "Energy-Efficient Phase-Change Memory with Graphene as a Thermal Barrier," Nano Lett. **15**(10), 6809-6814 (2015).

[110] T. Yagi, K. Tamano, Y. Sato, N. Taketoshi, T. Baba, and Y. Shigesato, "Analysis on thermal properties of tin doped indium oxide films by picosecond thermoreflectance measurement," Journal of Vacuum Science & Technology A **23**(4), 1180-1186 (2005).

[111] G. W. Hanson, "Dyadic Green's functions and guided surface waves for a surface conductivity model of graphene," Journal of Applied Physics **103**(6), 064302 (2008).

[112] Z. Z. Ma, Z. R. Li, K. Liu, C. R. Ye, and V. J. Sorger, "Indium-Tin-Oxide for High-performance Electro-optic Modulation," Nanophotonics-Berlin **4**(2), 198-213 (2015).

[113] W. J. Liu, K. Etessam-Yazdani, R. Hussin, and M. Asheghi, "Modeling and data for thermal conductivity of ultrathin single-crystal SOI layers at high temperature," IEEE Transactions on Electron Devices **53**(8), 1868-1876 (2006).

[114] V. Palankovski, R. Schultheis, and S. Selberherr, "Simulation of power heterojunction bipolar transistors on gallium arsenide," IEEE Transactions on Electron Devices **48**(6), 1264-1269 (2001).

[115] J. J. Zheng, L. H. Yu, S. L. He, and D. X. Dai, "Tunable pattern-free graphene nanoplasmonic waveguides on trenched silicon substrate," Sci. Rep. **5**, 7987 (2015).

[116] K. I. Bolotin, K. J. Sikes, J. Hone, H. L. Stormer, and P. Kim, "Temperature-dependent transport in suspended graphene," Physical Review Letters **101**(9), 096802 (2008).

[117] M. Freitag, M. Steiner, Y. Martin, V. Perebeinos, Z. H. Chen, J. C. Tsang, and P. Avouris, "Energy Dissipation in Graphene Field-Effect Transistors," Nano Lett. **9**(5), 1883-1888 (2009).

[118] H. K. Lyeo, D. G. Cahill, B. S. Lee, J. R. Abelson, M. H. Kwon, K. B. Kim, S. G. Bishop, and B. K. Cheong, "Thermal conductivity of phase-change material Ge2Sb2Te5," Appl. Phys. Lett. **89**(15) (2006).

[119] A. Pirovano, A. L. Lacaita, A. Benvenuti, F. Pellizzer, S. Hudgens, and R. Bez, "Scaling analysis of phase-change memory technology," in *IEEE International Electron Devices Meeting 2003* (IEEE, 2003), pp. 29.26. 21-29.26. 24.

[120] W. K. Njoroge, H. W. Woltgens, and M. Wuttig, "Density changes upon crystallization of Ge2Sb2.04Te4.74 films," Journal of Vacuum Science & Technology a-Vacuum Surfaces and Films **20**(1), 230-233 (2002).

[121] L. H. Yu, J. J. Zheng, Y. Xu, D. X. Dai, and S. L. He, "Local and nonlocal optically induced transparency effects in graphene-silicon hybrid nanophotonic integrated circuits," ACS Nano **8**(11), 11386-11393 (2014).

[122] S. M. Sze, and K. K. Ng, *Physics of semiconductor devices* (John Wiley & Sons, 2006).

[123] J. T. Gaskins, P. E. Hopkins, D. R. Merrill, S. R. Bauers, E. Hadland, D. C. Johnson, D. Koh, J. H. Yum, S. Banerjee, B. J. Nordell, M. M. Paquette, A. N. Caruso, W. A. Lanford, P. Henry, L. Ross, H. Li, L. Y. Li, M. French, A. M. Rudolph, and S. W. King, "Review-Investigation and Review of the Thermal, Mechanical, Electrical, Optical, and Structural Properties of Atomic Layer Deposited High-k Dielectrics: Beryllium Oxide, Aluminum Oxide, Hafnium Oxide, and Aluminum Nitride," ECS J. Solid State Sci. Technol. **6**(10), N189-N208 (2017).

[124] "ALUMINIUM OXIDE (Al2O3)," http://www-ferp.ucsd.edu/LIB/PROPS/PANOS/al2o3.html.

[125] W. D. Sacher, and J. K. S. Poon, "Dynamics of microring resonator modulators," Opt. Express **16**(20), 15741-15753 (2008).

[126] Z. Fang, J. Zheng, and A. Majumdar, "Non-volatile Integrated Photonics enabled by Broadband Transparent Phase Change Material," in *CLEO: Science and Innovations* (Optical Society of America, 2020), paper JTh2B.3.

[127] N. Dhingra, J. C. Song, G. J. Saxena, E. K. Sharma, and B. M. A. Rahman, "Design of a Compact Low-Loss Phase Shifter Based on Optical Phase Change Material," IEEE Photon. Technol. Lett. **31**(21), 1757-1760 (2019).

[128] V. Joshi, M. Le Gallo, S. Haefeli, I. Boybat, S. R. Nandakumar, C. Piveteau, M. Dazzi, B. Rajendran, A. Sebastian, and E. Eleftheriou, "Accurate deep neural network inference using computational phase-change memory," Nat. Commun. **11**(1) (2020).

[129] A. Sebastian, M. Le Gallo, and E. Eleftheriou, "Computational phase-change memory: beyond von Neumann computing," J Phys D Appl Phys **52**(44) (2019).

[130] M. Rastegari, V. Ordonez, J. Redmon, and A. Farhadi, "Xnor-net: Imagenet classification using binary convolutional neural networks," in *European conference on computer vision* (Springer, 2016), pp. 525-542.

[131] F. Zokaee, Q. Lou, N. Youngblood, W. Liu, Y. Xie, and L. Jiang, "LightBulb: A Photonic-Nonvolatile-Memory-based Accelerator for Binarized Convolutional Neural Networks," in *2020 Design, Automation & Test in Europe Conference & Exhibition (DATE)* (IEEE, 2020), pp. 1438-1443.

[132] A. Sarangan, J. Duran, V. Vasilyev, N. Limberopoulos, I. Vitebskiy, and I. Anisimov, "Broadband Reflective Optical Limiter Using GST Phase Change Material," IEEE Photonics J. **10**(1) (2018).

[133] M. N. Julian, C. Williams, S. Borg, S. Bartram, and H. J. Kim, "Reversible optical tuning of GeSbTe phase-change metasurface spectral filters for mid-wave infrared imaging," Optica **7**(7), 746-754 (2020).

[134] W. F. Jiang, "Nonvolatile and ultra-low-loss reconfigurable mode (De) multiplexer/switch using triple-waveguide coupler with Ge2Sb2Se4Te1 phase change material," Sci. Rep. **8**(1), 1-12 (2018).

[135] B. H. Zhang, W. W. Chen, P. J. Wang, S. X. Dai, W. F. Jiang, W. Liang, H. Lu, J. Ding, J. Li, Y. Li, Q. Fu, T. G. Dai, H. Yu, and J. Y. Yang, "Switchable Polarization Beam Splitter Based on GST-on-Silicon Waveguides," IEEE Photonics J. **12**(2) (2020).

VITA

Jiajiu Zheng is a research assistant currently pursuing Ph.D. in Electrical Engineering at the University of Washington, Seattle. He received his M.S. in Optical Engineering from Zhejiang University in 2015 and his B.S. in Optoelectronic and Information Engineering from Nanjing University of Science and Technology in 2012. Zheng's research interests include but are not limited to silicon photonics, optical computing, and nanophotonics. Particularly, his current research focuses on nonvolatile programmable silicon photonics using phase-change materials towards optical FPGAs for applications such as data center, neuromorphic computing, and quantum computing. Previously, Zheng worked on self-electro-optic bistability devices, subwavelength grating-assisted directional coupler devices, novel photonic crystal nanobeam cavities, van der Waals metasurfaces, cavity-enhanced PL, EL, and SHG from 2D materials, on-chip graphene photodetectors, modulators, nonlinearity, and plasmonics, and so on. He is the recipient of the National Scholarship of China (2009-2010) and the OMEx Emerging Researcher Best Paper Prize (2018).

Publications during Ph.D.

[1] **Jiajiu Zheng**, Z. Fang, C. Wu, S. Zhu, P. Xu, J. K. Doylend, S. Deshmukh, E. Pop, S. Dunham, M. Li, A. Majumdar, "Nonvolatile Electrically Reconfigurable Integrated Photonic Switch Enabled by a Silicon PIN Diode heater", ***Advanced Materials***, 2001218 (2020).

[2] **Jiajiu Zheng**, S. Zhu, P. Xu, S. Dunham, A. Majumdar, "Modeling Electrical Switching of Nonvolatile Phase-Change Integrated Nanophotonic Structures with Graphene Heaters", ***ACS Applied Materials & Interfaces*** 12(19), 21827-21836 (2020).

[3] F. Zhang, **Jiajiu Zheng**, Y. Song, W. Liu, P. Xu, A. Majumdar, "Ultra-Broadband and Compact Polarizing Beam Splitter in Silicon Photonics", ***OSA Continuum*** 3(3), 560-567 (2020).

[4] J. Zhou, **Jiajiu Zheng**, Z. Fang, P. Xu, A. Majumdar, "Ultra-Low Mode Volume on-Substrate Silicon Nanobeam Cavity", ***Optics Express*** 27(21), 30692-30699 (2019).

[5] H. Xie, **Jiajiu Zheng**, P. Xu, J. Yao, J. Whitehead, A. Majumdar, "Ultra-Compact and Low-Loss Polarization-Independent Directional Coupler Using Subwavelength Gratings", ***IEEE Photonics Technology Letters*** **(Front Cover Paper)** 31(18), 1538-1541 (2019).

[6] C. Zou, **Jiajiu Zheng**, C. Chang, A. Majumdar, L. Y. Lin, "Nonvolatile Rewritable Photomemory Arrays Based on Reversible Phase-Change Perovskite for Optical Information Storage", ***Advanced Optical Materials*** 7(18), 1900558 (2019).

[7] Y. Chen, J. Whitehead, A. Ryou, **Jiajiu Zheng**, P. Xu, T. K. Fryett, A. Majumdar, "Large thermal tuning of polymer-embedded silicon nitride nanobeam cavity", ***Optics Letters*** **(Editor's Pick)** 44(12), 3058-3061 (2019).

[8] P. Xu, **Jiajiu Zheng**, J. Zhou, Y. Chen, C. Zhou, A. Majumdar, "Multi-Slot Photonic Crystal Cavities for High-Sensitivity Refractive Index Sensing", ***Optics Express*** 27(3), 3609-3616 (2019).

[9] P. Xu†, **Jiajiu Zheng**† (**Co-first author**), J. Doylend, A. Majumdar, "Low-Loss and Broadband Nonvolatile Phase-Change Directional Coupler Switches", ***ACS Photonics*** 6(2), 553-557 (2019).

[10] C. H. Liu, **Jiajiu Zheng**, Y. Chen, T. K. Fryett, A. Majumdar, "Van der Waals Materials Integrated Nanophotonic Devices", ***Optical Materials Express*** **(Invited Review)** 9(2), 384-399 (2019).

[11] C. H. Liu, **Jiajiu Zheng**, S. Colburn, T. K. Fryett, Y. Chen, X. Xu, A. Majumdar, "Ultrathin Van der Waals Metalenses", ***Nano Letter*** 18(11), 6961-6966 (2018).

[12] **Jiajiu Zheng**, A. Khanolkar, P. Xu, S. Colburn, S. Deshmukh, J. Myers, J. Frantz, E. Pop, J. Hendrickson, J. Doylend, N. Boechler, A. Majumdar, "GST-on-Silicon Hybrid Nanophotonic Integrated Circuits: A Non-volatile Quasi-Continuously Reprogrammable Platform", ***Optical Materials Express*** **(Best Paper Prize)** 8(6), 1551-1561 (2018).

[13] Z. Yu, **Jiajiu Zheng**, P. Xu, W. Zhang, Y. Wu, "Ultracompact Electro-Optical Modulator based $Ge_2Sb_2Te_5$ on Silicon", ***IEEE Photonics Technology Letters*** 30(3), 250-253 (2018).

[14] C. H. Liu, G. Clark, T. K. Fryett, S. Wu, **Jiajiu Zheng**, F. Hatami, X. Xu, A. Majumdar, "Nanocavity Integrated van der Waals Heterostructure Light-Emitting Tunneling Diode", ***Nano Letter*** 17(1), 200-205 (2017).

[15] T. K. Fryett, K. L. Seyler, **Jiajiu Zheng**, C. H. Liu, X. Xu, A. Majumdar, "Silicon Photonic Crystal Cavity Enhanced Second-Harmonic Generation from Monolayer WSe_2", ***2D Materials*** 4(1), 015031 (2016).

Conference papers and presentations during Ph.D.

[1] Nonvolatile Electrically Reconfigurable Integrated Photonic Switches Using Phase-Change Materials, oral presentation delivered in ***CLEO***, online, USA, May 11-15, 2020.

[2] Nonvolatile Electrically Reconfigurable Silicon Photonic Switches Using Phase-Change Materials, oral presentation delivered in ***Frontiers in Optics***, Washington, USA, September 15-19, 2019.

[3] Broadband Low-loss Non-volatile Photonic Switches Using Phase-Change Materials, oral presentation delivered in ***CLEO***, San Jose, USA, May 5-10, 2019.

[4] Nonvolatile Programmable Silicon Photonics Using Phase-Change Materials, oral presentation delivered in ***Photonics West***, San Francisco, USA, February 2-7, 2019.

[5] Non-volatile Quasi-Continuously Reprogrammable Silicon Photonic Integrated Circuits Using Phase-Change Materials, oral and poster presentation delivered in ***SRC TECHCON***, Austin, USA, September 16-19, 2018.

[6] Non-volatile All-Optical Quasi-Continuous Switching in GST-on-Silicon Microring Resonators, oral presentation delivered in ***CLEO***, San Jose, USA, May 13-18, 2018.

[7] Self-Electro-Optic Bistability in Hybrid Silicon Photonic Microring Resonators, poster presentation delivered in ***CLEO***, San Jose, USA, May 14-19, 2017.